PL-TR-91-2160

*E 200 &...*

②

PROPAGATION OF REGIONAL PHASES:
OBSERVATIONS AND THEORY

J. A. Orcutt
M. A. H. Hedlin

University of California, San Diego
Scripps Institution of Oceanography
La Jolla, CA 92093

DTIC
ELECTE
S JAN 15 1992 D
b

30 September 1991

Final Report
6 April 1989-1 July 1991

92-01234
║█║║║█║█║║║█║█║║█║║█║║█║║█║║║█║

92 1 14 018

This technical report has been reviewed and is approved for
publication.


_____          _____
JAMES F. LEVKOWICZ                        JAMES F. LEWKOWICZ
Contract Manager                          Branch Chief
Solid Earth Geophysics Branch             Solid Earth Geophysics Branch
Earth Sciences Division                   Earth Sciences Division


FOR THE COMMANDER


_____
DONALD H. ECKHARDT, Director
Earth Sciences Division

# REPORT DOCUMENTATION PAGE

| 1. AGENCY USE ONLY (Leave blank) | 2. REPORT DATE Sept. 30 1991 | 3. REPORT TYPE AND DATES COVERED Final Report (6 Apr 89–1 July 91) |
|---|---|---|

**4. TITLE AND SUBTITLE**
Propagation of Regional Phases:
Observations and Theory

**5. FUNDING NUMBERS**
PE 61101E
PR 9A10  TA DA  WU AL

Contract F19628-89-K-0018

**6. AUTHOR(S)**

Orcutt, J.A. and Hedlin, M.A.H.

**7. PERFORMING ORGANIZATION NAME(S) AND ADDRESS(ES)**
University of California, San Diego
Scripps Institution of Oceanography
La Jolla, CA 92093

**8. PERFORMING ORGANIZATION REPORT NUMBER**

**9. SPONSORING/MONITORING AGENCY NAME(S) AND ADDRESS(ES)**
Phillips Laboratory
Hanscom AFB, Massachusetts 01731-5000

Contract Manager: James Lewkowicz/LWH

**10. SPONSORING/MONITORING AGENCY REPORT NUMBER**

PL-TR-91-2160

**11. SUPPLEMENTARY NOTES**

**12a. DISTRIBUTION/AVAILABILITY STATEMENT**

Approved for public release; distribution unlimited

**12b. DISTRIBUTION CODE**

**13. ABSTRACT (Maximum 200 words)** In this report we present the results of investigations dealing with three topics: We have continued our investigation of the influence the regular repetition of features in seismograms, introducted at the source and/or during propagation by layer resonance, has on the spectrum of the recorded coda. We have developed an automatic algorithm that discriminates mining explosions from nuclear explosions and Earthquakes.
We consider the influence large crustal inhomogeneities, or topographic undulations, in the vicinity of receivers can have on the character of the recorded seismic coda. Specifically, we have developed a migration technique that scans the recorded coda for phases generated by local scattering interactions.
We have developed a regularized approach to seismic deconvolution that allows the introduction of a priori information, such as that describing the statistical nature of the additive noise and the underlying model, into the inversion process. We investigate how this algorithm can enhance the images produced by the migration algorithm developed in the previous section.

**14. SUBJECT TERMS**
discrimination  Seismic imaging
ripple-firing  deconvolution
quarry blasts

**15. NUMBER OF PAGES**
104

**16. PRICE CODE**

| 17. SECURITY CLASSIFICATION OF REPORT | 18. SECURITY CLASSIFICATION OF THIS PAGE | 19. SECURITY CLASSIFICATION OF ABSTRACT | 20. LIMITATION OF ABSTRACT |
|---|---|---|---|
| Unclassified | Unclassified | Unclassified | SAR |

# TABLE OF CONTENTS

# TASK OBJECTIVES

There are two broad objectives in this research effort. The first objective is to improve our understanding of the propagation of high frequency regional phases through the continental crust. This analysis involves the synthesis of realistic wavetrains, array processing and data analysis of NORESS/FINESS, Soviet and U.S. data. The second objective is to investigate the generation of seismic noise at the seafloor and, subsequently, the continents.

Specifically, the Work Statement includes the following:

- Compare regional broadband seismic data from the following sources:
  - NORESS/FINESS
  - Soviet high frequency data from the IRIS/IDA network in the USSR.
  - U.S. broad band stations including the Piñon IRIS/IDA station and the stations established in the western US for monitoring tests in Nevada and monitored at IGPP through a satellite telemetry link.

- Synthesize regional phases through the use of wavenumber integration.
  - Examine complex crustal and upper mantle structures.
  - Examine Q and frequency dependence at the European, Soviet and US sites.

- Array Processing of NORESS/FINESS data and comparison to synthetics.
  - Determine the frequency dependence of polarization anomalies caused by anisotropy. Apply to NORESS, Soviet and U.S. data.
  - Investigate the role of scattering in generation of regional phase coda.

- Physical modeling of seafloor and continental noise.

iv

# TECHNICAL RESULTS

## ABSTRACT

In this report we present the results of investigations dealing with three topics:

- We have continued our investigation of the influence the regular repetition of features in seismograms, introduced at the source and/or during propagation by layer resonance, has on the spectrum of the recorded coda. We have developed an automatic algorithm that discriminates mining explosions from nuclear explosions and Earthquakes.

- We consider the influence large crustal inhomogeneities, or topographic undulations, in the vicinity of receivers can have on the character of the recorded seismic coda. In specific we have developed a migration technique that scans the recorded coda for phases generated by local scattering interactions.

- We have developed a regularized approach to seismic deconvolution that allows the introduction of a priori information, such as that describing the statistical nature of the additive noise and the underlying model, into the inversion process. We investigate how this algorithm can enhance the images produced by the migration algorithm developed in the previous section.

## SUMMARY

As part of the last DARPA/AFGL contract we endeavored to determine how regional seismic network data can be used to discriminate ripple fired mining explosions from single event explosions. As part of this work, theory was developed which makes two predictions. Ripple-fired quarry blasts should produce coda that is highly colored. This spectral character should be resistant to change with time. A technique (sonogram analysis) was developed which expands the information contained in time series into a time-frequency plane and thus allows visual identification of time-independant spectral components. The technique was originally applied to data collected by the NRDC network of sensors. This dataset proved to be well suited to this endeavor since it contains regional recordings of single-event chemical explosions (detonated in the fall of 1987 by a joint Soviet-American team) in addition to a large number of recordings of events strongly believed to be ripple-fired mining explosions. The proximity of the stations to

the events is important since the algorithm depends on (and exploits) the retention of high-frequency energy - it is a broad band technique.

This work has been extended in Chapter 1 to use data recorded by arrays (in this case the NORESS small aperture array in Norway) and to determine if ripple-fired events in other geographic, and technical, settings appear to be anomalous when viewed using the sonogram technique. In view of the inverse relationship between the size a seismic event and its frequency of occurrance, this chapter is devoted to the development of a technique that automatically discriminates between quarry blasts and earthquakes, or single-event explosions. It is based on the assumption that quarry blasts that are comprised of a number of sub explosions closely grouped in space and time can be discriminated from the simpler events by virtue of the fact that they produce coda with distinctive spectral features that are resistant to change as time passes.

In chapter 2, work that has bearing on nuclear detection and discrimination of relatively large events (roughly 150 kT) from teleseismic ranges is introduced. This chapter describes how coda recorded by arrays can be scanned, or migrated, to image the local crust for scatterers large enough to emit recognizable surface waves (Rg) when excited by teleseismic body phases. There is some concern that such arrivals may be confused with the pP phase used to discriminate deep events from shallow events (most earthquakes from nuclear explosions). Although more physically comprehensive methods (such as f-k migration, Kirchoff migration and finite difference migration) have been developed to process seismic reflection data, we have chosen to adapt hyperbola-summation migration to our problem because we are dealing with dispersive wavelets. The idea of using small-aperture arrays for this type of imaging is tested extensively by examining synthetic (and thus controlled) datasets. The synthetic sources are infinitely small and can be used to assess the spatial resolution of the technique, and how this varies as the source moves, the array changes, or the imaging parameters vary. More significantly, this chapter concludes by relating the radial resolution with the temporal duration of the teleseismic wavetrains. It is concluded that deconvolution of the array records is necessary, and can be used to increase radial resolution. Unlike the work in Chapter 1, which requires the retention of high frequency energy and thus uses regional seismic stations, this chapter deals with a relatively narrow, and low, band of seismic energy - from 1.0 to 3.0 Hz.

In Chapter 3 a technique that relies on inverse theory is developed to deconvolve the teleseismic wavetrain from the seismic recordings to improve the radial spatial resolution. The algorithm is designed to produce models by trading off two undesirable quantities - data misfit and model complexity. A priori information, obtained from physical arguments regarding how we expect incident seismic energy interacts with large crustal scatterers, is used to define what level of model simplicity, in the form of serial correlation or smoothness, should be present in the model. The statistical character of the additive noise (which is assumed to be due to a random process) is estimated by assuming ergodicity and examining pre-event noise.

# Chapter 1

# An automatic means to discriminate between
# earthquakes and quarry blasts

## Abstract

In this chapter we discuss our efforts to use the NORESS array to discriminate between regional earthquakes and ripple-fired quarry blasts (events that involve a number of sub-explosions closely grouped in space and time). The method we describe is an extension of the time versus frequency "pattern-based" discriminant proposed by Hedlin *et al.* (1989b). At the heart of the discriminant is the observation that ripple-fired events tend to give rise to coda dominated by prominent spectral features that are independent of time and periodic in frequency. This spectral character is generally absent from the coda produced by earthquakes and "single-event" explosions. The discriminant originally proposed by Hedlin *et al* (1989b) used data collected at 250 $s^{-1}$ by single sensors in the 1987 NRDC network in Kazakhstan, U.S.S.R.. We have found that despite the relatively low digitization rate provided by the NORESS array (40 $s^{-1}$) we have had good success in our efforts to discriminate between earthquakes and quarry blasts by stacking all vertical array channels to improve signal to noise ratios.

We describe our efforts to automate the method, so that visual pattern recognition is not required, and to make it less susceptible to spurious time-independent spectral features not originating at the source. In essence we compute a Fourier transform of the time-frequency matrix and examine the power levels representing energy that is periodic in frequency and independent of time. Since a double Fourier transform is involved, our method can be considered as an extension of "cepstral" analysis (Tribolet, 1979). We have found, however, that our approach is superior since it is cognizant of the time independence of the spectral features of interest. We use earthquakes to define what cepstral power is to be expected in the absence of ripple firing and search for events that violate this limit. The assessment

of the likelihood that ripple firing occurred at the source is made automatically by the computer and is based on the extent to which the limit is violated.

## 1.1 Introduction

There is a peculiar breed of seismic event known as a ripple-fired explosion. Such an event differs markedly from a standard "single-event" explosion since it involves the detonation of numerous sub-explosions closely, and generally regularly, grouped in space and time. Ripple-firing is a technique commonly used in quarry blasting (Langefors and Kihlström, 1978) where mine operators are striving to reduce ground motions in areas proximal to the mine, enhance rock-fracturing and reduce the amount of material thrown into the air - "fly" or "throw" rock - (Dowding, 1985). Ripple-firing is in widespread use, being employed both in the Americas and in Europe (Stump et al., 1989).

There has been increased interest in recent years in discriminating mining events from earthquakes and nuclear explosions. A reduced Threshold Test Ban Treaty could potentially bring the magnitude of the largest nuclear explosions down to that of large "engineering" explosions otherwise known as quarry blasts (Stump and Reamer, 1988). Aggravating the problem is the existence of numerous quarries in the vicinity of the Semipalatinsk nuclear test site in the Soviet Union (Thurber et al., 1989; Hedlin et al 1989b). There have been a number of studies dealing directly and indirectly with this problem. Looking primarily at Scandinavian events recorded by the NORESS array, Baumgardt and Ziegler (1988) found prominent spectral modulation in events believed to involve ripple-firing, but not in the spectra computed from earthquake seismograms. Hedlin et al. (1989b) observed similar spectral modulation in the coda produced by suspected quarry blasts in Kazakhstan, U.S.S.R., but not in the coda produced by single-event calibration explosions detonated at similar ranges. They found further that the modulation, when present, was independent of time from the onset, well into the $L_g$ coda. This time-independent character has also been observed in the coda produced by quarry blasts and recorded in Scandinavia (Hedlin et al., 1989a). Both Baumgardt and Ziegler (1988) and Hedlin et al. (1989b) found that the spectral modulation observed in the coda produced by mine explosions could be reproduced effectively by assuming that all sub-explosions produce the same, common, waveform and that the motions superpose linearly. Stump and Reinke (1988) have investigated the validity of the assumption of linear superposition. They produced strong evidence supporting the assumption when wavefields from small, closely spaced, explosions are observed in the nearfield. Baumgardt and Ziegler (1988), Hedlin et al (1989a,b), Stump and Reamer (1988) and Smith (1989) - who also observed prominent peaks in the

2

spectra of phases produced by some quarry blasts - all concluded that the unusual spectral color could be used to discriminate quarry blasts from other events with "whiter" spectra.

In this work we are extending the study described in Hedlin *et al.*(1989b), hereafter referred to as paper 1, in a number of ways. We examine recordings of earthquakes, not single-event explosions, to determine if they can be discriminated from quarry blasts with a similar degree of success. We seek to determine the sensitivity of the method to the recording "environment". The recordings examined in the current study have been made at 40 $s^{-1}$ by the NORESS small aperture-array in Norway (Ringdal and Husebye, 1982; Mykkeltveit *et al.*, 1983). The data considered in paper 1 were recorded by single sensors and digitized at 250 $s^{-1}$. We feel that any successful discriminant should not depend strongly on the local geologic setting and mining practice. In paper 1 we examined events that occurred in central Asia, in this chapter we consider Scandinavian events. We have automated the algorithm to the point where discrimination can be carried out solely by the computer. This type of problem has also been investigated by Baumgardt and Ziegler (1989). Their approach also relies heavily on the expected time-independence of spectral modulation in the coda produced by ripple-fired events. In both the present work and Baumgardt and Ziegler (1989) the underlying premise of this automation is that in the future, if lower thresholds are realized, and thus a significantly greater data set must be examined, it will be beneficial and desirable to distance the human element from the discrimination process.

## 1.2 The data set

The bulk of the data used by this study were collected by sensors in the NORESS small-aperture array - located in south-eastern Norway - from 1985 to 1986 (see Figure 1.1 and Table 1.1). The NORESS array is composed primarily of 25 vertical component sensors deployed roughly 2 m deep in shallow vaults arranged in a set of concentric rings (Mykkeltveit *et al.*, 1983). The fourth and outermost ring is roughly 3 km across. The signal, collected by GS-13 seismometers which have a flat response to ground velocity between 1 and 10 Hz, is digitized at 40 $s^{-1}$. NORESS is actually part of a significantly larger array, known as NORSAR, and is situated within element 06C at this array, a site known to be particularly sensitive to signals propagating from Semipalatinsk (Richards, 1988). The seismometers are deployed in competent igneous rocks of granitic, rhyolitic and gabbroic composition (Mykkeltveit, 1987) and Precambrian or Paleozoic age (Bungum *et al.*, 1985). The site is thus relatively immune to the near-surface resonance of seismic energy. A more complete description of the array can be found in Mykkeltveit *et al.* (1983).
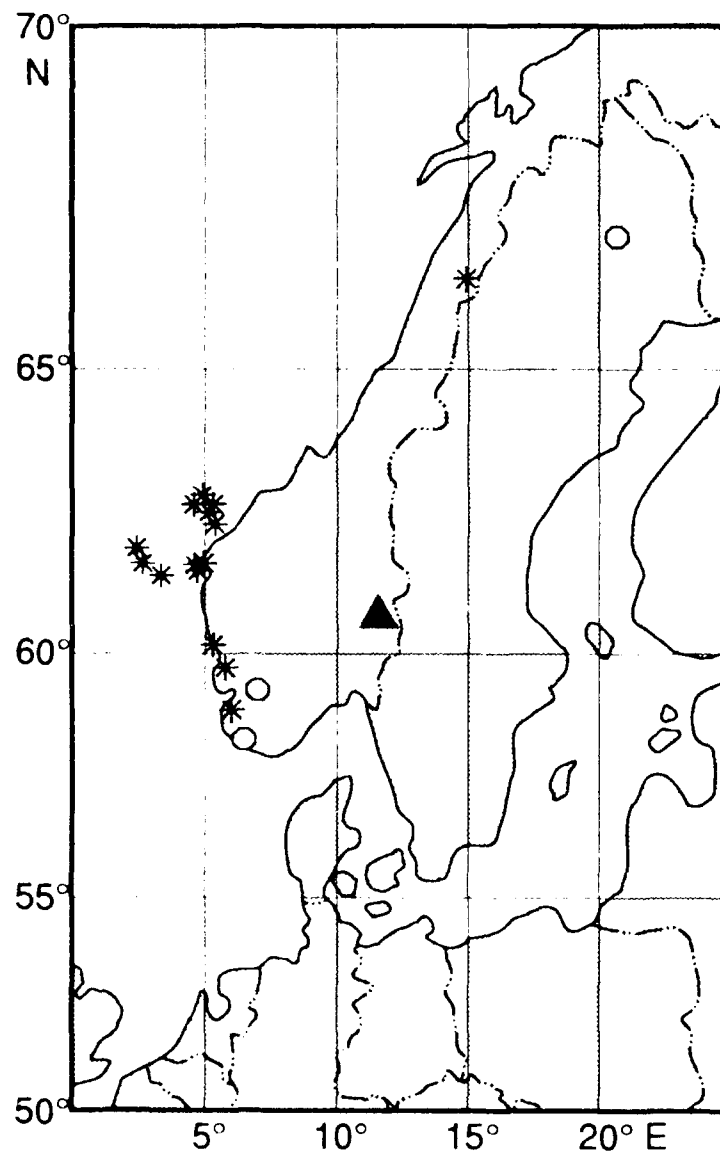
3

Figure 1.1 Map showing the locations of the earthquakes (stars), explosions (octagons) and the NORESS array (dark triangle).

| Event | Latitude | Longitude | Origin Time | Ml | Event type |
|---|---|---|---|---|---|
| | °N | °E | y/d-h:m:s (UTC) | | |
| 030 | 59.31 | 6.95 | 85/302-10:22:52.8 | 1.9 | Blasjo ex |
| 039 | 59.31 | 6.95 | 85/310-14:50:51.4 | 2.4 | Blasjo ex |
| 501 | 58.34 | 6.43 | 85/313-14:42:45.0 | — | Titania ex |
| 094 | 59.73 | 5.71 | 85/331-04:53:32.1 | 3.0 | earthquake |
| 099 | 61.55 | 4.65 | 85/334-19:05:13.4 | 3.0 | earthquake |
| 111 | 60.19 | 5.25 | 85/341-14:15:43.2 | 2.2 | earthquake |
| 112 | 58.90 | 5.98 | 85/341-14:39:09.9 | 1.9 | earthquake |
| 158 | 58.34 | 6.43 | 85/365-13:36:49.6 | 2.1 | Titania ex |
| 196 | 58.34 | 6.43 | 86/031-14:17:35.7 | 1.9 | Titania ex |
| 522 | 62.74 | 4.50 | 86/036-23:35:41.0 | 2.6 | earthquake |
| 523 | 62.90 | 4.86 | 86/037-06:19:52.0 | 2.3 | earthquake |
| 208 | 62.90 | 4.86 | 86/037-06:20:05.4 | 1.9 | earthquake |
| 216 | 66.45 | 14.89 | 86/038-21:03:21.1 | 2.2 | earthquake |
| 524 | 62.40 | 5.28 | 86/044-13:39:00.0 | 2.5 | earthquake |
| 525 | 62.61 | 5.07 | 86/044-19:03:48.0 | 2.6 | earthquake |
| 504 | 58.34 | 6.43 | 86/045-14:13:25.0 | 2.7 | Titania ex |
| 505 | 67.10 | 20.60 | 86/045-16:44:08.0 | 2.6 | explosion |
| 506 | 58.34 | 6.43 | 86/045-17:54:11.0 | 2.3 | Titania ex |
| 526 | 58.34 | 6.43 | 86/047-18:19:41.0 | 2.0 | earthquake |
| 239 | 62.76 | 5.29 | 86/057-02:11:58.5 | 1.9 | earthquake |
| 247 | 61.67 | 2.58 | 86/067-16:21:18.3 | 1.9 | earthquake |
| 266 | 61.66 | 4.53 | 86/089-03:22:48.7 | 1.6 | earthqu: .ve |
| 270 | 58.34 | 6.43 | 86/094-13:12:43.9 | 1.9 | Titania ex |
| 298 | 59.31 | 6.95 | 86/120-10:18:48.2 | 2.2 | Blasjo ex |
| 507 | 59.31 | 6.95 | 86/147-18:36:14.0 | 2.3 | Blasjo ex |
| 508 | 59.31 | 6.95 | 86/148-17:51:57.0 | 2.4 | Blasjo ex |
| 509 | 58.34 | 6.43 | 86/157-13:14:28.0 | 1.7 | Titania ex |
| 510 | 59.31 | 6.95 | 86/170-03:55:08.0 | 2.5 | Blasjo ex |
| 511 | 58.34 | 6.43 | 86/174-13:12:54.0 | 1.8 | Titania ex |
| 512 | 59.31 | 6.95 | 86/191-20:10:42.0 | 2.3 | Blasjo ex |
| 513 | 59.31 | 6.95 | 86/197-17:49:28.0 | 2.3 | Blasjo ex |
| 514 | 59.31 | 6.95 | 86/204-20:47:10.0 | 2.2 | Blasjo ex |
| 515 | 59.31 | 6.95 | 86/210-13:13:41.0 | 2.3 | Blasjo ex |
| 516 | 59.31 | 6.95 | 86/211-17:59:39.0 | 2.4 | Blasjo ex |
| 517 | 58.34 | 6.43 | 86/226-13:14:39.0 | 1.9 | Titania ex |
| 518 | 59.31 | 6.95 | 86/226-14:39:57.0 | 2.4 | Blasjo ex |
| 519 | 59.31 | 6.95 | 86/245-12:53:51.0 | 2.1 | Blasjo ex |
| 520 | 59.31 | 6.95 | 86/252-17:55:58.0 | 2.4 | Blasjo ex |
| 503 | 58.34 | 6.43 | 86/274-14:15:10.0 | 1.9 | Titania ex |
| 521 | 58.34 | 6.43 | 86/282-14:13:52.0 | 2.0 | Titania ex |
| 407 | 61.97 | 2.33 | 86/283-19:56:29.1 | 2.1 | earthquake |
| 422 | 61.46 | 3.29 | 86/299-11:44:54.1 | 2.4 | earthquake |

Table 1.1. Event locations, origin times, local magnitudes and types.

In addition to the NORESS data, we shall use an event recorded by the NRDC high-frequency stations deployed in Kazakhstan, U.S.S.R. in 1987 (Given *et al.*, 1990). The recording we have chosen is of the calibration explosion, Chemex 2, and was made by the surface sensor at Bayanaul.

The events recorded by the NORESS array consist of earthquakes and quarry blasts which, with the exception of one event, occurred within a range of 700 km from the array. Only regional events are considered here since the analysis depends on the retention of high-frequency energy in the coda. All events fall within a local magnitude range of $1.6 \leq M_L \leq 3.0$. Event magnitudes, locations, origin times and identifications were obtained from Baumgardt and Ziegler (1988) and Sereno *et al.* (1987). All frequency-spectral estimates have been computed using a multi-taper algorithm. The rationale behind the choice of this algorithm is described in paper 1, and the theory describing this approach can be found in numerous papers, including Park *et al.* (1987) and Thompson (1982).

## 1.3 The effect of ripple-firing

At least at the macroscopic scale, the practice of ripple-firing appears to have little systematic effect on the seismic waveforms. It is well known, however, that ripple-fired events tend to give rise to seismic coda possessing highly colored spectra, that is, spectra enriched in power in certain, preferred, frequency bands and depleted in power in others (Bell, 1977; Baumgardt and Ziegler, 1988; Stump and Riemer, 1988; Smith, 1989). This spectral color is due to the interaction of the time-offset wavefields produced by each sub-explosion. Briefly, the regular repetition and superposition of similar seismic motions in the time domain leads to regular amplification and suppression of power in the frequency domain. The manner in which the wavefields interact undoubtedly involves nonlinear processes; however, we feel that simple linear theory is sufficient to describe the most obvious result, specifically the pronounced spectral modulation. As described in paper 1, and by numerous other authors (Baumgardt and Ziegler, 1988; Stump and Reinke, 1988; Smith, 1989; Stump *et al.*, 1989) this model makes the assumptions that the wavefields produced by each sub-explosion w(t) are identical and that they superpose linearly. Forcing all shots to occur at regular time-intervals T we can construct the wavelet produced by the ensemble of sub-explosions (lasting a total of D seconds) by the equation:

$$ r(t) = w(t) * \left[ \frac{1}{T} III(\frac{t}{T}) B(\frac{t}{D}) \right] \tag{1.1} $$

where * represents convolution. Here, $III$ is the shah function (Bracewell, 1986) and B is the boxcar

function. Hereafter we refer to this representation as model 1. By Fourier transforming this expression we see that the spectrum of the entire seismogram equals that of an individual event multiplied by a set of equispaced sinc functions - collectively referred to as the modulation function:

$$\tilde{X}(f) = \tilde{W}(f)\left[III(fT) * \frac{\sin(\pi f D)}{\pi f}\right] \tag{1.2}$$

In Figure 1.2 we display the modulation function resulting when 39 sub-explosions spaced at 25 ms are superposed in this manner. Primary reinforcement occurs at multiples of 40 Hz (the loci of the main-lobes of the sinc functions). The side-lobes have insignificant amplitudes relative to the main-lobes. They can, however, in theory allow us to compute the duration of the entire quarry blast. The duration, D, is given by the inverse of the width of a single sidelobe. In the event displayed in Figure 1.2, this value is 0.975 seconds, the known duration of the set of explosions. As discussed in paper 1, using the model described above, we predict that the modulation produced by ripple firing should be independent of time in the coda. In paper 1 we found that this predicted character can be investigated efficiently by the computation of frequency-time displays known as sonograms (Markel and Gray, 1976; paper 1). In Figures 1.3 and 1.4 are displayed the sonograms computed from the coda generated by an earthquake and a quarry blast respectively. The quarry blast (Figure 1.4) clearly shows a time-independent spectral modulation whereas the earthquake (Figure 1.3) does not. Often the two types of events do not contrast as well as these examples do when presented in this format. For this reason we have found it beneficial to convert the spectral estimates to binary form. The means by which we accomplish this conversion is discussed fully in the paper 1, and involves comparing a relatively unsmoothed version of each spectrum with a more heavily smoothed one that resolves only the large scale structure, in order to extract the regular modulation. In practice, when analyzing the events considered in this chapter, we simply convolved the spectra with boxcar functions spanning 1.0 and 2.5 Hz respectively. We then represent all sections of the spectra where the local power is high relative to the more regional average power by a value of +1 and where it is low by a value of -1. In this manner the bulk of the magnitude information is discarded and the spectra are "flattened" to very simple binary patterns. When analyzing array data, we generalize the procedure by computing such a binary pattern for each trace individually, and then stacking all the patterns. Because the procedure is quite nonlinear, this is very different from computing binary sonograms from beams as in Figures 1.3 and 1.4. As illustrated below, stacking *after* reduction to binary patterns is a more effective approach for our present purposes. In Figures 1.5 and 1.6 we display array stacks of the binary sonograms computed for the events displayed in Figures 1.3 and 1.4
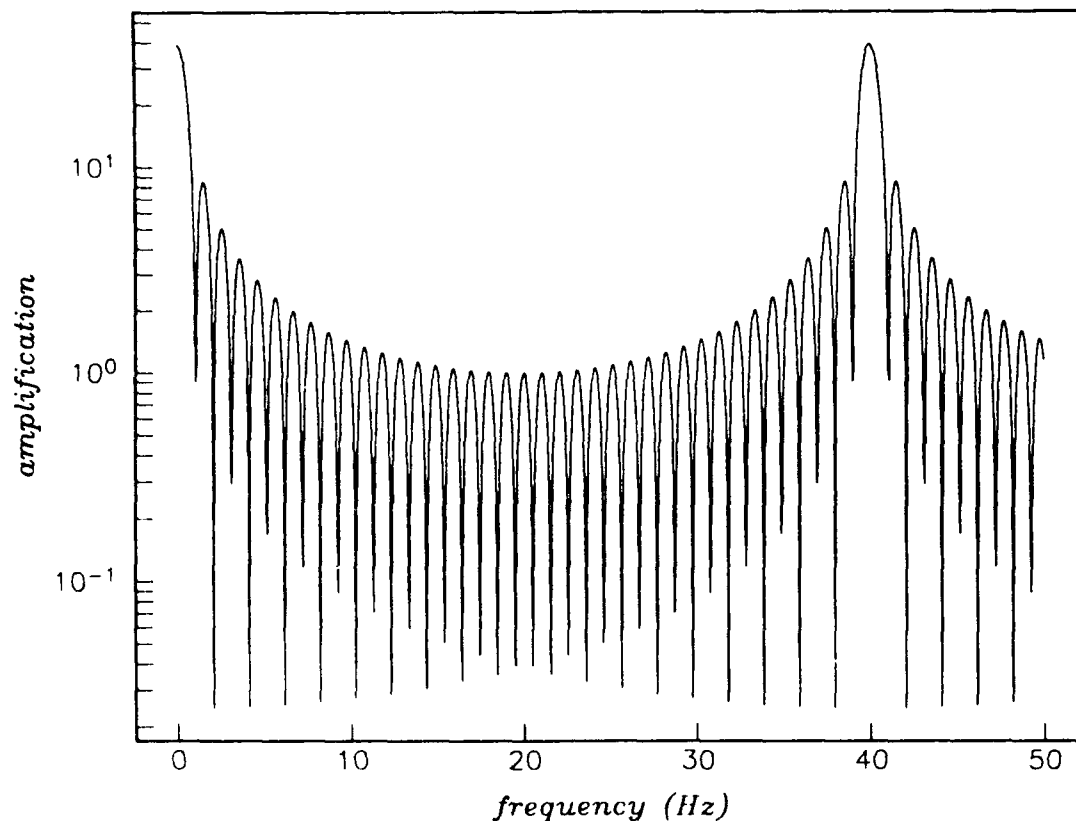
Figure 1.2 Spectral modulation predicted for an event consisting of 39 sub-explosions located at the same point in space and offset evenly in time at 25 ms.

respectively. Since typically 25 vertical sensors simultaneously record each event, the values in these binary stacks typically range from -25 to +25. The original spectral estimates have been corrected for noise by subtracting an average pre-event sample. Time-independent spectral modulation is present after the onset in the coda of the quarry blast only. This spectral character is not unique to this event but is shared by virtually all the events identified in Table 1.1 as explosions.


## 1.4 The cause of the observed spectral modulation

The simplest explanation of the observed spectral modulation is, as discussed in the previous section, that it is due to ripple-firing. The main argument against this explanation is that the inferred delay times at the source are extremely long. Spectra computed from a typical event (030 - pictured in Figures 1.4 and 1.6) have power highs spaced at roughly 5 Hz leading to an inferred average shot spacing
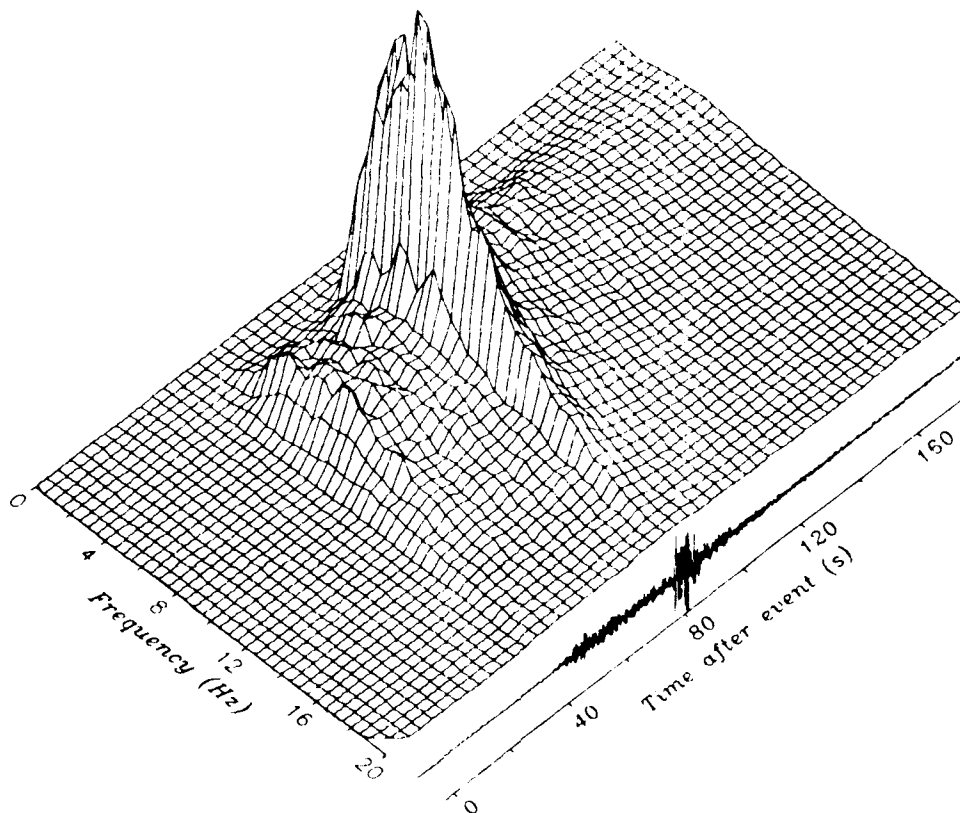
8

**Figure 1.3** Seismogram resulting from an earthquake located 342 km from NORESS (event 094) and corresponding sonogram. In Figures 1.3 through 1.6 the sonograms have been computed from a stack of 25 spectra, each computed from an individual vertical channel in the NORESS array. The stacks were computed after offsetting the seismograms to beamform for the $P_g$ phase. In addition all spectral estimates have been corrected for noise and the instrument response. The spectral amplitudes in figures 1.3 and 1.4 are shown on a linear scale.

of 200 ms. In paper 1 we inferred delay times as high as 400 ms at quarries in Kazakhstan, U.S.S.R. As Baumgardt and Ziegler (1988) mention, "slow delays" (from 500 to 1000 ms) are used in subsurface mining where the intent is to use a shot to remove material prior to the next shot. We have reason to believe, however, that the explosions considered in paper 1 and the current data set did not occur in the subsurface.

With the aid of satellite (SPOT) photos we know that a number of the mines in Kazakhstan are at the free surface (Thurber *et al.*, 1989). The Blasjo explosions are known to be associated with the construction of a dam (Baumgardt and Ziegler, 1988). As discussed by several authors (including Langefors and Kihlström, 1978) the short delays employed at free-surface mining operations generally
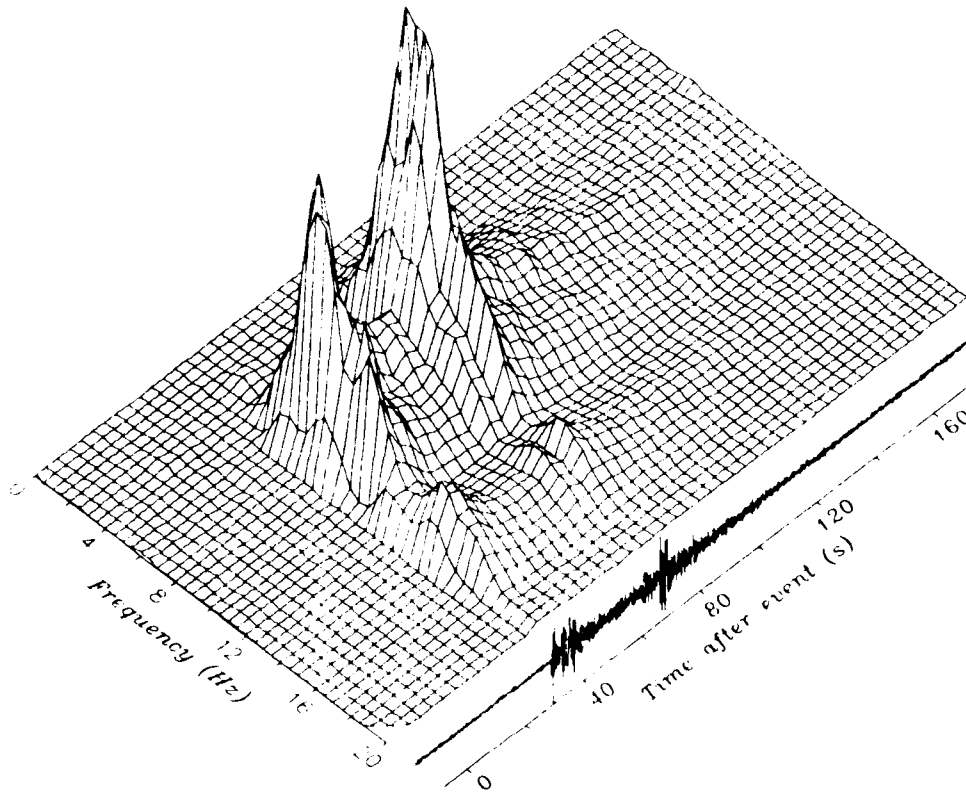
9

Figure 1.4 Seismogram resulting from a quarry blast located 301 km from NORESS (event 030) and corresponding sonogram.

fall in the range from 1 to 100 ms and are typically on the order of 20 to 30 ms. Using the model described in the previous section, and 30 ms offsets, we predict spectral amplification at multiples of 33 Hz - well beyond the Nyquist frequency of the NORESS data set. It is conceivable that the closely spaced modulations (shown in Figures 1.4 and 1.6) could be an artifact of multiple-row blasting where short delays are used between successive shots in each row, but adjacent rows are spaced by significantly greater delays. Synthetic experiments, in which modulation functions are computed for a variety of quarry blast configurations, suggest that this is a plausible argument; however, realistic examples taken from the literature do not. For example, Stump *et al.* (1989) describe multiple-row quarries which have interrow time spacings of 42 ms. This argument does not rule out slow delays, either between successive shots or adjacent rows, but suggests that we should look for alternative explanations for the observed spectral modulation.

As discussed in paper 1 and Hedlin *et al.* (1988) it is possible for a wavefield to acquire a

time after event (s)

0    20    40    60    80    100    120    140    160    180
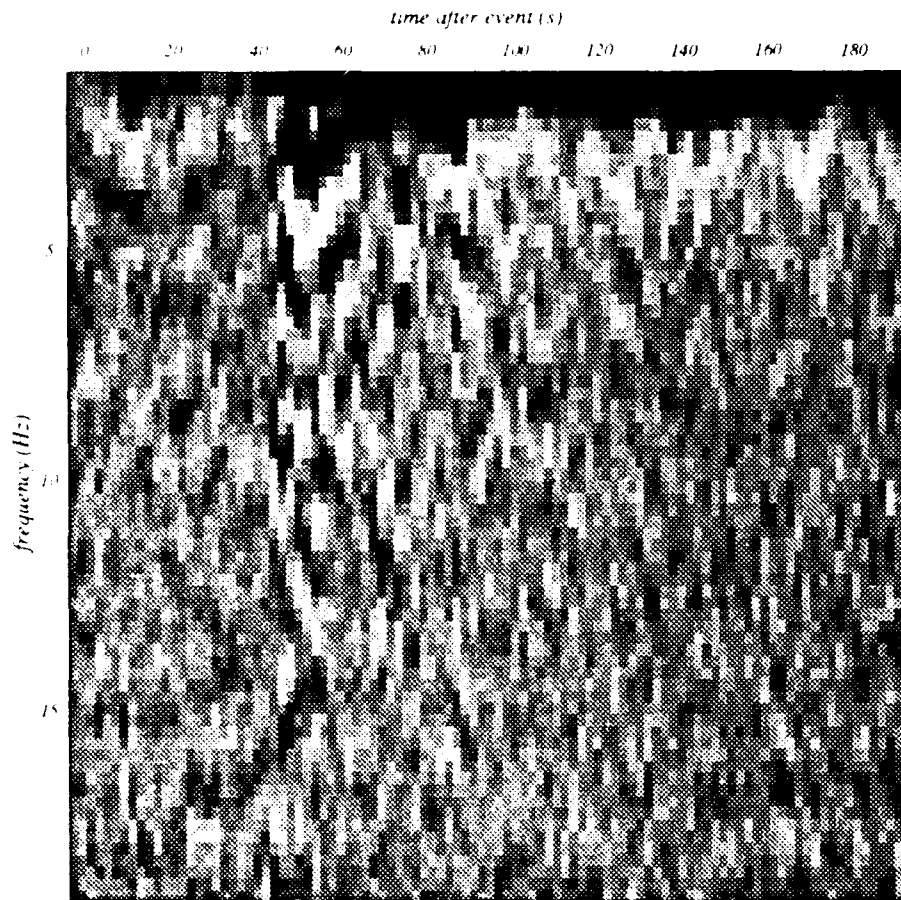
frequency (Hz)

s

10

15

Figure 1.5 Seismogram resulting from the earthquake presented in Figure 1.3 (094) and corresponding binary sonogram. The conversion to binary form was performed on each channel before stacking.

time-independent spectral modulation during propagation by resonating in low velocity layers. The most likely locations of layer resonance are in low velocity sediments or weathered strata near the free-surface close to the source and/or the array. Considering that many of the recorded events have given rise to unmodulated spectra it is clear that no significant near-receiver resonance is taking place. Furthermore, since different modulation patterns are commonly produced by different events with the same location (such as successive mine explosions at the same mine), the modulations are clearly not due to near source resonance. We conclude that the spectral modulation is most likely due to intrinsic source processes.

A third explanation relies again on source multiplicity. The modulation function produced by model 1 is dominated by the main lobes of the sinc functions. These are the only features that can realistically be expected to produce observable spectral peaks when the time delays are perfectly regular. Model 1, however, does not describe a very likely quarry blast. As discussed by many authors (including
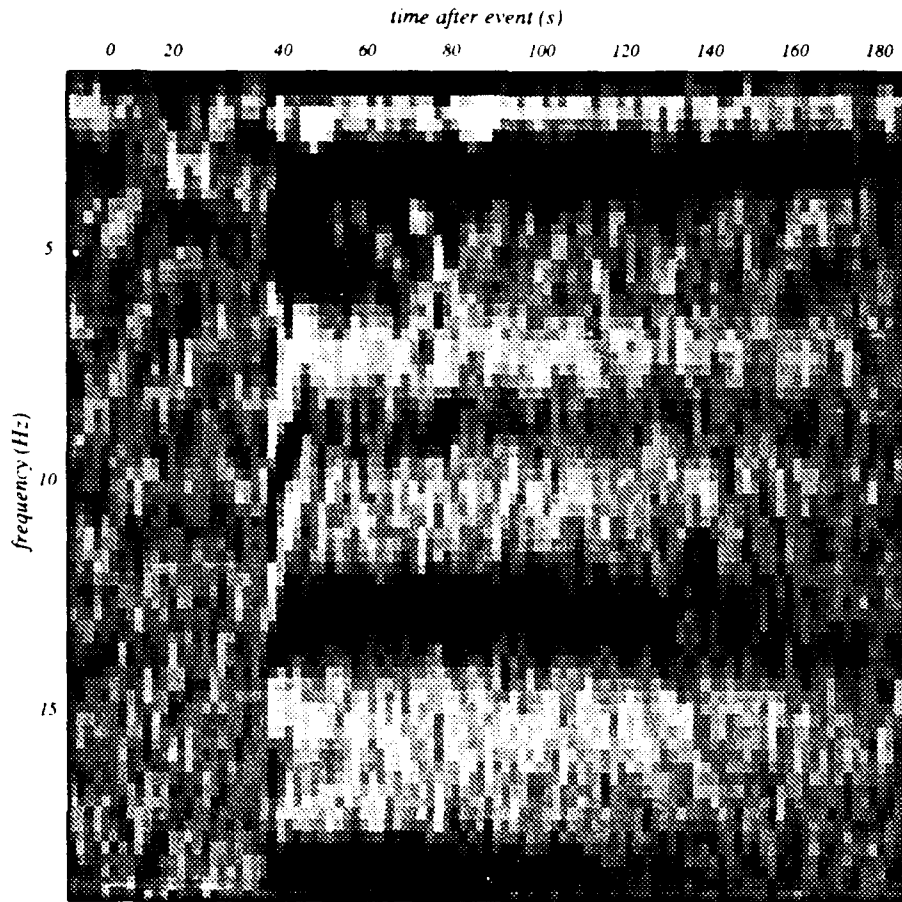
**Figure 1.6** Seismogram resulting from the quarry blast presented in Figure 1.4 (030) and corresponding binary sonogram.

Langefors and Kihlström, 1978; Dowding, 1985 and Stump *et al.*, 1989) ripple-fired shots in quarries are spatially offset, usually in a regular pattern. At each shot location there are sometimes several vertically offset (decked) charges. The time-delays between the shots, especially in multiple row blasting, are not necessarily going to be consistent. Actual shot times often deviate a considerable amount from the intended times (Stump and Reamer, 1988). Knowing the near-surface velocity and the slowness (p) of the energy under consideration we can replace actual time and space offsets ($\delta T_i$ and $\delta X_i, \delta Y_i$) with apparent time offsets $\delta T_i^a$ by noting that:

$$\delta T_i^a = p(\delta X_i \sin\theta - \delta Y_i \cos\theta) - \delta T_i \qquad (1.3)$$

The azimuth from the quarry to the receiver is given by $\theta$. All the aforementioned factors can cause a considerable deviation of the apparent times of the sub-explosions from a common value. Using these

apparent time-offsets, and assuming linear superposition and commonality of basis wavelet w(t), we can construct the wavelet due to a more general quarry blast.

$$x(t) = \sum_{i=1}^{n} w(t - \delta T_i^a)$$  (1.4)

In the frequency domain this expression is equivalent to:

$$\tilde{X}(f) = \tilde{W}(f)[(\sum_{i=1}^{n} cos(2\pi f \delta T_i^a))^2 - (\sum_{i=1}^{n} sin(2\pi f \delta T_i^a))^2]^{\frac{1}{2}}$$  (1.5)

Scatter in the apparent times of the sub-explosions reduces the dominance of the main lobes, or equivalently, lets the side-lobes rise into prominence (paper 1). To illustrate this point we have computed a theoretical modulation pattern for a quarry blast layout adapted from that of a real life quarry, the San Vel quarry, described and studied by Stump and Reimer (1988) and Stump et al. (1989). As displayed in Figure 1.7 the sub-explosions are arranged in an en echelon pattern. The shots in each row are spaced at 25 ms proceeding from west to east. The row detonations are separated by 42 ms proceeding from south to north. The modulation functions, computed for energy traveling to observation points due north and east of the quarry with a slowness of 1/7 s/km, are displayed in Figure 1.8. Although the dominant delay time is 25 ms, the 40 Hz peak does not dominate either modulation function. The function for the station to the north can be constructed by multiplying the modulation function due to 13 shots spaced at 25 ms (representing the intershot delays) with the function corresponding to 3 shots spaced at roughly 42 ms (representing the inter-row delays after taking into account the delay associated with the propagation of the energy between the rows). The two functions are in competition, and the result is that the broad main-lobes of the latter accentuate the side-lobes of the former to a point where they can be expected to have a significant impact on the spectrum of the quarry blast.

Using a technique employed in paper 1 we synthesize a quarry blast using the apparent sub-explosion times occurring in the event described above. We assume a common waveform is generated by each sub-explosion and for that waveform we select the calibration explosion Chemex 2 detonated in Kazakhstan, U.S.S.R. and recorded at the station at Bayanaul. (We have resorted to this data set simply because the 40 Hz NORESS data do not have adequate resolution in time to permit the millisecond offsets required by this quarry.) The Chemex 2 recording was made at 250 $s^{-1}$. This "Green's function" is linearly stacked upon itself 39 times after including the offsets appropriate for the observation point due north of the quarry. Although we have chosen to create the synthetic quarry blast by offsetting and stacking a Green's function in the time domain, the equivalent result could be achieved by multiplying
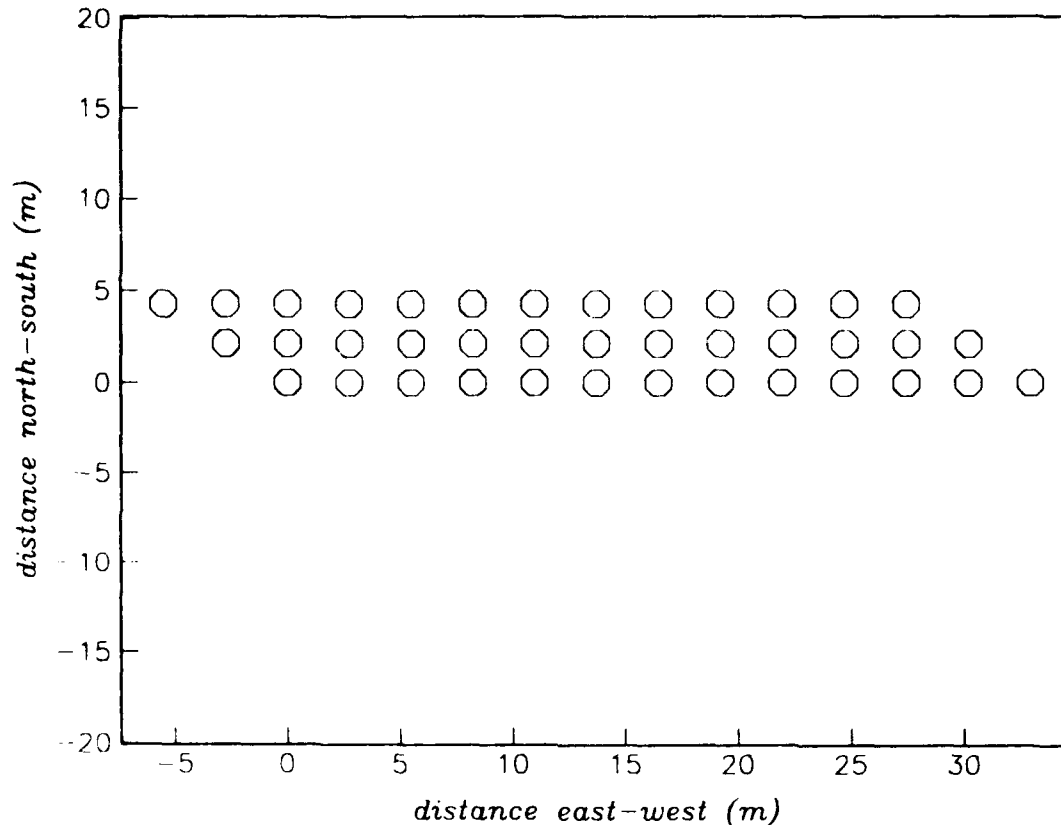
Figure 1.7 The layout of sub-explosions in an en echelon quarry blast. Shooting within the rows is spaced in time at 25 ms. Adjacent rows are separated by 42 ms in time. This pattern is adapted from Stump *et al.* (1989).

the spectrum of the Green's function by the complex modulation function which underlies the solid curve pictured in Figure 1.8. Prior to computing the sonogram, the "synthetic" seismogram was low-pass filtered between 0 and 20 Hz and decimated to one point in 5 to mimic a NORESS recording. The sonogram (displayed in Figure 1.9) is dominated by time-independent structure. Assuming this modulation pattern was due to main-lobe activity, one would estimate a dominant delay time to be roughly 170 ms (the inverse of 6 Hz). We know, however, that this structure is due to side-lobe activity and is controlled in this case by the total duration of the quarry blast. Because of the manner in which the sonogram is calculated, the frequency estimates are heavily smoothed. Longer time windows would allow a more accurate estimate of the frequency spacing of the modulation. In fact we know that the average sidelobe width is roughly 2.6 Hz (see Figure 1.8) and that the duration of the quarry blast is 384 ms.

It seems that there is a fundamental ambiguity in the spectral modulation produced by ripple-
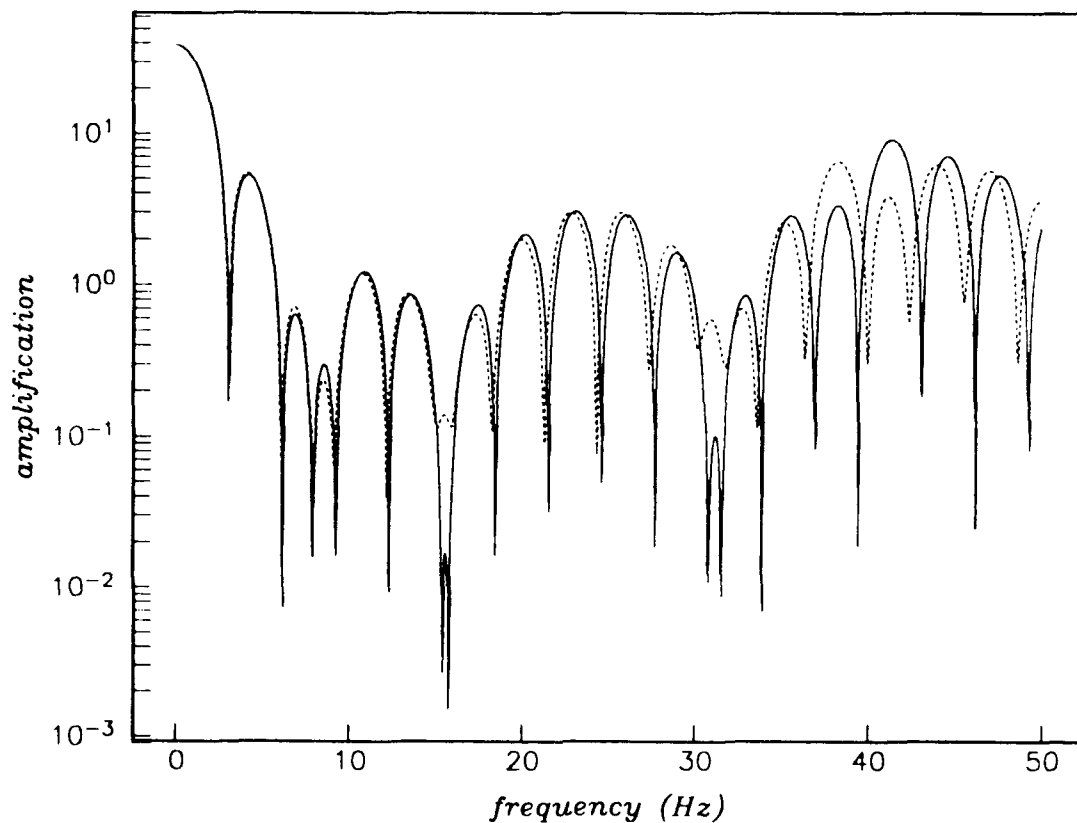
14

**Figure 1.8** The amplitude of modulation functions resulting from the shot introduced
in Figure 7. The solid and dashed curves represent energy traveling at a slowness of
$1/7$ s km $^1$ to stations due north and east of the quarry respectively.

fired, and hence non-instantaneous, events. Without *a priori* information about what occurred at the source we cannot be sure if the modulation spacing is controlled by the duration of the entire set or by the dominant inter-shot apparent time spacing. This experiment shows that our discriminant, perhaps, will not recognize quarry blasts because they are ripple fired per se, but because they last an intermediate length of time. Instantaneous events give rise to unmodulated spectra. Extremely long events (for example large earthquakes) should produce very finely modulated spectra, such that the modulation is masked by scattering and noise.

In paper 1 we considered two types of events - calibration explosions which were detonated by American and Soviet scientists (Given *et al.*, 1990) and did not involve ripple firing. Using *a priori* information we strongly suspected the rest of the events were quarry blasts. This information included satellite photos, provided by Prof. Clifford Thurber (at the University of Wisconsin), which showed
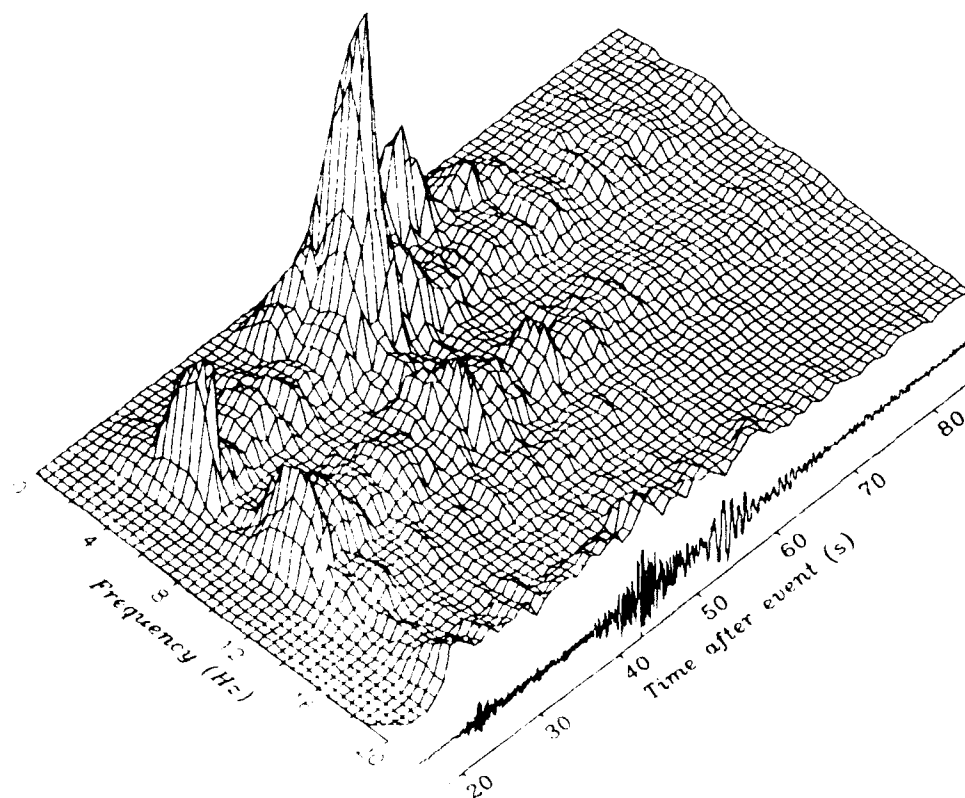
15

**Figure 1.9** Time series and sonogram representing a "synthetic" quarry blast. The synthetic was constructed by linearly stacking a seismogram produced by the Chemex 2 explosion in Kazakhstan U.S.S.R. upon itself after offsetting in time to mimic the quarry pictured in Figure 1.7 when observed from a point to the north (see Figure 1.8). The original seismogram was sampled at 250 s$^{-1}$. The synthetic was low pass filtered and decimated to simulate recording conditions similar to the NORESS array.

surface mining activity in the vicinity of some of the events. In addition it is known that the region has little natural seismicity (Leith, 1987). Time independent spectral modulation was only observed in the latter set of events and was attributed to the source multiplicity. The present study and the previous one are consistent in suggesting that quarry blasts can be discriminated from non ripple-fired events.

## 1.5 The automatic discriminant

For our purposes it is irrelevant whether the time independent spectral features observed in the coda produced by quarry blasts are due to main lobes or to sidelobes in the modulation functions. Ripple fired events tend to give rise to time independent spectral modulation, the earthquakes examined in this

study do not. To examine this modulation we have developed a means to "expand" a time series into a matrix of numbers depending on frequency and time. Typical patterns obtained from recordings of an earthquake and a quarry blast (Figures 1.5 and 1.6) illustrate that it can be very easy to discriminate visually between these two types of events given these time-frequency displays. In paper 1, using the same approach, we found a similar degree of success in discriminating between quarry blasts and single-event explosions. Given the current interest in the problem of discriminating quarry blasts from earthquakes and single-event explosions and the large numbers of events involved, we feel it is important to extend the algorithm so that human intervention is distanced from the discrimination process, to a point where the patterns can be recognized automatically by the computer. One method we have found to be very effective involves the computation of a two-dimensional Fourier transform of the sonogram matrices. This can be considered as an extension of *cepstral* analysis (Tribolet, 1979). In the standard cepstral analysis a Fourier transform of the log of the amplitude spectrum is computed to highlight any regular spectral modulation regardless of its longevity. The independent variable is known as the *quefrency* and has units of time. The form of cepstral analysis we are proposing is more demanding, however. A given point in the 2-D cepstral matrix not only represents spectral modulation at a certain quefrency, but periodic along the time axis at a certain frequency. It is thus a simple matter to isolate energy periodic in frequency and independent of time.

To illustrate our point we display two 2-D cepstra in Figures 1.10 and 1.11. The first was computed from the first 100 seconds of coda of event 030 (Figures 1.4 and 1.6), the second was computed from the coda of the earthquake 094 (Figures 1.3 and 1.5). The quarry blast has significantly more energy at zero frequency (along the time axis) than the earthquake. The quefrency at which the power is concentrated in the 2-D cepstrum computed from the coda produced by the quarry blast is roughly 0.2 seconds (reflecting the spectral modulation with 5 Hz spacing. Slices at zero time-frequency through 2-D cepstra computed from the coda produced by a quarry blast (event 507) and all the earthquakes in the data set are shown in Figure 1.12. As expected, the quarry blast is a singular event. The most noticeable feature in the quarry blast cepstrum is, obviously, the significant peak at a quefrency of 0.2 seconds. We expect that ripple-fired events should give rise to significantly larger extreme cepstral values than earthquakes. Supporting this thesis are the histograms in Figure 1.13 showing the observed distributions of cepstral extremes for the entire earthquake and quarry blast populations examined in this study.

Although we are most interested in the quarry blast cepstra, we can gain some important insight from the earthquake cepstra which illustrate the 2-D cepstral structure that can be expected in the absence of source multiplicity. These cepstra show what time-independent structure will be acquired by
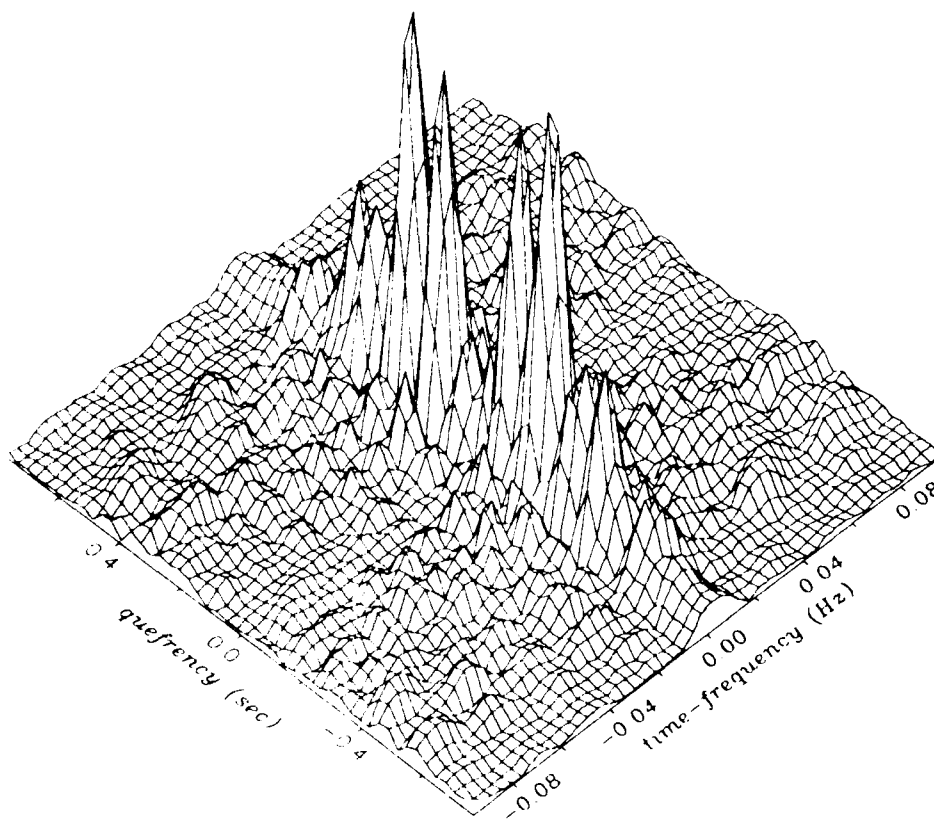
Figure 1.10 Two-dimensional cepstrum computed from the coda produced by a quarry blast (event 030). The first 100 seconds of the coda were considered.

a propagating wavelet or, in other words, they are indicative of the region's natural level of resonance. We propose to identify events as quarry blasts by searching for anomalously high global extrema in the time-independent segments of the 2-D cepstra. To calibrate the algorithm, to account for the natural resonance in the region, we make the judgment of what is a large value on the basis of what extrema non-ripple-fired events produce. The consideration of global extrema in these 2-D cepstra is a problem that is well suited for analysis using the statistics of extremes (Gumbel, 1958).

In Figure 1.13 it is clear that the logs of the extreme amplitudes are centrally distributed, and there are no significant outliers. The Kolmogorov-Smirnov test suggests that the earthquake cepstral extremes follow a log-normal distribution. However we would like to avoid the adoption of a specific underlying distribution since we have no fundamental reason for choosing one and since we only have 16 earthquakes. It is known (e.g., Gumbel, 1958 and Weissman, 1978) that when dealing with observations of extreme values the underlying distribution need not be assumed, but the behavior can be modeled using
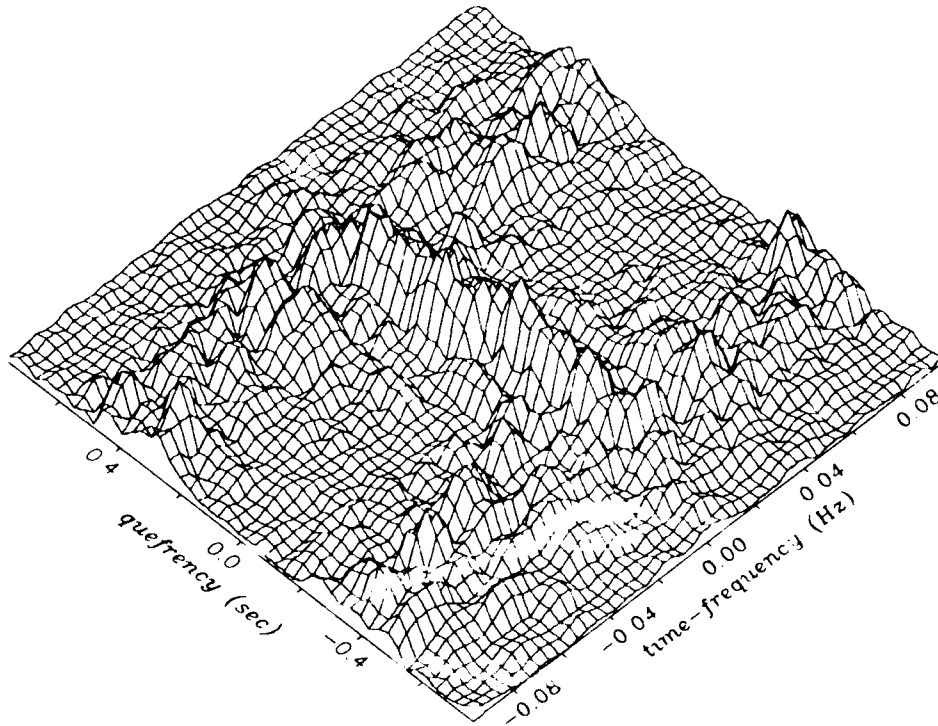
18

**Figure 1.11** Two-dimensional cepstrum computed from the coda produced by an earthquake (ev^nt 094). The first 100 seconds of the coda were considered.

functions that are asymptotically valid as the number of samples examined and the number of points in each sample approaches infinity (Kennedy and Neville, 1974). Selecting the exponential asymptote, the cumulative probability (P) that an extremum belonging to the earthquake population will be less than the one observed is given b;.

$$P = e^{[-e^{(-y)}]} \tag{1.6}$$

where the expression for the reduced variate (y) is:

$$y = a(u - \hat{u}) \tag{1.7}$$

The terms a and $\hat{u}$ are the dispersion parameter and the mode of the distribution respectively and are estimated directly from the population of earthquake extremes shown in Figure 1.13 (Kennedy and
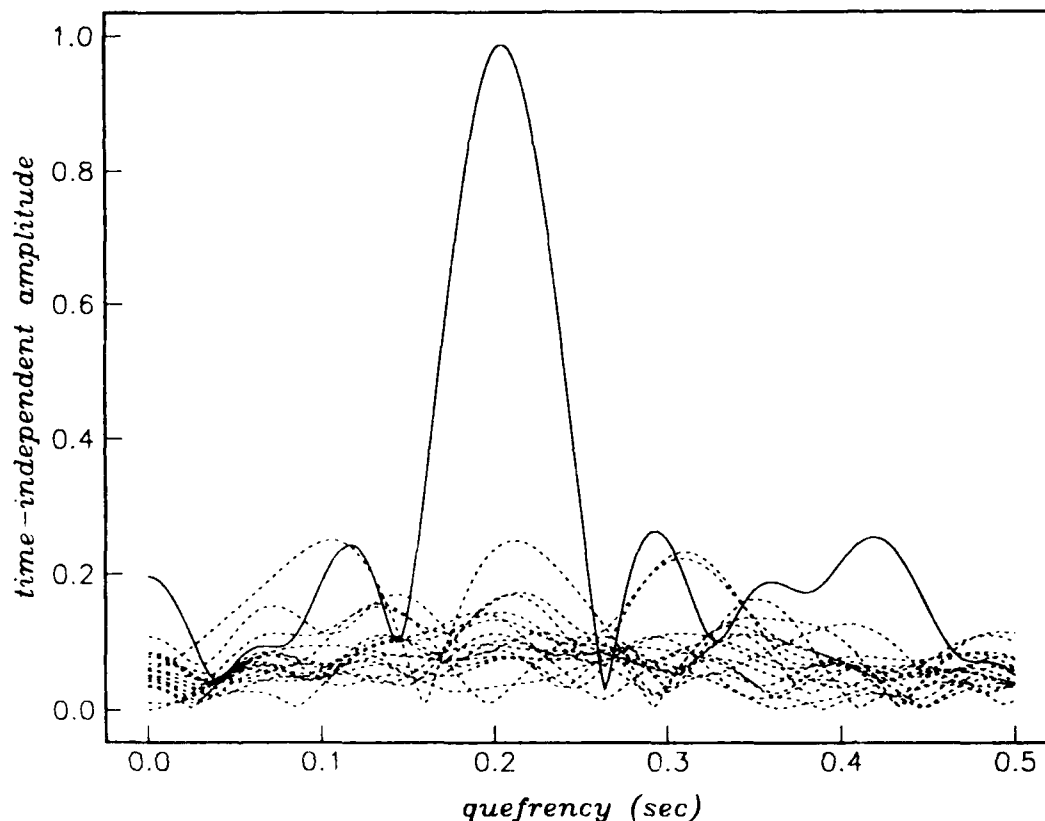
19

Figure 1.12 Slices through the time-independent portions of two-dimensional cepstra computed from a quarry blast (event 507) and all the earthquakes considered in this study. The quarry blast is shown as the solid line.

Neville, 1974). The log of the cepstral extremum of interest is represented by u. We find that for this distribution a and û equal 7.204 and 3.55, respectively.

Given this probability function we can pose the discrimination problem in terms of a standard hypothesis test: Let the null hypothesis ($H_0$) be that a newly recorded event belongs to the population of earthquakes used to calibrate the technique. If the cepstral extremum calculated for this event exceeds a certain threshold determined from the distribution (1.6), then we can reject the null hypothesis ($H_0$) at a preset confidence level, and conclude that the event is probably a quarry blast. For example, on Figure 1.14, this threshold was selected such that for points that plot above the threshold line, the null hypothesis is rejected with only a 5% risk of doing so erroneously. In other words, we state that events above the line do not belong to the earthquake population, at the 95% confidence level. In spite of the apparent efficiency of the discriminant illustrated on Figure 1.14, we must remember that the calibration
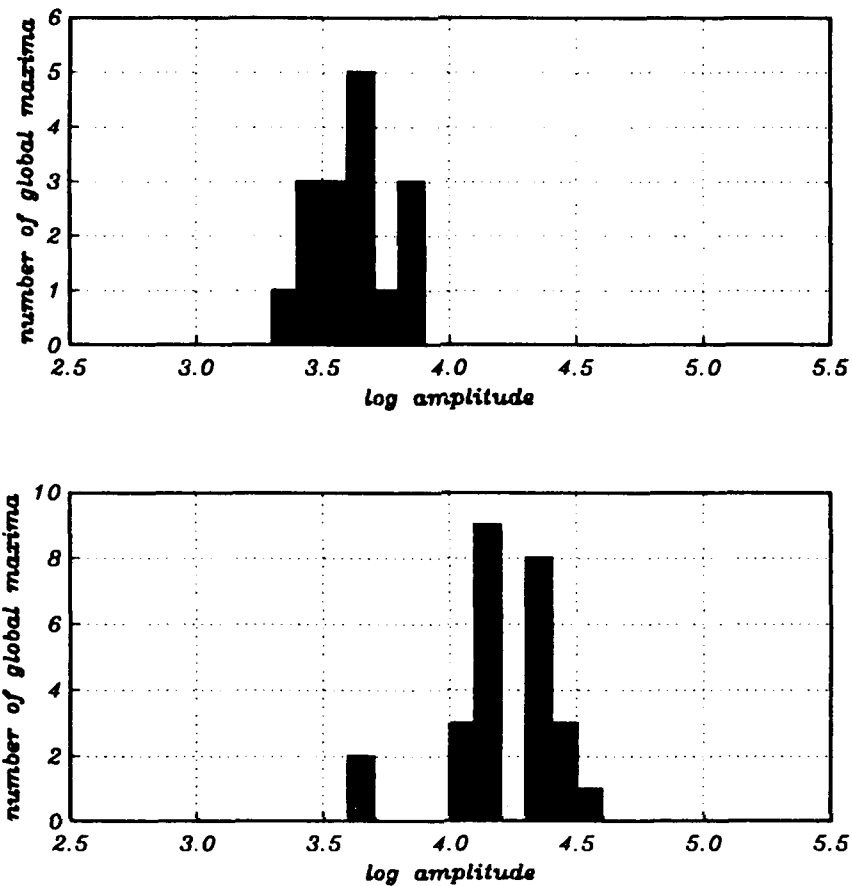
20

**Figure 1.13** Histograms showing the observed distributions of global extreme cepstral values computed from the coda produced by earthquakes (top) and quarry blasts (bottom).

of the distribution (8) is based on our (small) sample of 16 identified earthquakes, so that the test is in fact "data fitted". Confirmation of our claim of success will have to be based on an independent sample. In this figure the symbol size is directly proportional to the signal to noise ratio (derived from average spectra encompassing the time from 50 seconds before and after the compressional onset). Of the 26 quarry blasts considered, 23 lie above the 95% confidence level. Of the two that fall well below this limit, one (event 505 - located in northern Sweden) had extremely low signal to noise levels (less than 10 dB) and the other (event 504) produced only a very broad spectral modulation. The three earthquakes located above a probability of 0.8 (events 112, 523 and 208) all suffered from signal to noise ratios less than 10 dB.
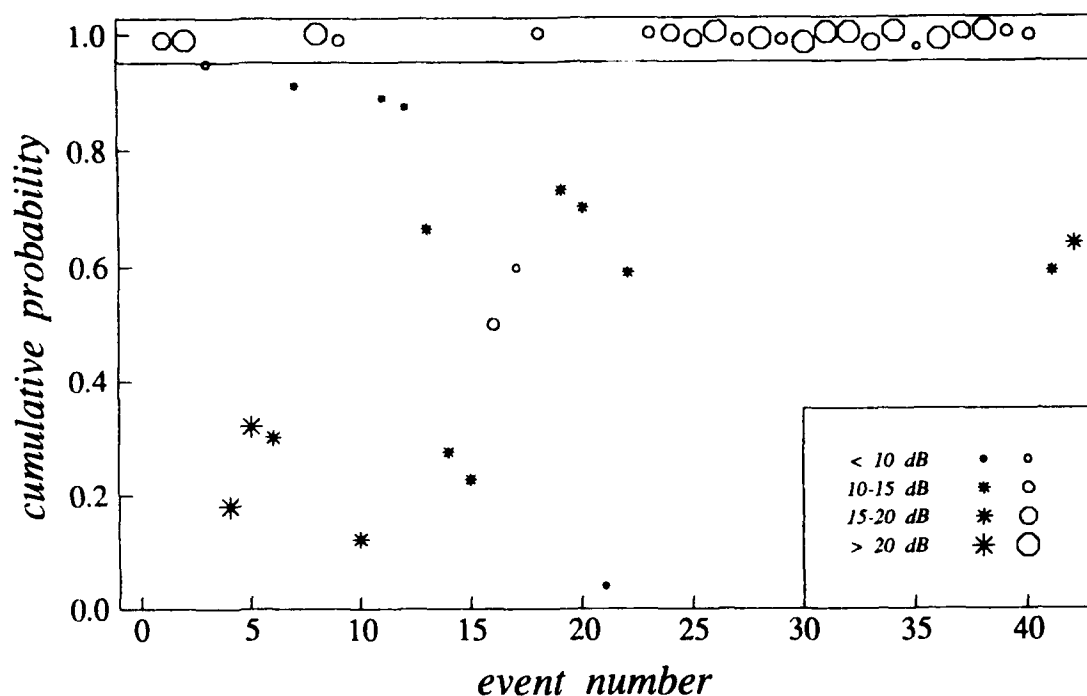
21

**Figure 1.14** The cumulative probabilities of extreme cepstral values derived from the coda produced by all events in the data set. The quarry blasts are denoted by octagons, the earthquakes are represented by stars. The likelihood that the assumption that the event is an earthquake is invalid increases with this probability. For points above the 0.95 threshold, the hypothesis that the corresponding events belong to the earthquake population is rejected at the 5% risk level. The event number (along the horizontal axis) indicates the location of the event in table 1.1. The symbol size scales with the signal to noise ratio (see insert).

## 1.6 Conclusions

In paper 1 we advanced the preliminary observation that ripple-fired events tend to give rise to coda dominated by time-independent spectral features and that this quality should be exploited to discriminate these events from earthquakes and single-event explosions.

In this chapter we have demonstrated that this can also be done with a high degree of success when considering earthquakes and quarry blasts. We have found that quarry blasts tend to produce modulated spectra, but the modulations may not result directly from the ripple-firing; they may exist simply because the event is non-instantaneous. We have produced an empirical, calibrated, approach to the discrimination problem which allows for local seismic resonance. We have automated the approach to the point where discrimination can be carried out solely by the computer. We have examined a data set consisting of 26 quarry blasts and 16 earthquakes and have found that with few exceptions the two populations are well separated by our approach. The events which failed to be identified with a high

22

degree of confidence generally suffered from low signal to noise ratios.

By comparing our current results with those in the earlier work we have illustrated the ability of the algorithm to accommodate changes in the recording environment, local geologic setting and mining practice. Based on the results presented in paper 1, we expect that we would have a similar degree of success in discriminating between single-event explosions and quarry blasts.

## 1.7 Acknowledgments

# References

Baumgardt, D. R. and Ziegler, K. A., Spectral Evidence for Source Multiplicity in Explosions: Application to Regional Discrimination of Earthquakes and Explosions. *Bull. Seismol. Soc. Am.*, **78**, 1773-1795, 1988.

Baumgardt, D. R. and Ziegler, K. A., Automatic recognition of economic and underwater blasts using regional array data. *Science Applications Incorporated, 11-880085-51*, 1989.

Bell, A. G. R., A Digital Technique for Detection of Multiple Seismic Events. *EOS, Trans. of the American geophys.Union*, **57**, 444, 1977.

Bracewell, R. N., *The Fourier transform and its applications*. McGraw-Hill Book Compan, 1986.

Bungum, H., Mykkeltveit, S. and Kværna, T., Seismic noise in Fennoscandia, with emphasis on high frequencies. *Bull. Seismol. Soc. Am.*, **75**, 1489-1513, 1985.

Dowding, C.H., *Blast vibration monitoring and control*. Prentice-Hall international series in civil engineering and engineering mechanics, 1985.

Given,H.K., Tarasov, N.T., Zhuravlev, V., Vernon, F.L., Berger, J. and Nersesov, I.L., High-Frequency Seismic Observations in Eastern Kazakhstan, U.S.S.R., with emphasis on chemical explosion experiments. *J. Geophys. Res.*, **95**, 295-307, 1990.

Gumbel, E. J., *Statistics of extremes*. Columbia University Press, New York and London, 1958.

Hedlin, M. A. H., Orcutt, J. A. and Minster, J. B. (1988). A Comparative Study of High Frequency Signal and Noise in Oceanic and Continental Environments. Contributed paper at "*10th annual AFGL/DARPA seism. Res. Symp*", held in Falbrook, CA.

Hedlin, M. A. H.,Orcutt, J. A., Minster, J. B. and Gurrola, H. (1989a). The time-frequency characteristics of quarry blasts, earthquakes and calibration explosions recorded in Scandinavia and Kazakhstan, U.S.S.R.. Contributed paper at "*11th Annual AFGL/DARPA Seismic Research Symposium*", held in San Antonio, TX.

Hedlin, M. A. H., Minster, J. B. and Orcutt, J. A., The time-frequency characteristics of quarry blasts and calibration explosions recorded in Kazakhstan, U.S.S.R.. *Geophys. J. Int.*, **99**, 109-121, 1989b.

Kennedy, J. B.and Neville, A. M, *Basic statistical methods for engineers and scientists*. Harper and Row, 1974.

Langefors, U. and Kihlström, B., *The modern technique of rock blasting*. Halsted Press, John Wiley and sons, New York, 1978.

Leith, W., Geology of NRDC seismic stations in Eastern Kazakhstan, U.S.S.R.. *U.S.G.S. Open-File Report 87-597*, 1987.

Markel, J. D. and Gray, A. H. Jr., *Linear Prediction of Speech*. Springer-Verlag, Berlin Heidelberg New York, 1976.

Mykkeltveit, S., Local geology of the regional array sites in Norway. *Norsar Semiannual Technical Summary, Scientific Report No. 1-87/88*, 1987.

Mykkeltveit, S., Åstebol, K., Doornbos, D.J. and Husebye, E.S., Seismic array configuration optimization. *Bull. Seismol. Soc. Am.*, **73**, 173-186, 1983.

Park, J., Lindberg, C. R. and Vernon, F. L., Multitaper Spectral Analysis of High-Frequency Seismograms. *J. Geophys. Res.*, **92**, 12675-12684, 1987.

Richards, P., Nuclear test ban treaties and seismic monitoring of underground nuclear explosions: an overview of the historical, technical and political issues. *the Alan S. Attardo Symposium on Science and Society,* 1988.

Ringdal, F. and Husebye, E. S., Application of arrays in the detection, location, and identification of seismic events. *Bull. Seismol. Soc. Am.* , 72, S201-S224, 1982.

Sereno, T. J. Jr., Bratt, S.R. and Bache, T.C., Regional wave attenuation and seismic moment from the inversion of NORESS spectra. *unclassified semiannual report, Air Force Geophysics Laboratory, AFGL-TR-87-0237, ADA 187399,* 1987.

Smith, A. T., High-Frequency Seismic Observations and Models of Chemical Explosions: Implications for the Discrimination of Ripple-Fired Mining Blasts. *Bull. Seismol. Soc. Am.* , 79, 1089-1110, 1989.

Stump, B. W. and Reamer, S. K. (1988). Temporal and Spatial Source Effects from Near-Surface Explosions. Contributed paper at *"10th annual AFGL/DARPA seism. Res. Symp",* held in Falbrook, CA.

Stump, B.W. and Reinke, R.E., Experimental confirmation of superposition from small-scale explosions. *Bull. Seismol. Soc. Am.* , 78, 1059-1073, 1988.

Stump, B. W., Reamer, S. K., Anderson, D., Olsen, K. and Reinke, R., Quantification of explosion source characteristics from near source, regional and teleseismic distances. *unclassified final report, Geophysics Laboratory, GL-TR-89-0194, ADA 216218,* 1989.

Thompson, D. J., Spectrum Estimation and Harmonic Analysis. *IEEE Proc,* 70, 1055-1096, 1982.

Tribolet, J. M., *Seismic Applications of Homomorphic Signal Processing.* Prentice-Hall Signal Processing Series, 1979.

Thurber, C. H., Given, H. and Berger, J., Regional seismic event location with a sparse network: application to eastern Kazakhstan U.S.S.R.. *J. Geophys. Res.* , 94, 17767-17780, 1989.

Weissman, I., Estimation of parameters and large quantiles based on the k largest observations. *Journal of the American Statistical Association,* 73, 812-815, 1978.

# Chapter 2

# The migration of small-aperture array recordings
# to image local crustal scatterers

## Abstract

This chapter is concerned with the development of a technique to scan seismic coda recorded by single small-aperture seismic arrays for phases generated locally by scattering from large heterogeneities, or topographic undulations. In essence, a hyperboloid-summation time migration is performed on array recordings of distant primary events to enhance local scattered phases. This technique can be applied to single events but should give more robust results when applied to a broadly distributed suite of primary sources. Prior to analyzing recorded data, synthetics are examined to assess the spatial resolution that can be achieved with the imaging algorithm. A preliminary analysis of real data is performed to provide initial images of the distribution of scatterers in the vicinity of the NORESS array in southern Norway. Several teleseismic events are analyzed separately to assess the feasibility of using a widely distributed suite of dissimilar primary sources in the imaging process. The analysis indicates that, due to the protracted nature of most teleseisms, deconvolution of the event records should be done before a final, spatial, image of the scatterers can be produced. The initial analysis of recorded data indicates that stable apparent secondary seismic sources are present in the vicinity of the NORESS array. These are tentatively interpreted as scatterers excited by the primary events.

## 2.1 Introduction

One of the important aspects of seismic monitoring is to understand the generation of seismic coda, particularly the near-station mechanisms. Two mechanisms that have been investigated include

seismic resonance (in low velocity strata) and scattering by inhomogeneities and topographic undulations (both at the free surface and at buried interfaces). The two processes appear to have different relative importance in the continental and oceanic crusts. Recent work (by Sereno and Orcutt, 1985a,b; Sereno and Orcutt, 1987; Mallick and Frazer, 1990) has produced evidence that in the oceanic crust, coda waves are likely dominated by resonance in the water and sedimentary horizons. Other studies (eg. Aki, 1969; Aki and Chouet, 1975) have argued that coda waves generated in the continental crust are most likely due to scattering by heterogeneities. Although studies quantifying the effects of scattering have mostly been statistical and have dealt with the influence of small-scale random scatterers, some deterministic studies (Key, 1967; Key, 1968; Gupta *et al.*, 1990a,b; Bannister *et al.*, 1990; Lay, 1987; Lynnes and Lay, 1989) have produced compelling evidence that large features are capable of producing significant amounts of scattered energy, principally in the form of large, identifiable seismic phases, which affect nuclear monitoring and discrimination: These prominent scattered phases may be confused with direct arrivals. Being able to identify these "secondary" sources is the first step toward being able to reduce this confusion.

Several attempts have been made to locate the sources of scattered phases both near the receiver (Key, 1967; Gupta *et al.*, 1990a,b; Bannister *et al.*, 1990) and near the source (Lay, 1987; Lynnes and Lay, 1989). The work to date suggests that the most significant sources of identifiable phases are topographic features at the free-surface.

## 2.2 The imaging technique

The problem of imaging sources of scattered energy using two-dimensional (2-D) array records bears a strong resemblance to the use of 1-D seismic reflection profiles to produce images of subsurface velocity contrasts. As a result, we have drawn on the experience of the reflection seismology community in the current analysis.

Recently, we (Hedlin *et al.*, 1990) have examined a suite of synthetic and recorded events (observed by the NORESS array in Norway) and developed a systematic technique to image nearby large scatterers. The underlying premise is that incident seismic waves impinging on a scatterer generate coda waves recorded by the array. From this point of view each scatterer may be treated as a secondary source which is excited with a delay estimated from elementary ray theory. We have applied a modified beamforming technique to array records to enhance signals radiated by such faint secondary sources.

## 2.2.a The adaptation of hyperbola summation migration to small aperture array data

To describe the technique, we adopt, for the time being, a simple model describing the origin of locally scattered waves - one in which a single omnidirectional point scatterer exists, is impulsively excited at a time t=0 and produces seismic motions that are recorded by an array of sensors located at the free surface (z=0; x=$x_j$, y=$y_j$) where j varies from 1 to N (the number of sensors in the array). Furthermore, we assume that the scattered energy propagates at a constant velocity, V, and there is no dispersion. Without loss of generality we place the scatterer at x=0,y=0 and find, using simple trigonometry, that the time $t_j$ at which the scattered wavefront should pass the jth sensor is given by:

$$t_j = \frac{\sqrt{x_j^2 + y_j^2 + z_s}}{V} \tag{2.1}$$

or, defining $t_0 = (\frac{z_s}{V})$, the vertical travel time from the scatterer to the free surface, equation 2.1 becomes:

$$\frac{t_j^2}{t_0^2} - \frac{x_j^2}{t_0^2 V^2} - \frac{y_j^2}{t_0^2 V^2} = 1 \tag{2.2}$$

Clearly, the surface in 3 dimensional space-time which describes the arrival times predicted for energy arriving from the scatterer is a hyperboloid of revolution (whose axis of symmetry is the time axis). From examination of equation 2.1 it is made clear that when the scatterer is located in the x-y plane the hyperboloid degrades to a circular cone with its apex located at the origin. If the space-time location of this sensor is outside the hyperboloid, the sensor cannot have been influenced by the scatterer. Conversely, if the sensor is located within the hyperboloid, the scattered wavefield will have already passed. Clearly, given this simple situation, to achieve the greatest enhancement of seismic motions caused by this source (at the expense of motions caused by secondary sources at other locations), and thus to achieve the best image of the source itself, one should sum the motions recorded by the sensors at times that will reposition each sensor in space-time onto the surface of the hyperboloid. This is a simple extension of the hyperbola summation migration method (Yilmaz, 1987) in seismic reflection. Since a delay-and-sum operation is involved, this method is akin to standard beamforming techniques and bears some resemblance to f-k analysis. This technique is distinguished, however, by its cognizance of not only the wavenumber but the onset time of a seismic arrival. As a result, the technique can be used to infer the likely geographic location of the secondary source. This method differs from previous attempts to locate large near-receiver scatterers since it is capable of accommodating simultaneously many primary events from different azimuths, to give a balanced, redundant, illumination of local scatterers while suppressing

the influence of near-source scatterers.

The *method* has been developed to accommodate secondary sources located at any point in the crust but, in view of the findings made by previous studies (Gupta *et al.*, 1990a,b; Bannister *et al.*, 1990), the following analysis is directed toward sources of $R_g$ energy located at the free surface

### 2.2.b Processing details

To image a region of the crust, we subdivide the area into small segments and considers them individually, in sequence. It is assumed that a secondary source exists within the sub-area of current interest. Since the location of the hypothetical scatterer is known, the adoption of a slowness of propagation of the scattered waves, $p_s$, allows the space-time hyperboloid to be defined. For each crustal sub-area being scanned 'he ecordings of the teleseismic event are summed after shifting them in time as required by the hyperboloid. In practice, since it is not known when, in absolute time, excitation occurs, the time axis is translated so that the onset time of the primary energy at the array occurs at t=0. Using elementary ray theory it is possible to estimate what time delay, $\tau$, should exist between the arrival of the primary energy and the scattered phases originating at the hypothetical scatterer after excitation by the primary energy. As is illustrated in Figure 2.1, considering a single event-scatterer pair, the time offset, $\tau$, between the arrivals of energy propagating directly from the source (at vector slowness $p_i$) and via the scatterer (vector slowness $p_s$) at a vector distance $R_{as}$ from the array is given by:

$$\tau = R_{as} \bullet (p_i - p_s) \tag{2.3}$$

It is possible to estimate $p_s$ by considering a suite of broadly distributed events and computing a number of preliminary images while slowly varying this parameter and selecting the value that brings the image into the sharpest focus. The slowness of the incident energy, $p_i$, is well constrained by fitting a least-squares best fit plane (in x-y-t space) to the first breaks on the array records. By systematically scanning the crustal volume about the array, we can generate an image which is interpreted as a map of local scatterers. To date, we have considered scattering interactions excited by P waves, using both synthetic seismograms and recorded data.

In practice, there are a number of complicating factors that must be taken into account prior to constructing images of faint, local sources using synthetics or recorded data.

1) If the scattered field consists of surface waves, propagating at the surface of a crust whose velocity increases with depth, no single velocity, V, will allow a comprehensive description of
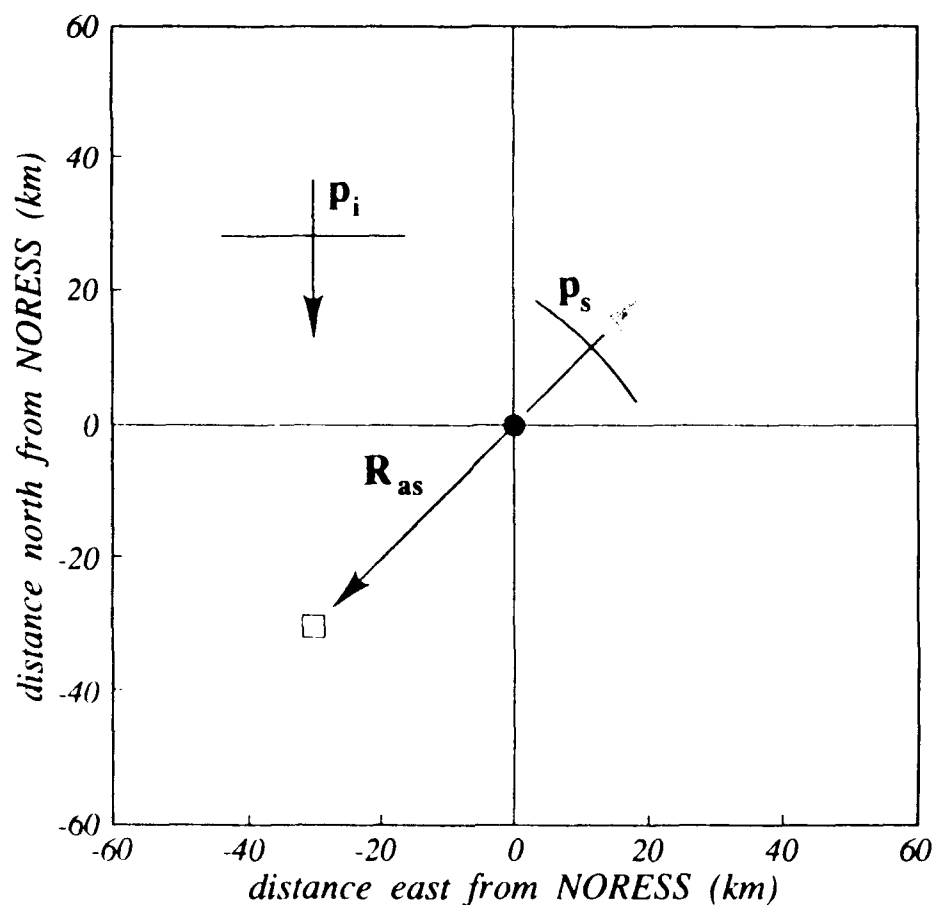
Figure 2.1 The vectors appearing in equation 2.1 are illustrated in this figure. The incident wavefront arrives from the north at a vector slowness of $p_i$. A scattered wavefield originates within the small box (3 km on a side) and propagates outward to the NORESS array (dark circle at the center of the figure) at vector slowness $p_s$. The vector from the array to a sample block is $R_{as}$. Both the array and the sample block are shown to scale.

the scattered wavefield - the energy will become dispersed. As a result it becomes necessary to integrate over a span of time centered on the space-time hyerboloid which is defined by a velocity representative of the average speed of propagation of the surface wave energy. We have used integration time windows of up to 5 seconds in duration.

2) Based on the results of synthetic tests we have not attempted to use the full coherent, or phased, recordings. Because we are are dealing with dispersive energy, we have concluded that the trade-off between image resolution and stability can best be mitigated by migrating coherent records but converting the results to envelopes prior to integration in a method akin to incoherent beamforming (Ringdal et al., 1975).

3) When considering the recorded data, it is immediately apparent that local scattered phases,

excited by teleseismic energy, cannot be examined in the absence of this (primary) energy. It is necessary to mask the more energetic primary source by suppressing the energy that has propagated directly from it. The method we have adopted to accomplish this, introduced by Gupta *et al.* (1990a), is known as beam correction and simply involves the coherent subtraction of the primary source beam from all the individual channels to yield residual seismograms.

4) The recorded signals are immersed in seismic noise, much of which is microseismic energy originating in the North Sea (Fyen, 1986), and thus exists in a relatively low frequency band ($\frac{1}{10}$ to $\frac{1}{3}$ Hz). Fortunately, the surface wave energy of interest exists, mainly, in the band from $\frac{1}{2}$ to 3.0 Hz, and thus the signal to noise ratio (SNR) can be significantly improved by narrow band pass filtering of the array records.

5) Since we are considering surface wave propagation, a gain proportional to $\sqrt{|R_{as}|}$ should be applied to compensate for amplitude loss due to cylindrical geometrical spreading.

6) Finally, further complication, that exists only in the recorded data, is caused by the non-impulsive nature of most teleseisms - they consist of a protracted sequence of arrivals. Discussion of the impact of this complication is deferred to sections 2.3 and 2.4.


## 2.3 Analysis of synthetic seismograms - imaging resolution

The resolution of the imaging technique can be gauged from experiments with synthetics. Using wavenumber integration (Apsel and Luco, 1983; Luco and Apsel, 1983) we consider a localized omnidirectional scatterer (delta function in space) illuminated by an impulsive incident wave (delta function in time), and compute synthetic vertical seismograms individually for each of the sensors in the array. Since no energy from the primary source is added to the local synthetic phases, this yields a perfectly beam-corrected image (Figure 2.2). This, and all subsequent images, have been computed by subdividing the area shown into 1681 blocks 3 km on a side. In the preliminary analysis of synthetic seismograms and recorded data we have chosen a surface wave slowness of .304 s/km (the slowness of the dominant phase in the synthetic $R_q$ packet) and have bandpass filtered the records between 1 and 3 Hz. All synthetic images have been adjusted for the amplitude loss due to geometrical spreading.

As illustrated in Figure 2.2 the radial resolution of the point source is limited. This is due to some extent to the dispersion of the surface wave packet (displayed in the lower half of the figure) but to a greater extent by the time-averaging (in this case 5 seconds). Clearly, an inverse relationship exists between the degree of time-averaging that is employed and the radial resolution. The azimuthal resolution
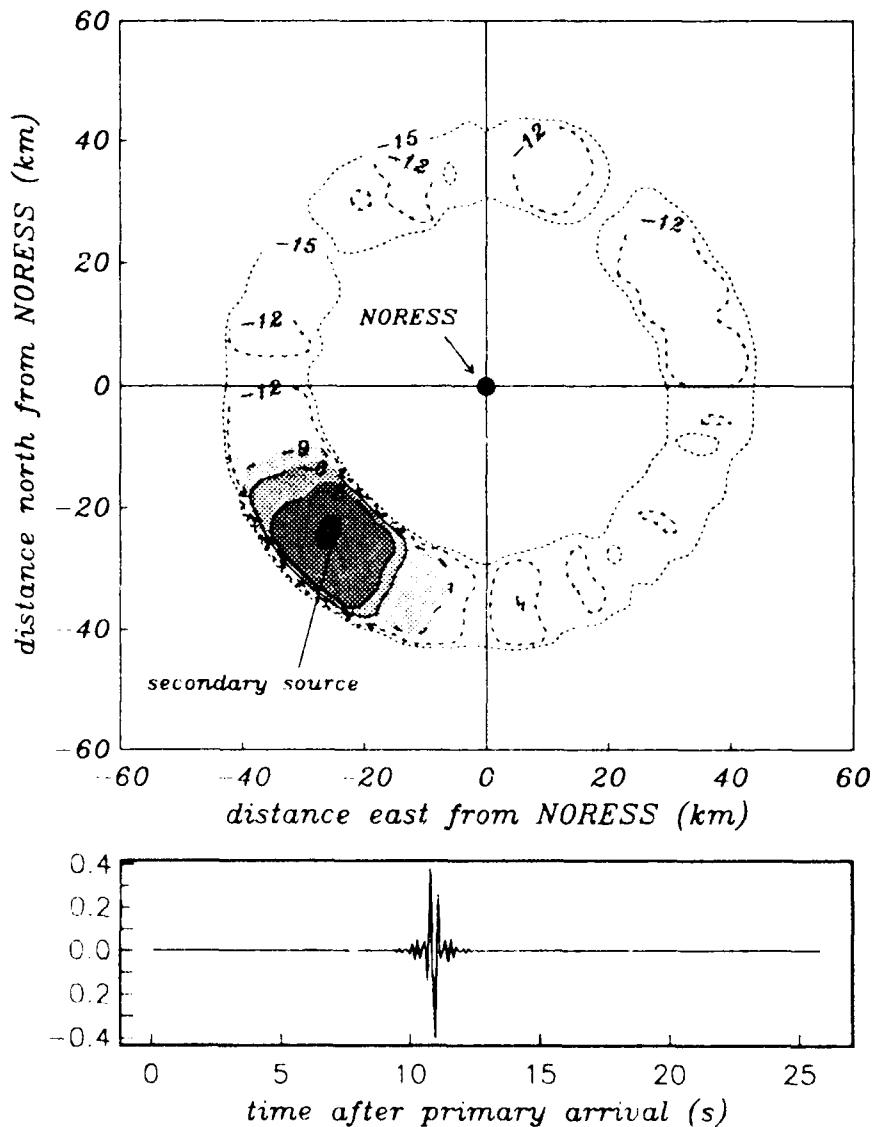
**Figure 2.2** Image of a synthetic point source located 35 km from the array at a back azimuth of 225°. Wavenumber Integration was used to generate synthetic seismograms individually for each of the 25 vertical component sensors in the NORESS array (illustrated is the synthetic computed for the center station). In this, and all subsequent images, contour values indicate amplitudes in dB relative to the largest value in the image and cylindrical propagation of scattered wavefronts was assumed.

of the synthetic source is very poor primarily because the coherence of the surface waves, computed with only a small degree of numerical noise, is very high and because we are employing envelopes of the beams.

Energy is aliased away from the actual location of the scatterer to locations which share the same delay time. By manipulation of equation 2.1, it can be shown that scatterers which share a common

delay time $\tau$ lie on a curve described by:

$$|R_{a,s}| = \frac{\tau}{|p_s| - |p_i|cos(\theta)} \tag{2.4}$$

When $p_s$ is greater than $p_i$ (eg. P to $R_y$ scattering) this describes an ellipse with one focus at the center of the array, major axis pointing to the primary source and eccentricity proportional to $p_s$. In this synthetic calculation the primary source was located directly beneath the array ($p_i = 0$) and thus the curves of constant $\tau$ have degenerated into circles centered on the array.

To test the dependence of the azimuthal and radial resolution on the range of the source from the array an additional suite of synthetics has been computed in which three point sources were placed 12.5, 25.0 and 37.5 km from the array at a back-azimuth of 225°. The image obtained using these synthetics is displayed in Figure 2 3. Not surprisingly, the azimuthal resolution is reduced as distance from the array to the source increases. There is no discernable reduction of radial resolution with increasing range due to dispersion of the surface wave packet since the radial resolution is degraded to a greater degree by the time-averaging (in this case 5 seconds). The azimuthal resolution depends strongly on the aperture of the seismic array. In Figure 2.4 is displayed the image of the point source used to create Figure 2.2, however in this case the array used, referred to as MORESS, is simply the NORESS array with all dimensions doubled by affine transformation. By comparison of Figures 2.2 and 2.4 it is clear that the azimuthal resolution has improved roughly by a factor of 2. The greater spacing between the sensors in this new array, however, means that the spatial aliasing is more severe (note the increased size of the side lobes relative to those in Figure 2.2).

The preceding images were computed using synthetics corrupted only by a small degree of numerical noise. In Figure 2.5 we test the ability of the imaging algorithm to locate successfully a secondary source when the records contain a significant amount of noise, that, for some reason, cannot be suppressed by filtering. To generate this image we have added Gaussian noise, uncorrelated in space and time, to the synthetics used to generate Figure 2.2. The image has suffered a significant amount of corruption but, despite high noise levels, evident in the time series displayed in the lower half of this figure, the secondary source is still inferred to exist at the correct location.

The imaging algorithm assumes that all excitation of a scatterer located at $R_{a,s}$ occurs at $\tau = R_{a,s} \cdot p_i$ (the scatterer is illuminated by a single arrival). This condition is met by the synthetics, and as a result it is possible to infer the geographic location of the synthetic source, not just the time of excitation and angle of approach. If this is not the case, and the incoming wavetrain consists of a
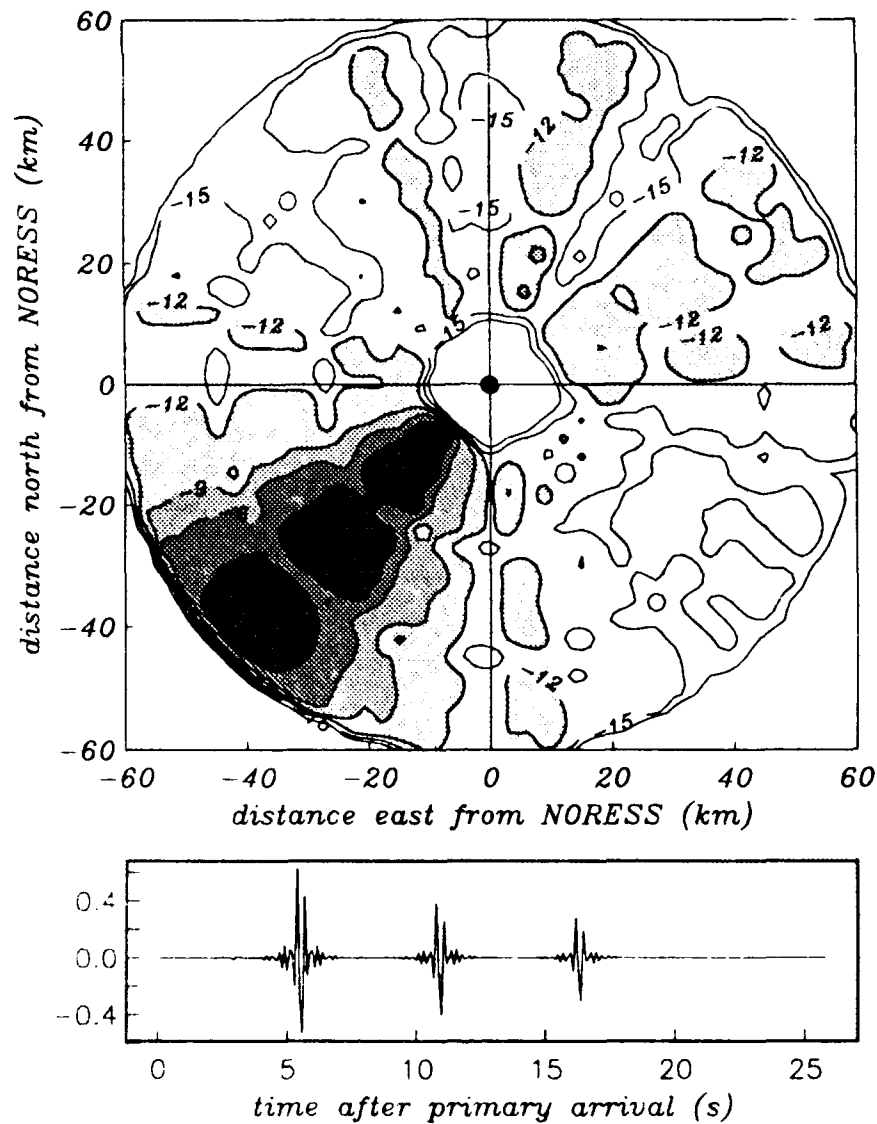
**Figure 2.3** Image of three synthetic point sources located 13, 35 and 53 km from the array at a back azimuth of 225°. Illustrated is the wavenumber integration synthetic computed for the center station in the array.

protracted sequence of arrivals, then a single scatterer will be illuminated, and likely emit energy, for a longer time.

In theory, this should result in a "tail" of energy extending outward from the actual location of the scatterer along a radial line (see Chapter 3). In such cases it is more appropriate to plot the image as a function of time, not space.
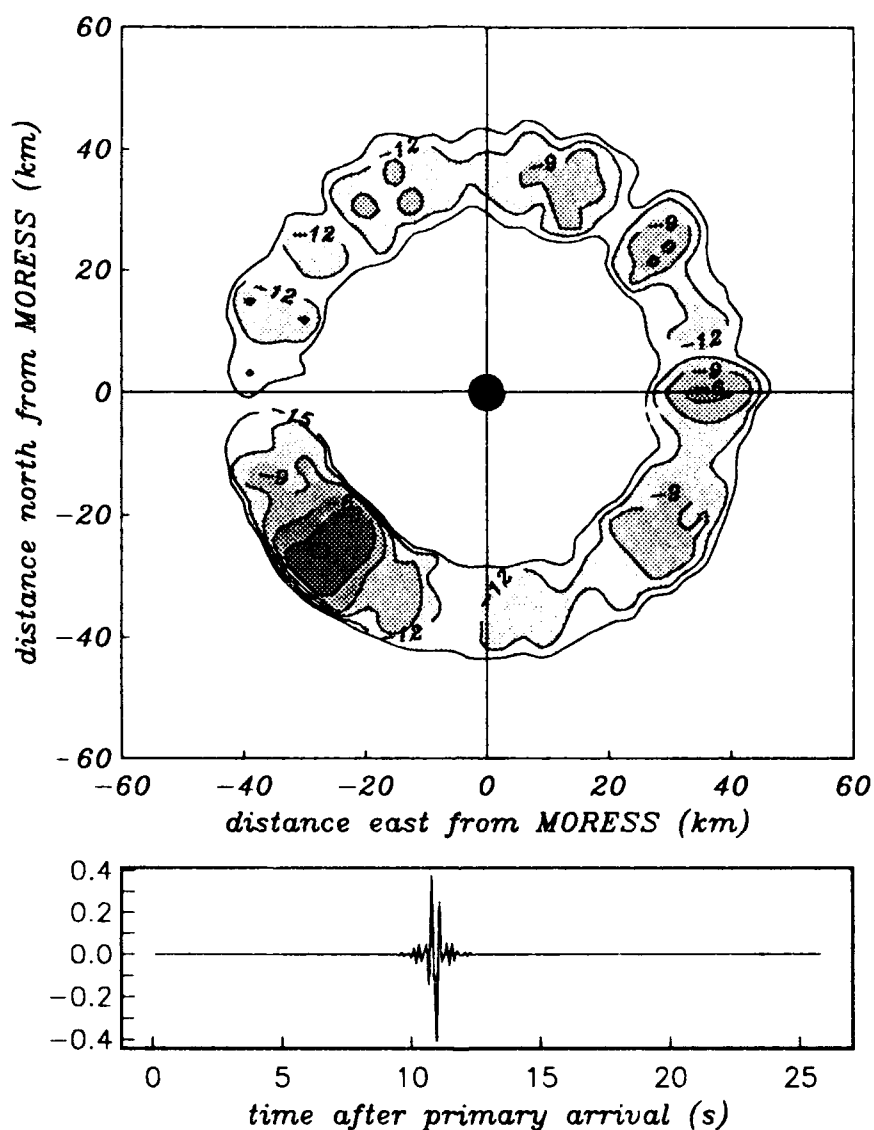
Figure 2.4 Image of a synthetic point source located 35 km from the array at a back azimuth of 225°. Illustrated is the wavenumber integration synthetic computed for the center station in the MORESS array (an array created by dilating the NORESS array by a factor of 2).

## 2.4 Preliminary analysis of recorded data

*2.4.a Analysis of single events*

In this section we apply the technique to recordings of 5 nuclear explosions and 1 earthquake made by the NORESS arra, ... southern Norway (see Table 2.1). To test the resolving power of events
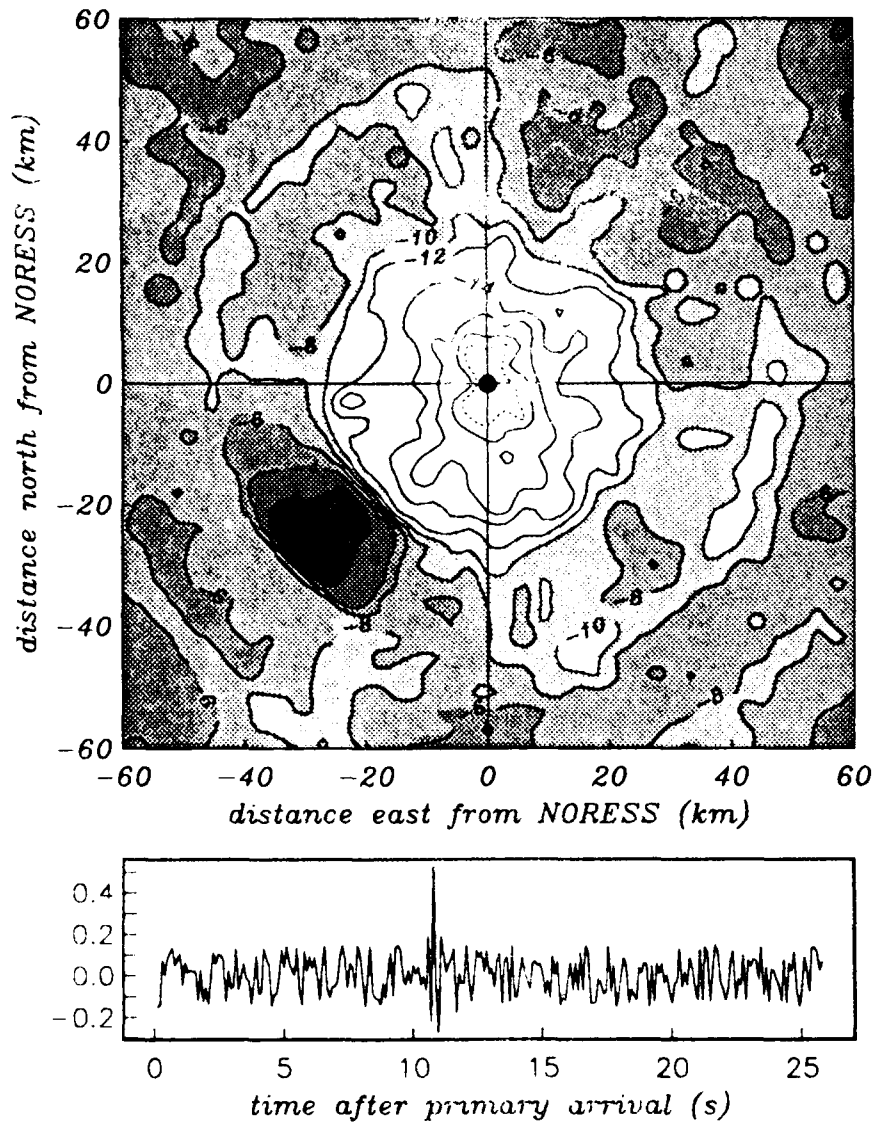
Figure 2.5 Image of a synthetic point source located 35 km from the array at a back azimuth of 225° computed after adding a significant amount of Gaussian white noise to each channel. Illustrated is the wavenumber integration synthetic computed for the center station in the array.

coming from a single azimuth (and thus to gauge the improvement we can expect by using a widely distributed suite of events) an image has been computed using a single Semipalatinsk nuclear explosion (84351).

Although all Semipalatinsk explosions produce images that are remarkably similar, we chose this event because it has been previously considered by Gupta et al., (1990a,b) who also applied beam-correction, and f-k analysis in their search for large scatterers. This gives us an opportunity to compare
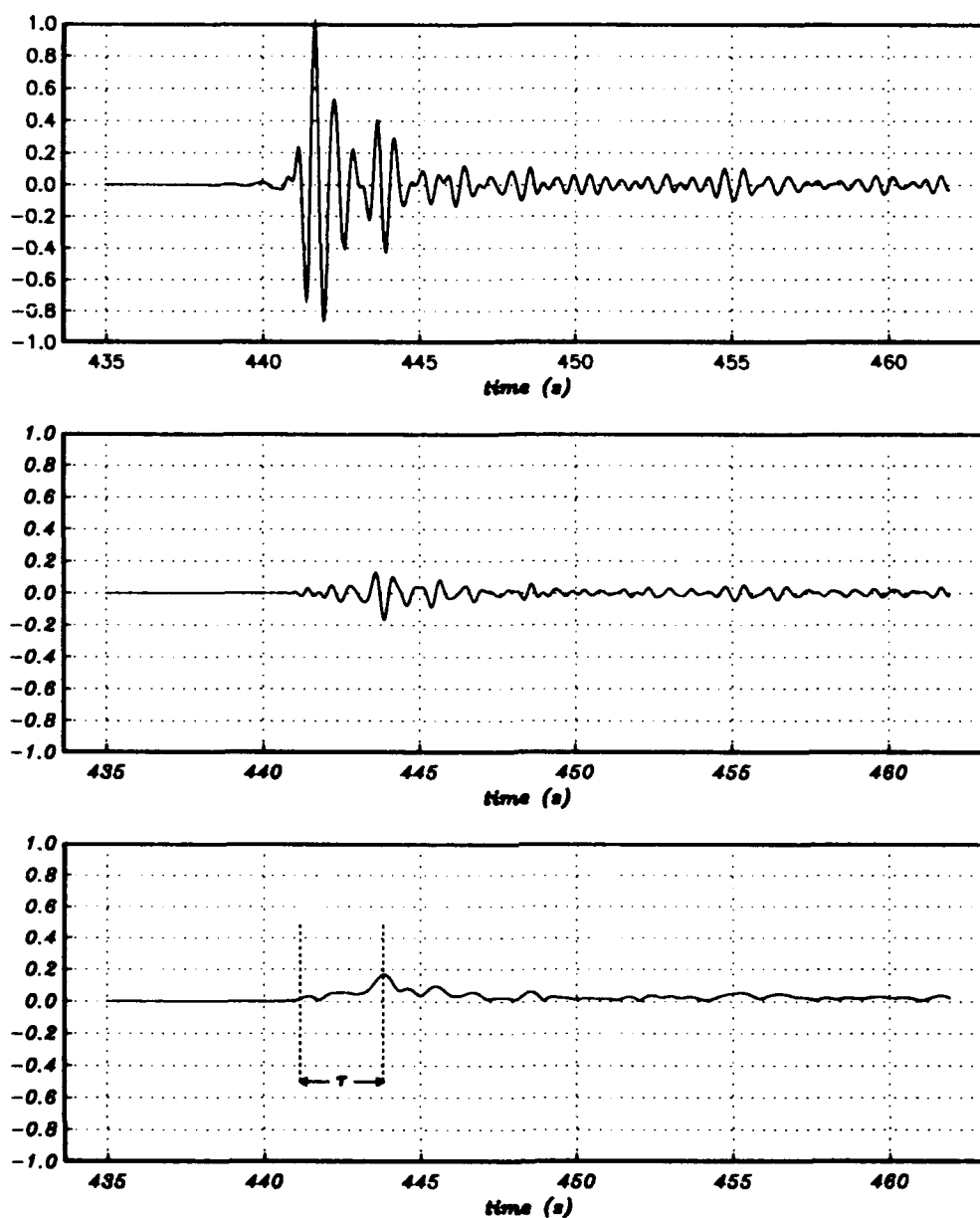
Figure 2.6 This figure is included to illustrate the effect of beam correction. Pictured in the upper box is the NORESS center element (a0) recording of a Semipalatinsk nuclear explosion (84351; see Table 2.1). The middle box displays the residual a0 channel after the beam to the primary source has been coherently subtracted. The residual channels have been beamformed for a back azimuth of 80° and a phase velocity of 3.29 kms$^{-1}$. The resultant beam has been converted to an envelope. Energy is concentrated at a delay time $\tau$ of roughly 3 s.

both techniques. Because of the energetic nature of the Semipalatinsk teleseism, it has been necessary to apply beam correction to the recorded data. To illustrate the need for, and the effect of, beam correction, we have included Figure 2.6. Illustrated in the upper part of this figure is a single channel recording
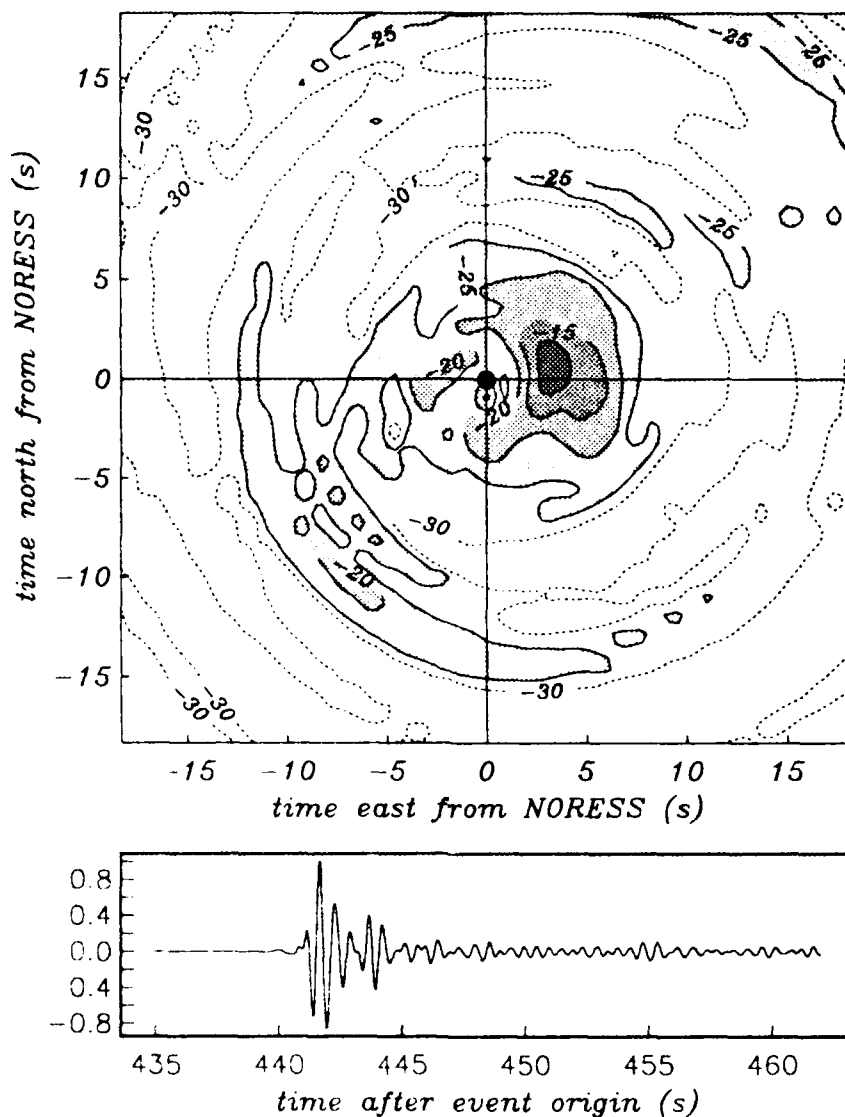
**Figure 2.7** Image of the scattering field in the vicinity of the NORESS array obtained using a single Semipalatinsk nuclear explosion (84351). The image was generated by employing 1 second of time averaging. The test site is located at a back azimuth of 75°. Due to the protracted form of the incoming wavefield (estimated by the beam pictured in the lower half of the figure), the image has been plotted as a function time. In practice we found that applying a gain to correct for geometrical spreading of the recorded scattered waves resulted in an unacceptable amount of noise amplification at extreme ranges so we did not do it.

(a0) of the Semipalatinsk nuclear explosion (84351). In the middle third of the figure is the residual record that remains after correcting (coherently subtracting) primary source beam source from channel a0. To obtain the lower third of the figure all array records have been beam-corrected, beamformed for a back-azimuth of 80° (an azimuth known to contain an apparent secondary source of energy). The

resultant coherent beam has been converted to an envelope. There is clearly a concentration of energy centered at $\tau$ s behind the compressional onset.

| Table 2.1. Event Locations | | | |
|---|---|---|---|
| Event | Latitude | Longitude | Origin Time |
| | (°N) | (°E) | year/day/h:m:s |
| 84351 | 49.88 | 78.82 | 84/351/03:55:02.8 |
| 85134 | -10.72 | 41.26 | 85/134/13:25:01.2 |
| 86318 | 37.10 | -116.05 | 86/318/16:00:00.0 |
| 87225 | 37.06 | -116.05 | 87/225/14:00:00.1 |
| 87267 | 37.23 | -116.38 | 87/267/15:00:00.0 |
| 87287 | 37.09 | -116.05 | 87/287/14:00:00.1 |

The steps illustrated in Figure 2.6 are systematically followed for all 1681 sub-areas to construct an image using recorded data. The image in Figure 2.6, and the following ones computed using recorded data, have been plotted as functions of time because of the protracted nature of the incoming primary wavetrains. The first image, obtained from the Semipalatinsk event (84351), is displayed in Figure 2.7 and has been computed using 1 second of time averaging. It contains significant amounts of energy smeared along ellipses of constant $\tau$. Not surprisingly, the ability of a single primary event to resolve structure in the azimuthal direction is poor. As in synthetic tests, the smearing is due to the high coherence of the low frequency scattered phases across the array. We can decrease the smearing by increasing time-averaging so that several cycles of less coherent scattered energy are included in the window. By increasing the time span to 5 seconds of coda centered on the predicted onset we obtain the result displayed in Figure 2.8. The smearing is still present, but has been significantly reduced, and two apparent energy sources are clearly resolved although with somewhat lesser radial resolution. The feature in Figure 2.8, close to the array in the first quadrant is due to the energy displayed in the lower third of Figure 2.6 at $\tau$ s behind the primary onset. Previous studies (Gupta et al., 1990a; Bannister et al., 1990) which have used the NORESS array to locate local sources of scattered energy have also identified an apparent local secondary source to the south-west of the array. These studies have concluded that this energy is most likely due to scattering interactions occurring at the Skreikampen/Lake Mjosa topographic relief (a north-west to south-east trending lake with an adjacent mountain that has roughly 1000 m of total relief) located roughly 35 km from the array. In addition, the latter study noticed energy coming from the north-east of the array and attributed this to the Bronkeberget topographic relief at a range of roughly 10 km.

To expedite the present analysis, we assume that two point sources are present and, as is suggested by Figure 2.8 and the two previous studies (Gupta *et al.*, 1990a; Bannister *et al.*, 1990), are located roughly 35 km to the southwest of the array, and 10 km distant at a back azimuth of 80°. Since we have fixed the secondary source locations, it is possible to use equation 2.4 to predict where energy originating at these locations should be aliased to in this image. We have done so and have overlain the ellipses associated with these two apparent sources on the image in Figure 2.8. The strong coincidence between these ellipses and locally high power levels suggests that much of the energy in this figure likely originates from the two sources.

In Figure 2.9 we take this analysis one step further by placing two point sources at these locations, illuminating them using arrival times consistent with a teleseism arriving from Semipalatinsk, and computing synthetics for each element in the array.

Although this has been a crude forward modelling exercise (the synthetic the sources are infinitely small, perfectly omnidirectional and impulsively excited) this image bears a striking resemblance to the real image in Figure 2.8 despite the use of a gain to compensate for geometrical spreading only in the synthetic image. In the synthetic image, since only two point sources exist, and their locations are known, we can discriminate between the true sources, and false sources that are due to spatial aliasing. For example, considering the inner ellipse, we know that the true source exists to the east or the array and that all sources inferred to exist close to the array to the south, west and north are false, and are only due to energy aliased away from the true location. The two small sources inferred to exist in the Norwegian crust to the south and west of the array (at a time range of roughly 3 s) by the image in Figure 2.8 are almost certainly only due to aliasing from a single source to the east of the array.

### 2.4.b Image instability - should the fold of coverage be increased?

Clearly it would be desirable to produce more robust images of the local scatterers by simultaneously processing a broadly distributed suite of primary events. In doing so, we could, in effect, image the crust through a "synthetic aperture array". Such an event suite would provide a more "balanced" illumination of the population of scatterers that could be provided by a single event since we could scan the crustal volume for stable apparent sources. As discussed earlier, when considering event 84351, it was noticed that the azimuthal resolution was improved somewhat at the expense of reducing radial resolution - or in other words - that a trade-off exists between azimuthal and radial resolution that cannot be avoided when using single primary events. It is possible to increase azimuthal resolution using a
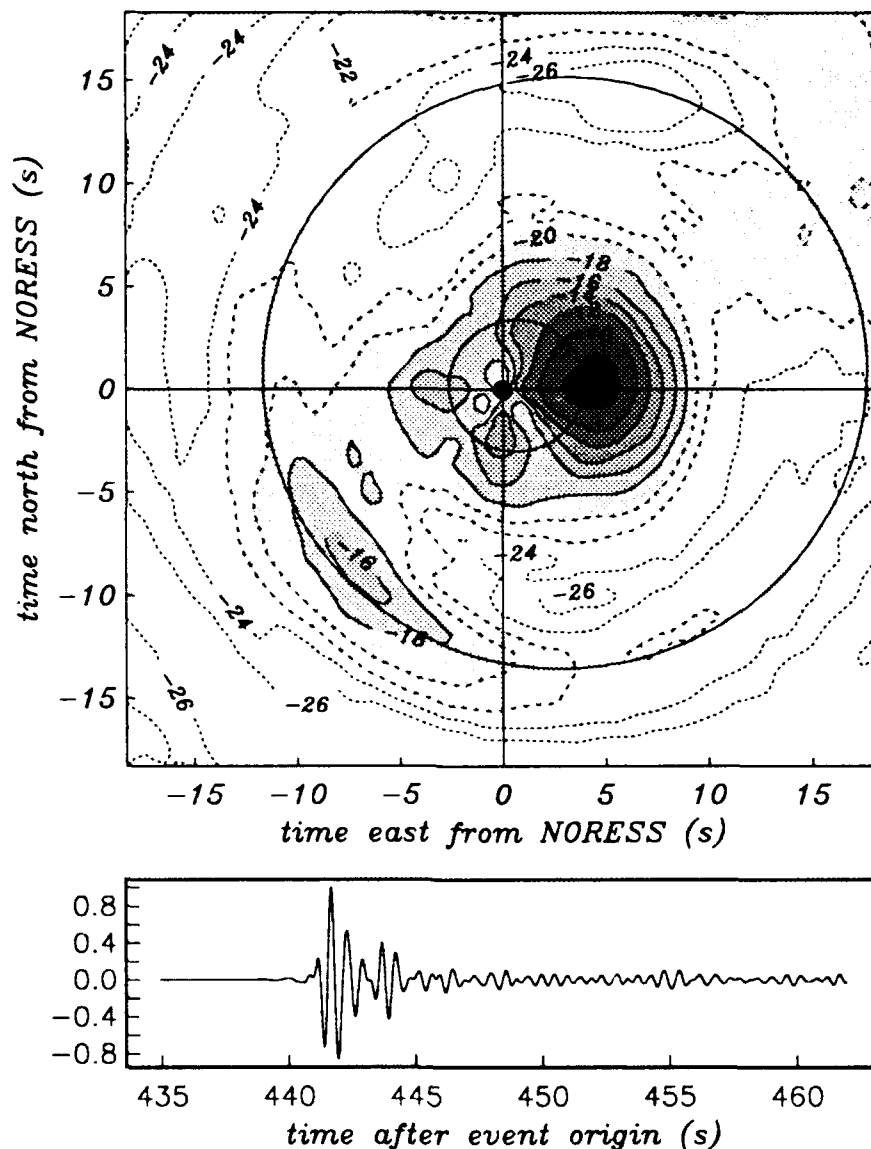
**Figure 2.8** Image of the scattering field in the vicinity of the NORESS array obtained using a single Semipalatinsk nuclear explosion (84351). The image was generated by employing 5 seconds of time averaging. The beam computed for the test site is pictured in the lower half of the figure. Overlain on the image are two ellipses representing the curves of constant delay time $\tau$ appropriate for scatterers illuminated by this event. The secondary sources are located 38 km from NORESS at a back azimuth of 225° and 13 km at a back azimuth of 80° .

broadly distributed suite of primary events without degrading radial resolution. It is certain that stacking numerous events will help suppress incoherent noise in the event records, and thus, for this reason, image stability should increase. The question we want to address next is whether it is feasible to attempt the stacking of dissimilar primary events to find a more robust image of the local scatterers. In an attempt to answer this question, we have computed an image of the scatterers by using teleseisms from 3 nuclear
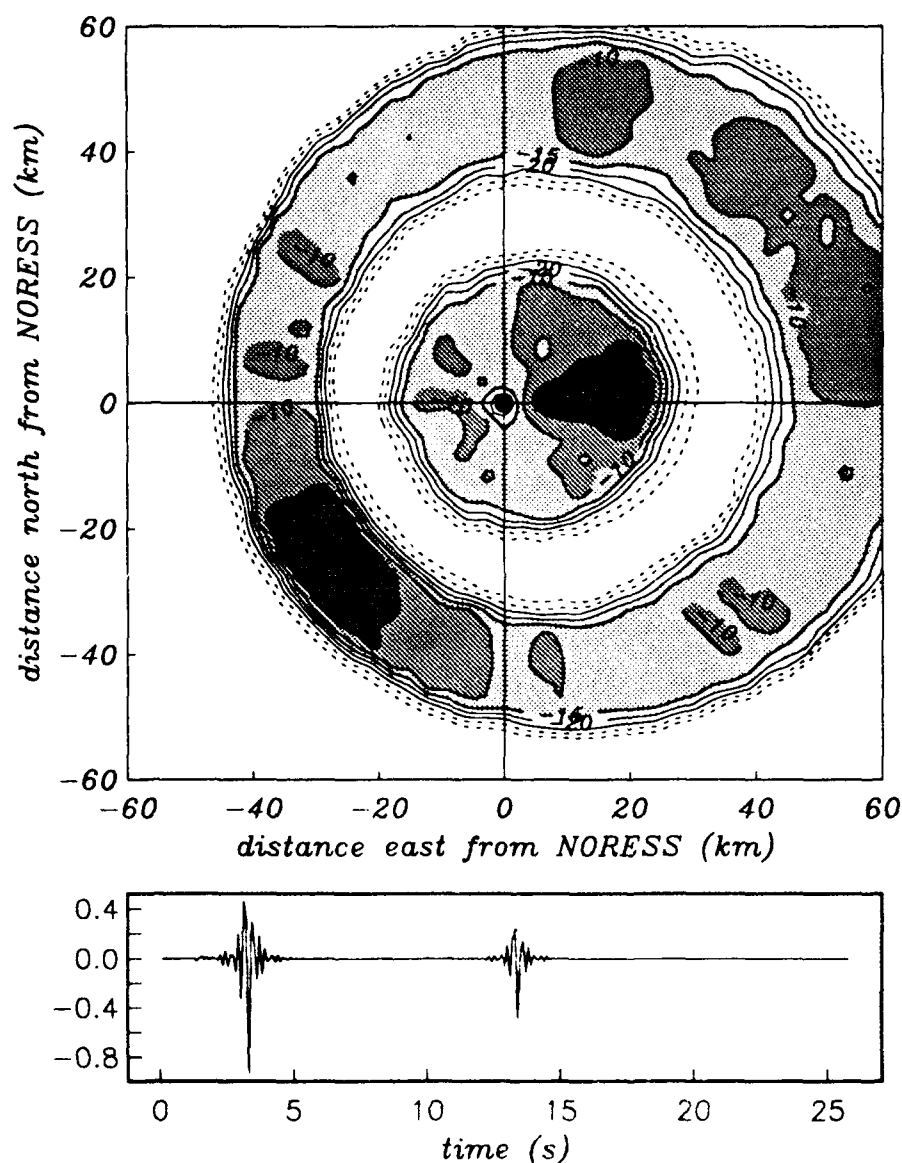
**Figure 2.9** Image of two synthetic point sources (located 35 km from the array at a back azimuth of 225° and 13 km from the array at a back azimuth of 80°). The sources were illuminated by an impulsive synthetic primary event located near Semipalatinsk. Illustrated is the wavenumber integration synthetic computed for the center station in the array.

explosions detonated at the Nevada Test Site (NTS). The result is displayed in Figure 2.10 with the smearing ellipses computed for the two local sources considered in Figure 2.9 overlain. The ellipses have changed since $p_1$ has changed (the back azimuth to the NTS is roughly 318°). A secondary source is still inferred to exist to the east of the array (at a time offset of roughly 4 s), but beyond that coincidence, this image is profoundly different from that in Figure 2.8. A strong source is inferred to exist to the northwest of the array. Several coherent sources are suggested to exist to the south of the array.
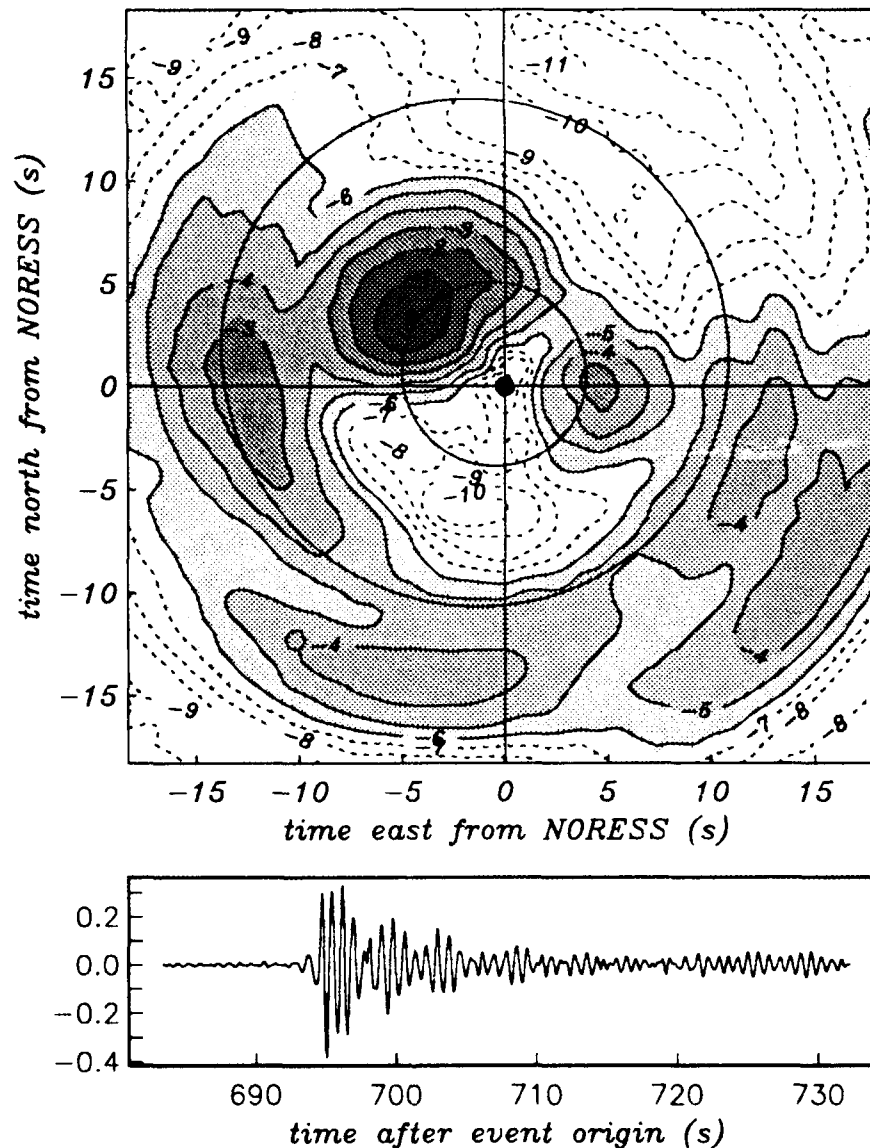
**Figure 2.10** Image of the scattering field in the vicinity of the NORESS array obtained using four nuclear explosions detonated at the Nevada Test Site (NTS) (86318, 87225, 87267 and 87287). The image was generated by employing 5 seconds of time averaging. The beam computed for the test site, using recordings of the second event, is pictured in the lower half of the figure. Overlain on the image are ellipses representing the curves of constant delay time $\tau$ appropriate for scatterers illuminated by these events. The secondary sources are located 38 km from NORESS at a back azimuth of 225° and 13 km at a back azimuth of 80° .

These two images suggest that there is the possibility that the intrinsic appearance of the crust depends on the direction from which it is illuminated. If we accept the hypothesis that topographic features are responsible for the bulk of the scattered energy then an examination of this surface quickly reveals that common topographic structure has geographic extent and is clearly not cylindrically symmetric - there is
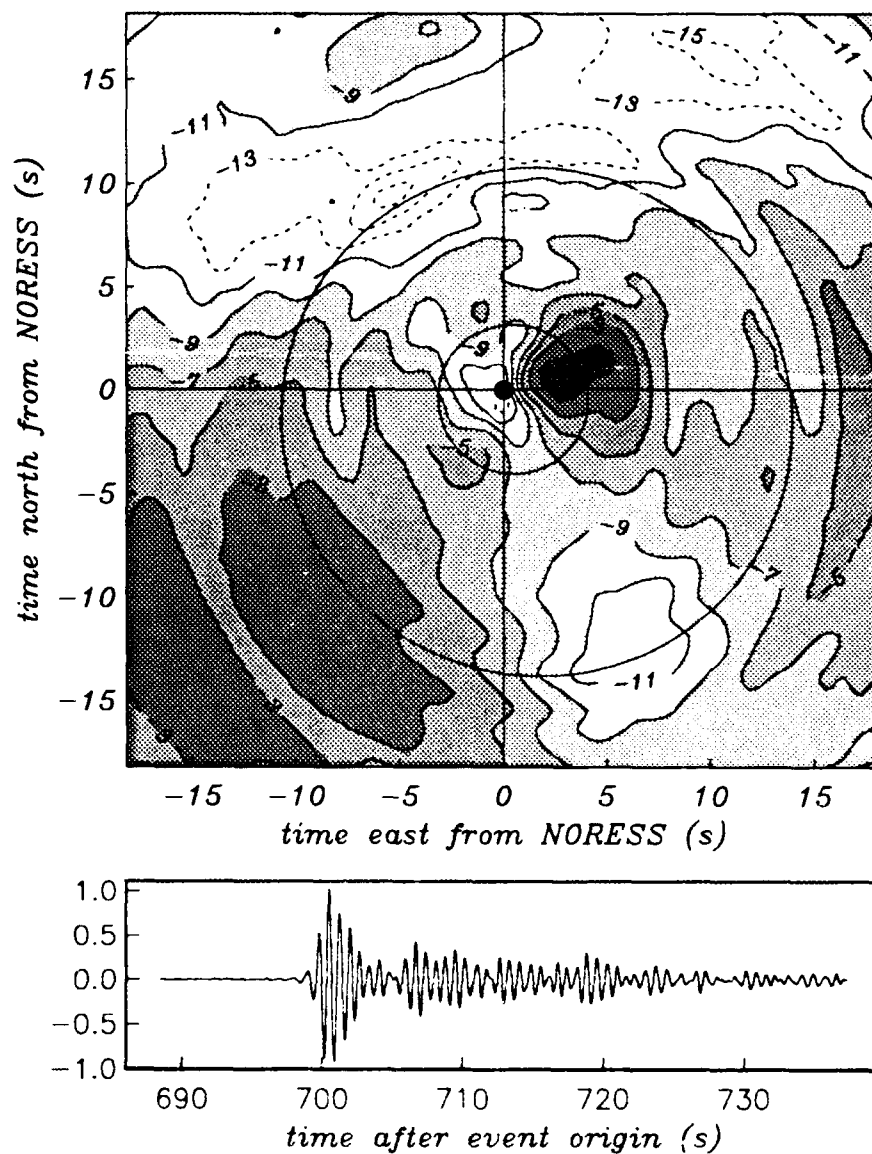
**Figure 2.11** Image of the scattering field in the vicinity of the NORESS array obtained using recordings of a single earthquake (85134; 10.7° S, 41.3° E). The image was generated by employing 5 seconds of time averaging. The beam computed for the earthquake is pictured in the lower half of the figure. Overlain on the image are ellipses representing the curves of constant delay time $\tau$ appropriate for scatterers illuminated by this event. The secondary sources are located 38 km from NORESS at a back azimuth of 225° and 13 km at a back azimuth of 80°.

a clear northwest-southeast fabric in which typical features are 10's of km long. In view of the geographic extent, and shape, of typical topographic features it is not be surprising that there appears to be some dependence of the appearance of the crust on the direction from which it is illuminated. If this was the only possible explanation of the dissimilar nature of the images then perhaps a strong argument could be made against stacking.

Fortunately, other explanations exist which can explain the disparate nature of these images and strongly support the simultaneous use of many primary events to attempt a more robust imaging analysis. The image quality of Figure 2.10 is clearly degraded since the signal to noise ratio (SNR) is much lower in the NTS seismograms than it is in the Semipalatinsk events. We expect that noise in the data will map directly into image noise, or instability. Some, or all, of the apparent sources in this image (or any image produced using a single event) could be due to coherent bundles of noise. Furthermore, a distinct possibility exists that the energy located in the fourth quadrant of Figure 2.10 (at roughly the back azimuth of the primary event) does not have a local source but, in fact, is due to incomplete beam-correction. This argument could be used to shed doubt on the reality of the secondary source inferred to exist to the east of the array by the Semipalatinsk event (Figure 2.8) since Semipalatinsk is located at a back-azimuth of 75° from the array.

Obviously, neither of the two images considered thus far can confidently be touted as representative of the true distribution of scatterers. Unless the intrinsic appearance of the crust is wildly dependent on the direction of illumination it seems clear that image quality can be improved if a large number of events are allowed to "vote" on what a representative image of local scatterers should be. It also seems logical that greater attention should be paid to the events recorded with higher SNR. If the feature in the fourth quadrant in Figure 2.10 is due to incomplete beam correction, and even if this problem is shared by many events, then stacking of a broadly distributed suite should suppress this effect, since the primary source energy should lie in a pie slice originating at the array and pointing toward each primary source. Furthermore, such stacking should serve to suppress the influence of near source scatterers - and incoherent noise.

A very similar problem has plagued the reflection seismic community. As in our work, they image subsurface structure using recordings of phases produced by the interaction of man-made seismic energy and sub-surface reflectors. It is well known (Yilmaz, 1987; Claerbout, 1985) that attempting such imaging using data that has sampled each point on a reflector of interest only once, "single fold coverage", generally yields poor results. Given the size of typical primary sources, the SNR isn't high enough to allow good resolution of the subsurface "secondary" sources. To improve the results, seismic data is generally collected such that redundant excitation of each subsurface point of interest is achieved - or to use the parlance of the reflection seismology community - the fold of coverage is increased. The redundant recordings are stacked to interfere coherently such energy. In the current problem, we can increase the fold of coverage, or we can in effect cause each active scatterer to be redundantly excited, by using more than one primary event.

*2.4.c An illustration of why temporal deconvolution is necessary*

As mentioned in section 2.2, further complication is provided by the fact that the excitation function is clearly not impulsive but consists of a protracted sequence of arrivals (a wavetrain). In Figure 2.12 is illustrated an image computed using a single teleseismic earthquake as a primary source (event 85134 located at a back azimuth of $133°$) and assuming a $p_s$ of .304 $skm^{-1}$. An energy low in the second quadrant (at the back azimuth to the primary event) suggests that the beam correction has been effective. The two sources discussed earlier are still prominent but an additional apparent source is inferred to exist in the third quadrant. When generating images using temporally protracted teleseisms, a fundamental ambiguity exists when trying to locate sources of scattered energy. Is one apparent source inferred to exist at a greater distance from the array than another because it is located farther from the array or because it is due to excitation by a tardy primary arrival? It seems likely that this distant source is simply due to a late arrival from the earthquake exciting a scatterer located relatively close to the array since other events see no source at this location. Prior to generating spatial images of the local scattering field using recorded teleseismic events as primary sources it is clear that an attempt should be made to suppress the influence of late primary arrivals. In Chapter 3 a simple convolutional model is developed to describe the interaction between protracted teleseismic wavetrains and the impulse response of the local scatterers. A remedy, in further pre-processing involving deconvolution of an estimate of the incoming wavetrain from the individual records, is developed.

## 2.5 Conclusion

In this chapter, a technique to image for local sources of scattered energy using small aperture array recordings has been developed. In essence, a hyperboloid summation migration is used to resolve the faint secondary sources of $R_g$ energy. This technique has been applied to array recordings of individual real and synthetic events. The synthetics have shown that the azimuthal spatial resolution provided by the technique, when applied to a small-aperture array, is inversely proportional to the distance to the secondary source and directly proportional to the aperture of the array. In theory, the radial resolution should be inversely proportional to the range to the secondary source (due to dispersion of the surface wave packet). However this effect is, in practice, lessened due to the effect of time-averaging. Preliminary analysis of several events recorded by the NORESS array in southern Norway indicates that stable secondary sources

likely exist in the vicinity of the array (to the southwest and northeast). These results are consistent with those of Gupta *et al.*(1990a,b) and Bannister *et al.*(1990). It appears, however, that the production of robust images cannot likely be achieved using single primary events. The feeble secondary sources cannot be well imaged without redundant excitation. It is necessary to "increase the fold" by stacking the results of a large suite of broadly distributed primary events. Because of the protracted nature of most teleseisms it is not clear what primary phases are responsible for exciting locally scattered energy. As a result, only temporal images have been produced. To refine the algorithm further, to facilitate the production of spatial images, will require deconvolution of the incident wavetrain (Chapter 3). This will allow us to test more stringently the stability of our images.

## 2.6 Acknowledgments

# References

Aki, K., Analysis of the seismic coda of local earthquakes as scattered waves. *J. Geophys. Res.*, **74**, 615-631, 1969.

Aki, K. and Chouet, B., Origin of coda waves: source, attenuation, and scattering effects. *J. Geophys. Res.*, **80**, 3322-3342, 1975.

Apsel, R.J. and Luco, J.E., On the Green's functions for a layered half-space, part II. *Bull. Seismol. Soc. Am.*, **73**, 931-951, 1983.

Bannister, S.C., Husebye, E.S. and Ruud, B.O., Teleseismic P coda analyzed by three-component and array techniques: Deterministic location of topographic P-to-$R_g$ scattering near the NORESS array. *Bull. Seismol. Soc. Am.*, **80B**, 1969-1986, 1990.

Claerbout, J.F., *Imaging the Earth's interior*. Blackwell Scientific Publications, 1985.

Fyen, J., NORSAR semiannual technical summary - 2-85/86. *48-59*. 1986.

Gupta, I.N., Lynnes, C.S., McElfresh, T.W. and Wagner, R.A., F-K analysis of NORESS array and single station data to identify sources of near-receiver and near-source scattering. *Bull. Seismol. Soc. Am.*, **80B**, 2227-2241, 1990a.

Gupta, I.N., Lynnes, C.S. and Wagner, R.A., Broadband F-K analysis of array data to identify sources of local scattering. *Geophys. Res. Lett.*, **17**, 183-186, 1990b.

Hedlin, M.A.H., Minster, J.B. and Orcutt, J.A. (1990). Beam-stack imaging of scatterers near a small aperture array. Contributed paper at "*12th annual AFGL/DARPA seism. Res. Symp*", held in Key West, FL.

Key, F.A., Signal-generated noise recorded at the Eskdalemuir seismometer array station. *Bull. Seismol. Soc. Am.*, **57**, 27-37, 1967.

Key, F.A., Some observations and analysis of signal generated noise. *Geophys. J. R. astr. Soc.*, **15**, 377-392, 1968.

Lay, T., Analysis of near-source contributions to early P-wave coda for underground explosions. III. Inversion for isotropic scatterers. *Bull. Seismol. Soc. Am.*, **77**, 1767-1783, 1987.

Lokshtanov, D.E., Ruud, B.O. and Husebye, E.S., The upper crust low velocity layer; a Rayleigh ($R_g$) phase velocity study from SE Norway. *Terra Nova*, **3**, 49-56, 1991.

Luco, J.E. and Apsel, R.J., On the Green's functions for a layered half-space, part I. *Bull. Seismol. Soc. Am.*, **73**, 909-929, 1983.

Lynnes, C.S. and Lay, T., Inversion of P coda for isotropic scatterers at the Yucca Flat test site. *Bull. Seismol. Soc. Am.*, **79**, 790-804, 1989.

Mallick, S. and Frazer, L.N., Po/So synthetics for a variety of oceanic models and their impications for the structure of the oceanic lithosphere. *Geophys. J. Int.*, **100**, 235-253, 1990.

Ringdal, F., Husebye, E.S. and Dahle, A., P-wave envelope representation in event detection using array data. *Exploitation of Seismograph Networks, K.G. Beauchamp, Editor, Noordoff-Leiden*, 1975.

Sereno, T. J. Jr. and Orcutt, J. A., Synthetic seismogram modelling of the oceanic Pn phase. *Nature*, **316**, 246-248, 1985a.

Sereno, T. J. Jr. and Orcutt, J. A., Synthesis of Realistic Oceanic Pn Wave Trains. *J. Geophys. Res.*, **90**, 12755-12776, 1985b.

Sereno, T. J. Jr. and Orcutt, J. A., Synthetic $P_n$ and $S_n$ phases and the frequency dependence of Q in oceanic lithosphere. *J. Geophys. Res.* , **92**, 3541-3566, 1987.

Yilmaz, O., *Seismic data processing*. Society of Exploration Geophysicists, investigations in geophysics, volume 2, 1987.

# Chapter 3

# Regularized deconvolution of noisy seismic array recordings

## Abstract

In this chapter, an algorithm is developed for the deconvolution of a presumed known wavelet from uncertain data. This approach seeks a deconvolved trace (model) that possesses a physically reasonable amount of covariance and produces an acceptable data misfit. Regularization is achieved using the $L_2$ norm to assess data misfit and model roughness (or complexity). The method of Lagrange multipliers is used to control the tradeoff between these 2 characteristics. The noise is assumed to result from a stationary, Gaussian, process. The noise covariance is estimated assuming the process is ergodic and applying an autocorrelation operator to pre-event noise.

Two approaches are taken to introduce the proper level of covariance into the model. In one, akin to the Occam's Razor method of Constable et al.(1987), a straightforward differencing operator is applied to the model vector to yield a smoothed result. In the second approach, a priori knowledge, obtained from physical arguments, is used to provide an estimate of the statistical nature of the model. This information is used to define a correlation operator that is applied to the model vector as a way of seeking a model with an appropriate degree of covariance. In both approaches, it is assumed that the mapping kernel which relates the model to the observed data is known exactly. A series of synthetic models is explored in an attempt to define weaknesses of the approaches. Comparison is made with the spectral division technique.

Full array synthetics are convolved with recorded time series and then deconvolved, after adding noise, to determine the extent to which the resolution of crustal scatterers near seismic arrays can be enhanced by using this processing.

## C.1 Introduction

The imaging analysis introduced in Chapter 2 is based on equation 2.3

$$\tau = \mathbf{R}_{as} \bullet (\mathbf{p}_i - \mathbf{p}_s) \tag{3.1}$$

that assumes impulsive excitation of the local population of scatterers to predict arrival times of scattered phases at seismic receivers. This formula was applied to recordings of teleseismic events to produce images of the scattering field in the vicinity of the NORESS array. If one adopts the simple assumption that the level of excitation of an active scatterer is proportional to the amplitude of the incoming wavefield then it is clear that excitation is not impulsive. Instead, due to the protracted nature of the incoming wavefields, estimated by beamforming, scatterers are repeatedly illuminated by successive arrivals in a typical teleseismic wavetrain. Given this hypothesis, it was concluded in Chapter 2 that formula 2.3 should be used to produce temporal, not spatial, images of the local scatterers. It is clear that further pre-processing of the array records, with the goa. of reducing the effective time span of teleseismic arrivals, is desirable.

## C.2 Analysis of the forward problem

### C.2.a The convolutional model

In an attempt to remedy this situation we assume a simple model for the array records. The motions occurring at the location of an individual sensor, d(t), are real values that result from the convolution of the sensor's impulse response, m(t), hereafter known as the model, and the sequence of arrivals from the primary source, b(t), which we assume is invariant with respect to time shift. In more precise terms, we define the impulse response, m(t), to be the wavefield that would be recorded by that sensor in the event of impulsive excitation by a plane wave with the wavevector appropriate for the teleseismic source. The wavetrain, b(t), goes under many aliases - the transfer function, the basis wavelet, the mapping kernel, the representer, the data kernel, etc. Hereafter, in this chapter, b(t) will be referred to simply as the wavelet. Considering, for the moment, recordings uncorrupted by additive noise:

$$d(t) = b(t) * m(t) = \int_{t_1}^{t_2} b(t - \tau) m(\tau) d\tau = \int_{t_1}^{t_2} g(t, \tau) m(\tau) d\tau \tag{3.2}$$

where * denotes convolution. The model is assumed to have finite support between $t_1$ and $t_2$. $g(t, \tau)=b(t - \tau)$. It is assumed that these motions superpose linearly (and that we have a linear forward, and thus linear inverse, problem). Given that we consider discrete representations of the data, model and wavelet these relations can be rewritten as:

$$d_k = \sum_{j=1}^{N_m} b_{k-j+1} m_j = \sum_{j=1}^{N_m} g_{kj} m_j \tag{3.3}$$

where $g_{kj} = b_{k-j+1}$ is defined from j=1 to j=$N_b$, the number of points in the wavelet. The number of model components is given by $N_m$, the data is recorded at $N_d$ points. Given this discrete representation, the solution of the error-free linear forward problem can be rewritten as a matrix equation

$$\mathbf{d} = \mathbf{Gm} \tag{3.4}$$

where $\mathbf{G}$ is a $N_d$ x $N_m$ matrix that contains the wavelet b(t) and can be defined as follows:

$$\mathbf{G} = \begin{pmatrix} b_1 & 0 & \ldots & \ldots & \ldots & \ldots & 0 \\ b_2 & b_1 & 0 & \ldots & \ldots & \ldots & \ldots \\ \vdots & \vdots & \vdots & \ddots & \vdots & \vdots & \vdots \\ b_n & b_{n-1} & \ldots & b_1 & 0 & \ldots & \ldots \\ 0 & b_n & b_{n-1} & \ldots & b_1 & 0 & \ldots \\ \vdots & \vdots & \vdots & \vdots & \vdots & \vdots & \vdots \\ \ldots & \ldots & 0 & b_n & \ldots & b_2 & b_1 \\ \vdots & \vdots & \vdots & \ddots & \vdots & \vdots & \vdots \\ \ldots & \ldots & \ldots & \ldots & 0 & b_n & b_{n-1} \\ 0 & \ldots & \ldots & \ldots & \ldots & 0 & b_n \end{pmatrix} \tag{3.5}$$

in which case the matrix is not square ($N_d = N_m + N_b - 1$). Given that $N_b$ is greater than one, there are more data points than model parameters to be determined. The problem, as defined above, is likely over-determined. All the direct constraint information we have to form an estimate of the model is contained within Equation C.4. All wavelets, $g_j$, j=1, $N_d$ are linearly independent and thus form the basis for an $N_d$ dimensional linear vector space, known hereafter as the data space. A subspace of the data space encompassing the first $N_m$ points is hereafter referred to as the model space.

*C.2.b The effect of protracted teleseismic wavelets on imaging for local scatterers*

Prior to considering the problem of inverting equation C.4, it seems reasonable to apply the convolutional model to synthetic and recorded data and to assess the effect of a prolonged excitation function on the imaging process. In Figure C.1 is displayed the image computed when a single scatterer
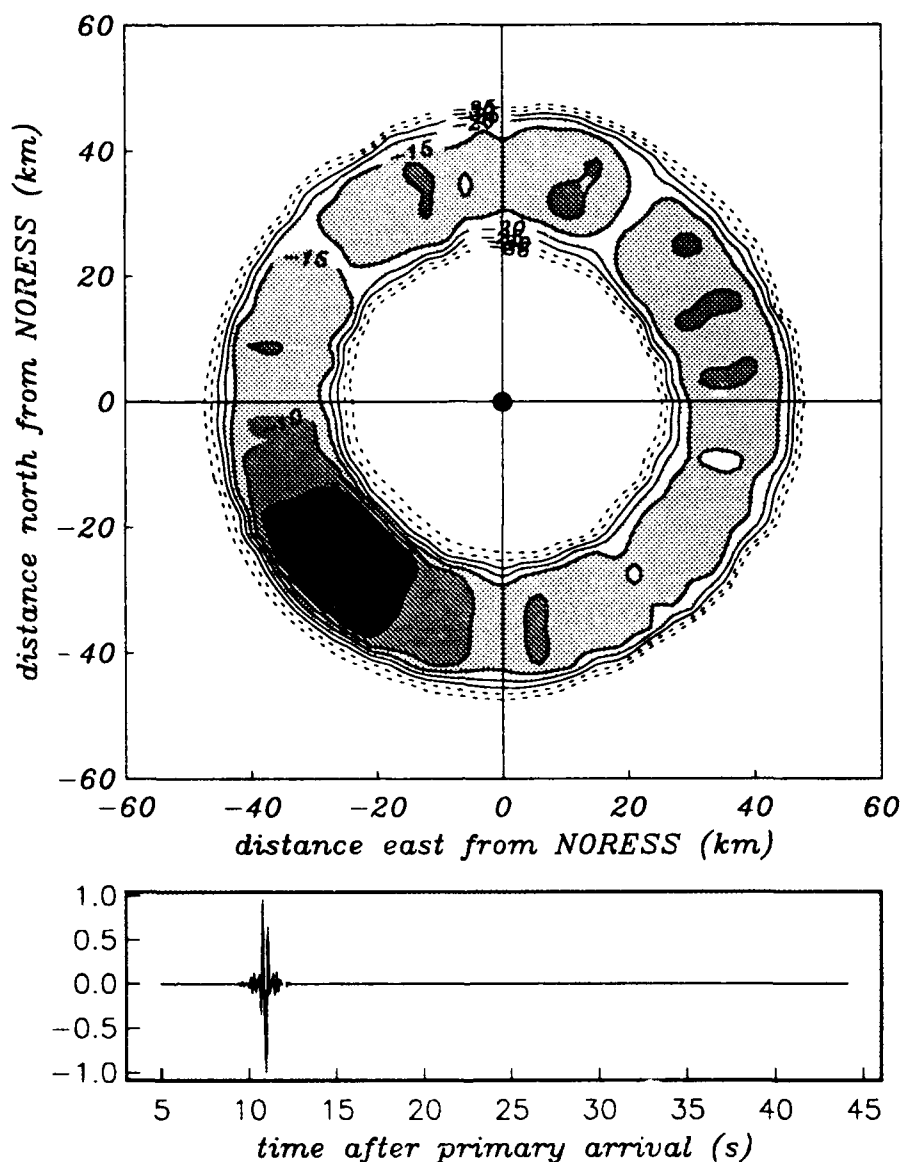
Figure 3.1 Image of a synthetic point source located 35 km from the array at a back azimuth of 225°. Wavenumber Integration was used to generate synthetic seismograms individually for each of the 25 vertical component sensors in the NORESS array (illustrated is the synthetic computed for the center station). In this, and all subsequent images, contour values indicate amplitudes in dB relative to the largest value in the image and cylindrical propagation of scattered wavefronts was assumed.

35 km to the southwest of the NORESS array is excited by a single, impulsive, arrival impinging on the area from directly beneath (it has infinite phase velocity).

The radial resolution is degraded only by dispersion and time-averaging which, in this case, is 5 seconds. The azimuthal resolution of the NORESS array at this range is roughly 20 km, the image sidelobes are not significant. In Figure C.2, we display a recorded teleseism, produced by a Semipalatinsk
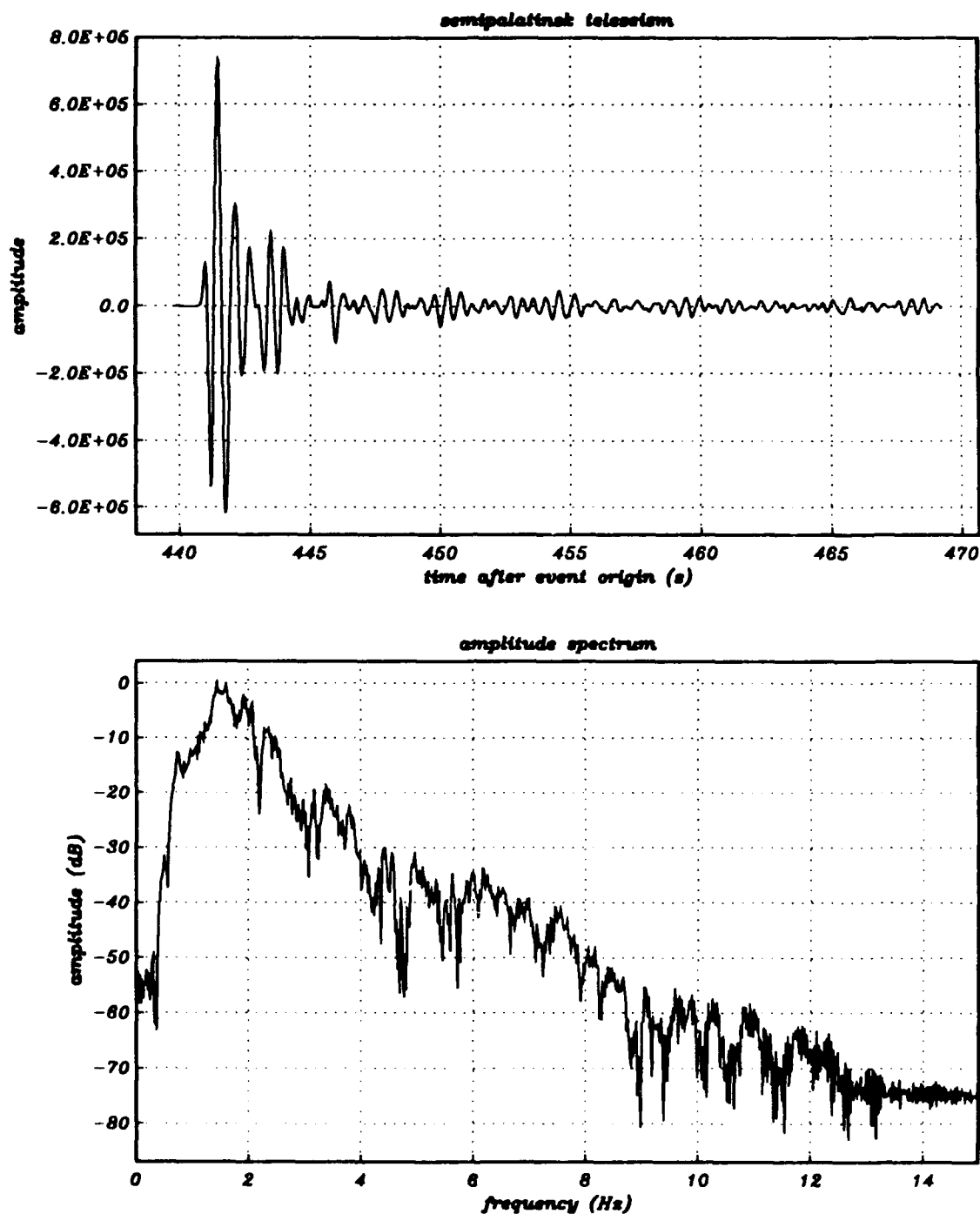
**Figure 3.2** A Semipalatinsk telescismic event recorded by the NORESS array. Displayed in the upper figure is the beam computed using 24 channels, the lower figure displays the amplitude spectrum of this beam.

nuclear explosion (1985, day 351). The character of the wavefield arriving from the explosion has been estimated using simple delay and sum beamforming - we denote this beam as $b_s(t)$. To produce the
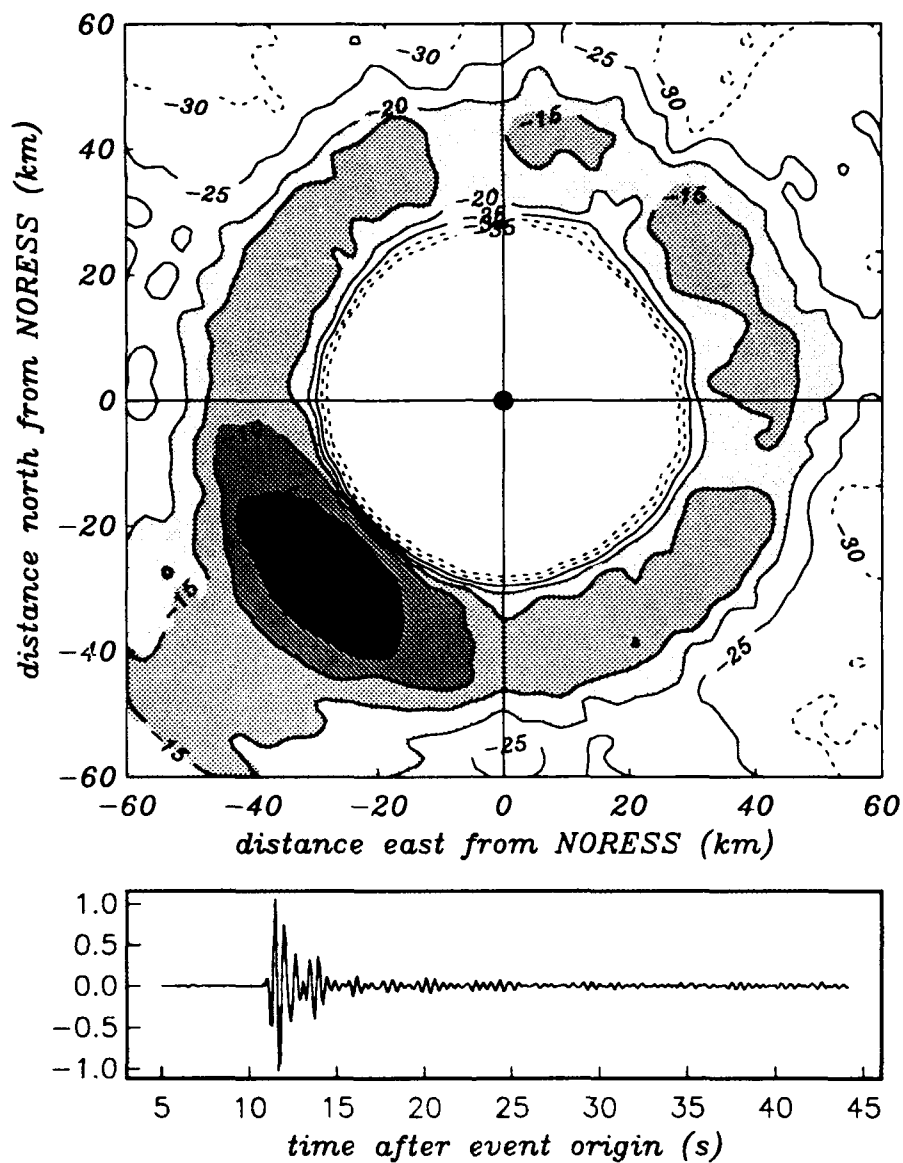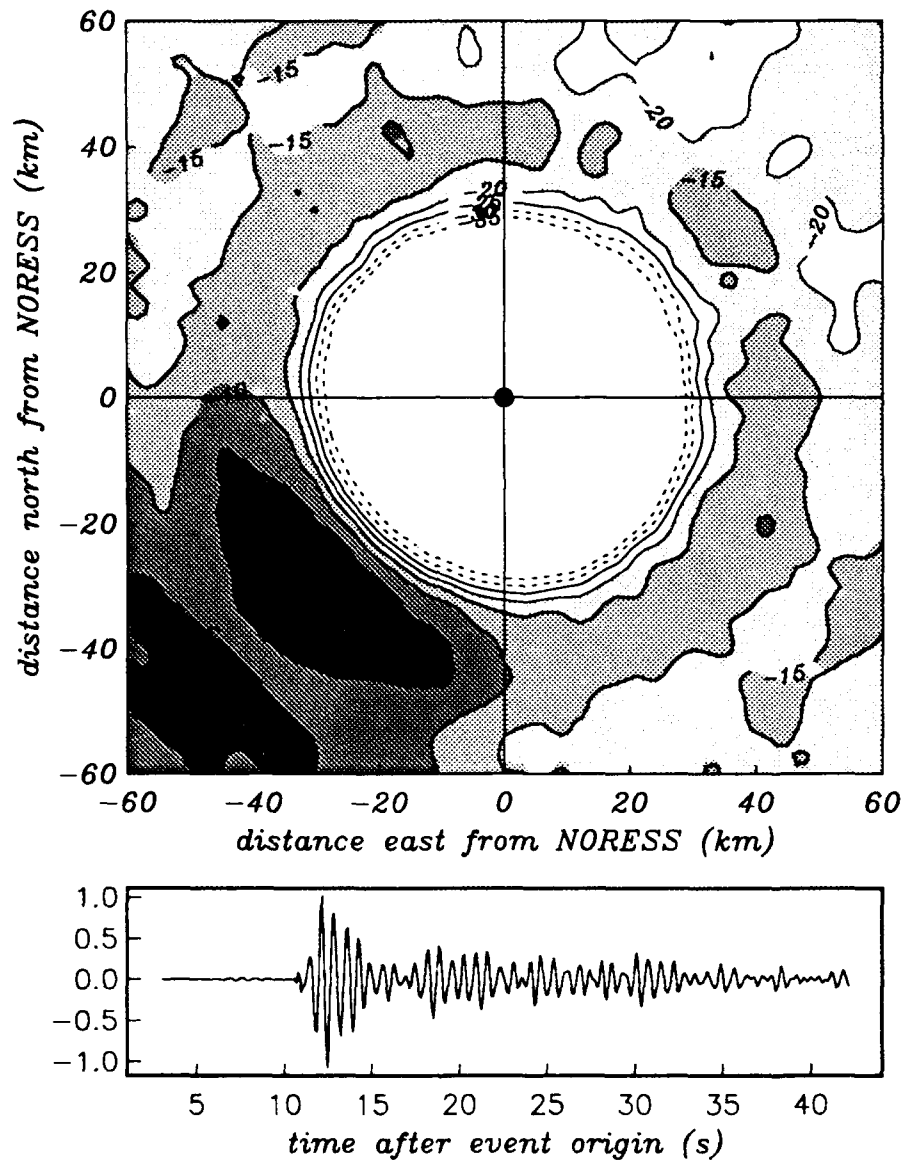
**Figure 3.3** Displayed is the image computed using time series that have resulted from the convolution of the synthetics displayed in Figure C.1 and the recorded teleseism displayed in Figure C.2. Illustrated in the lower figure is the a0 synthetic/recorded seismogram. This figure is included to illustrate what degradation of radial resolution we expect when local point scatterers are excited by a relatively impulsive teleseism.

image in Figure C.3, we have used this teleseism to play the role of the wavelet (excitation function) - the teleseism, $b_s(t)$, has been convolved with the synthetics used to produce Figure C.1.

In the lower part of this figure, a sample seismogram (station a0 - vertical component) is displayed - the convolution has clearly increased the duration of the arrivals. As a result, the image of the point secondary source (displayed in the upper part of Figure C.3) has acquired a "shadow" extending outward from the array originating at the true source of scattered energy - the radial resolution has been

55
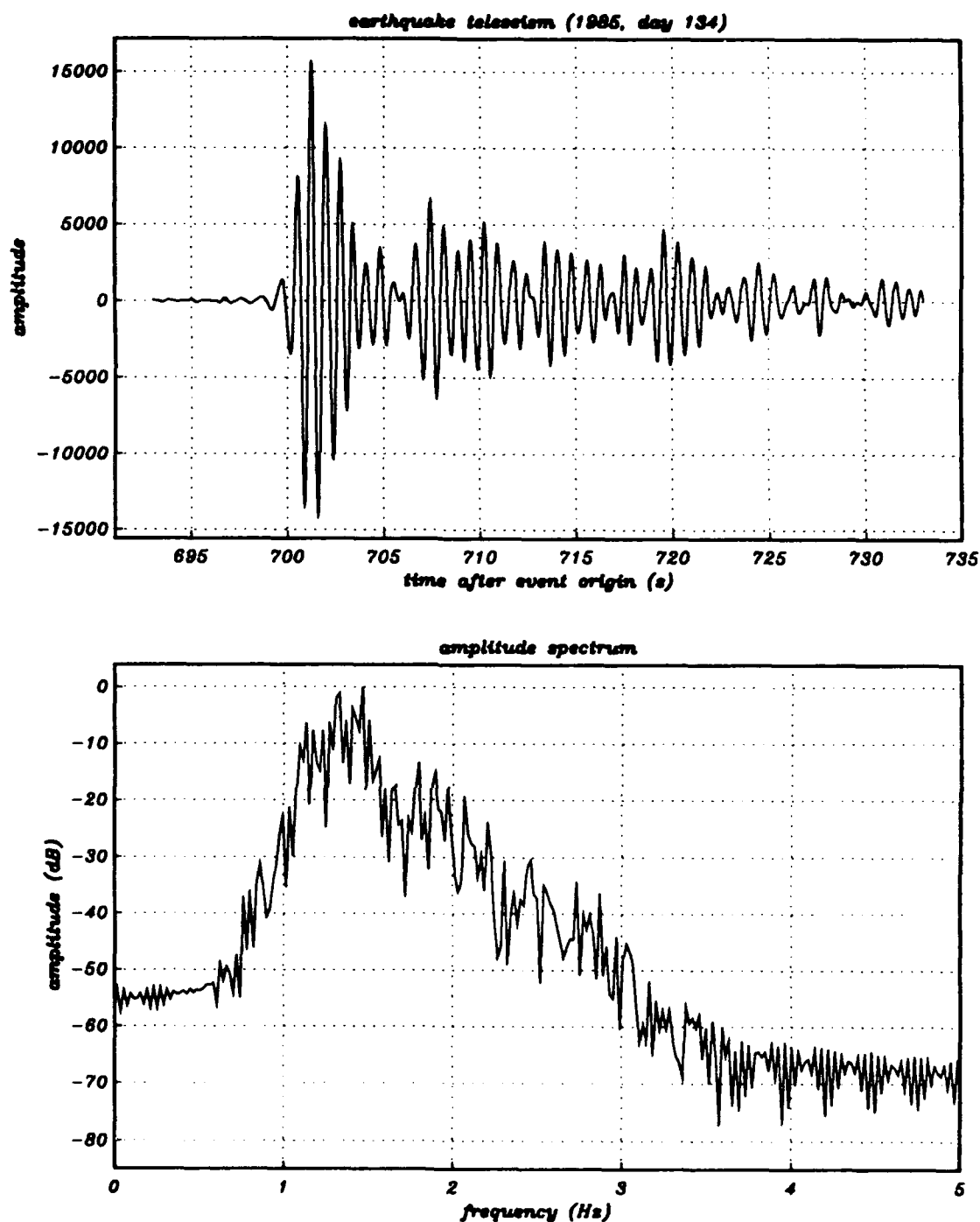
**Figure 3.4** A teleseismic earthquake (1985, day 134) recorded by the NORESS array. Displayed in the upper figure is the beam computed using 25 channels, the lower figure displays the amplitude spectrum of this beam. This event is the same one that appears in Figure 3.11.

seriously degraded. In a second example, we convolve the recording of a teleseismic earthquake ($b_e(t)$; 1985, day 134; Figure C.4) with the synthetics (Figure C.1) to produce the image in Figure C.5. The

**Figure 3.5** Displayed is the image computed using time series that have resulted from the convolution of the synthetics displayed in Figure C.1 and the recorded teleseism displayed in Figure C.4. Illustrated in the lower figure is the a0 synthetic/recorded seismogram. This figure is included to illustrate what degradation of radial resolution we expect when local point scatterers are excited by a relatively protracted teleseism.

"pulsy" nature of the earthquake wavetrain in Figure C.4 has translated directly into the image as discrete concentrations of energy located mainly to the southwest of the true scatterer. Still plotted as a function of space, this image implies the existence of a false source roughly 70 km to the southwest of the array. We know that this energy originated only 35 km from the array but is due to a multiple that arrived roughly 10 seconds after the primary onset. The effect of the teleseismic nuclear explosion on the image of the local scatterers seems relatively light and, given that the convolutional model gives a reasonable

description of how the energy in the wavelet interacts with the scatterers, should be relatively easy to remove. The earthquake, however, is characterized by more significant coda which will be harder to correct. In these synthetic examples, the temporal resolution of the array records, and thus the radial resolution of the images, is being degraded by the protracted nature of the wavelet. Given that the convolutional model introduced at the beginning of this section gives a reasonable description of the process at work, it seems likely that a similar process degrades the quality of the images presented in Chapter 2. The goal of this chapter is to develop a means by which the radial resolution of the images can be enhanced without degrading the azimuthal resolution. The quality of images produced using recorded data will be increased if the basic seismic wavelet can, in effect, be compressed into a delta function so we can use the impulse response to image the local population of scatterers. The goal of the next section is to derive a means whereby the inverse problem can be solved. Basically, the matrix equation, C.4, has to be inverted, or the wavelet within G is to be deconvolved from the data vector, d, to yield an estimate of the model, $\hat{m}$.

## C.3 Inversion methodology

As we've seen above, the convolution of the impulse response of a system with a non-impulsive function leads to a loss of resolution, or a blurring of detail. A large number of attempts have been made to reverse this process, or deconvolve the data for the underlying impulse response. This section describes three approaches.

### C.3.a Deconvolution by spectral division

One technique that has been used involves a straightforward use of the convolution theorem. Representing angular frequency by $\omega$, if $D(\omega)$, $B(\omega)$ and $M(\omega)$ are Fourier transform pairs of d(t), b(t) and m(t) respectively then by Fourier transforming equation C.2 we find that:

$$D(\omega) = B(\omega)M(\omega) \tag{3.6}$$

An estimate of the spectrum of the model, $\hat{M}(\omega)$ can be found using spectral division:

$$\hat{M}(\omega) = D(\omega)B^{-1}(\omega) \tag{3.7}$$

and the underlying model estimate, $\hat{m}(t)$ can be found by inverse Fourier transformation. At first sight, this technique seems like it should work well, however in practice spectral holes exist in B($\omega$) making its inversion unstable - straight division amplifies frequencies absent from B($\omega$) which produces ringing in $\hat{M}(\omega)$. In practice, the inversion is stabilized by filling in the spectral holes (or, so to speak, raising the water level) present in B($\omega$) prior to division in a process known as pre-whitening (Yilmaz, 1987). The degree to which the holes are filled up is most often determined by visual inspection of $\hat{m}(t)$ and thus the technique is, in general, highly subjective. This approach, however, reveals an important aspect of the inversion that, given a finite number of inexact observations, cannot be avoided. It is well known (Parker, 1977) that the problem of inverting a linear forward problem for a discrete, or continuous, model given a finite set of inexact observations is non-unique. The challenge lies in finding an inversion scheme that avoids the *ad hoc* selection of a single model.

### *C.3.b Wiener filtering - seeking the maximum resolution and the best data-misfit*

As discussed by Oldenburg (1981) a powerful alternative solution of this linear forward problem lies in the inversion formalism of Backus and Gilbert (1967,1968,1973). At the heart of this approach is the lesson that, given the finite, inexact, nature of the observations, a single, exact, model cannot be produced. It is possible only to estimate blurred versions of the true model using linear combinations of the observations. In matrix form the latter part of this statement can be rewritten as:

$$\hat{m} = Ad \tag{3.8}$$

or explicitly defining the terms involved:

$$\hat{m}_j = \sum_{k=1}^{N_d} a_{jk} d_k \tag{3.9}$$

combining equations C.3 and C.8 we find that:

$$\hat{m}_j = \sum_{i=1}^{N_m} \sum_{k=1}^{N_d} a_{jk} g_{ki} m_i \tag{3.10}$$

letting

$$R_{ji} = \sum_{k=1}^{N_d} a_{jk} g_{ki} \tag{3.11}$$

where **R** is generally known as the resolution kernel, we find that:

$$\hat{m}_j = \sum_{i=1}^{N_m} R_{ji} m_i \qquad (3.12)$$

The resolution kernel describes the degree to which the true model is blurred. It could be argued that we might want to seek those data weights, a, which yield the greatest resolution, or the most time limited resolution kernel. The greatest resolution that the data allow can be found by making a as close as possible, in the least squares sense, to the delta function ($\delta$). This result can be found by minimizing:

$$U = \sum_{i=1}^{N_m}(\sum_{k=1}^{N_d} a_{jk} g_{ki} - \delta(i,k))^2 \qquad (3.13)$$

with respect to the data weights, a. It can be shown that, provided $\mathbf{G}^T\mathbf{G}$ is non-singular, this yields the following solution, expressed in matrix form:

$$\mathbf{A} = (\mathbf{G}^T\mathbf{G})^{-1}\mathbf{G}^T \qquad (3.14)$$

This set of weights also yields the model that has the smallest Euclidean norm, or is smallest in the least squares sense and yields the smallest data misfit, as measured by the method of least-squares - it is a minimum error variance technique (Mendel, 1983). This result is known as the unconstrained Wiener shaping filter (Treitel and Robinson, 1966; Oldenburg, 1981 and Menke, 1984). In the unlikely event that the observations are uncorrupted by noise the predicted data, $d_p$, are given by

$$\mathbf{d}_p = \mathbf{G}(\mathbf{G}^T\mathbf{G})^{-1}\mathbf{G}^T\mathbf{d} \qquad (3.15)$$

which, by inspection, shows that the data are predicted exactly. The matrix which premultiplies the observed data vector is known as the data resolution matrix ($\mathbf{R}_d$; Menke, 1984) and, in this case, equals I, the identity matrix.

*3 e An approach to deconvolution that allows for a tradeoff between data misfit and model simplicity*

There are several reasons why the current imaging analysis should benefit from a less specific approach. In practice, it is always true that the observations are corrupted by noise. An equation that

gives a more realistic description of the forward problem, than is provided by equation C.4, is

$$d = Gm + n \qquad (3.16)$$

where the vector, n, represents the additive noise. We need an approach that will yield a model that produces the correct level of data-misfit (given data made inexact by noise, an exact fit is no longer desirable). Furthermore, it is appropriate to cast the solution in a way that will allow the introduction of *a priori* information, such as that which describes the expected, or desired, character of the model.

As in many other inverse problems, the model we seek suffers from a number of undesirable qualities that we want to suppress simultaneously (in this case model complexity and the inability to reproduce the input data). A constrained optimization that will allow us to control model complexity and vary the fidelity with which we reproduce the input data can be achieved using the method of Lagrange multipliers. Following this approach, we define the trade-off functional, U, as follows:

$$U = \|Om\|^2 + \mu^{-1}\{\|Gm - d\|^2 - X^2\} \qquad (3.17)$$

where the norm used is the standard Euclidian norm, O is an, as yet, undefined operator that we apply to the model vector and $X^2$ is the mean square misfit. One reason why this approach is attractive is that it is general, in the sense that we are free to use *a priori* information to define the norms in the way we feel best suits the problem at hand.

Considering the problem which has motivated the work in this chapter, there are several sources of noise. In addition to cultural sources, local wind, and spring runoff, an important source of noise in the vicinity of the NORESS array is microseismic noise, generated by interactions between swell propagating in opposite directions, for example in the North Sea (Fyen, 1986). The wind energy is converted to acoustic energy within the water column and then to seismic energy at the seafloor. The dominant period of microseismic noise shows some variation (Hedlin and Orcutt, 1989) but tends to lie in the band from 3 to 10 seconds. Given that the NORESS array records are digitized at 40 Hz, it is immediately apparent that the noise in this dataset must be correlated and the inversion theory should accommodate this complexity. Considering the complex nature of the noise, that many sources are simultaneously at work, we assume the added vector, n, is a single realization of a stationary random process, N(t), that obeys Gaussian statistics. By definition, assuming N(t) has been demeaned, the noise autocovariance is defined as:

$$R(\tau) = E\{N(t), N(t + \tau)\} \qquad (3.18)$$

where E denotes the expectation operator. Since we have only a single realization of N(t) in the pre-event noise sample we assume ergodicity and estimate $R(\tau)$ by a simple delay and sum operation over J points:

$$R(j\Delta t) \approx \frac{1}{J} \sum_{i=1}^{J-j} n(t_i)n(t_i + j\Delta t) \qquad (3.19)$$

and use this information to construct a Toeplitz autocovariance matrix, $C_{nn}$, where the $(i,j)^{th}$ element is given by $R((i - j)\Delta t)$. We assume, for the time being, that no error exists in G, and thus, give, the assumed Gaussian nature of N(t), that an appropriate measure of data misfit uses the Euclidean, or $L_2$, norm:

$$\|Gm - d\|^2 = (Gm - d)^T C_{nn}^{-1} (Gm - d) \qquad (3.20)$$

This misfit measure, known as the method of weighted least squares (Priestley, 1981), is essentially the one used by Constable et al.(1987). However, in the present work the noise is allowed to possess an arbitrary degree of covariance. As argued by Constable et al.(1987), in the event the errors result from a zero-mean, Gaussian, process and is uncorrelated the expected misfit, after normalization, is 1. As illustrated by Journel (1989), this is still true when the errors are correlated. The covariance matrix $C_{nn}$, operating in this manner within the norm, rotates the correlated vector $Gm - d$ such that the norm can be rewritten as the dot product of a new uncorrelated vector which has a covariance matrix that equals I, the identity matrix. Thus the expected rms misfit is still 1. The statistics underlying the model are not so easily analyzed - when dealing with recorded data, no model sample exists (it is what we seek) and so model statistics must be inferred using less direct means. In one approach that has been taken to this type of problem (i.e., Shaw and Orcutt, 1985; Constable et al., 1987), a simple (smooth) model is sought by applying a "roughening matrix", R, to the model vector. The roughening matrix is generally a first, or second, order discrete differencing operator. Following these authors, we define the $L_2$ model norm as follows.

$$|m|^2 = (Rm)^T(Rm) = m^T R^T Rm \qquad (3.21)$$

Expanding the right side of equation C.17, after substituting equations C.20 and C.21:

$$U = m^T R^T Rm + \mu^{-1}\{m^T G^T C_{nn}^{-1}Gm - 2m^T G^T C_{nn}^{-1}d + d^T C_{nn}^{-1}d - X^2\} \qquad (3.22)$$

Following the method of Lagrange multipliers, to find the model vector that yields the smallest functional,

U, we differentiate the functional with respect to m and force the result to vanish.

$$\frac{\partial U}{\partial m} = 0 = R^T R m + \mu^{-1} G^T C_{nn}^{-1} G m - \mu^{-1} G^T C_{nn}^{-1} d$$

$$G C_{nn}^{-1} d = \mu R^T R m + G^T C_{nn}^{-1} G m$$

$$\left( \mu R^T R + G^T C_{nn}^{-1} G \right) m = G^T C_{nn}^{-1} d$$

These steps yield a model estimate:

$$\hat{m} = \left( R^T R + \mu^{-1} G^T C_{nn}^{-1} G \right)^{-1} \mu^{-1} G^T C_{nn}^{-1} d \qquad (3.23)$$

Hereafter we refer to this model estimation procedure as method B. This approach is attractive because it guarantees that no unnecessary structure is given to the model - and thus it has been named the "Occam's Razor" approach. The degree to which structure is suppressed is determined by the order of the derivative. One limitation of this approach exists because it does not allow a rigorous selection of a model roughening operator. It simply uses the *a priori* belief that the model should be simple (smooth) - it is somewhat *ad hoc* since it is not known what degree of derivative is appropriate for the model, one is chosen that yields a visually appealing result. There is an alternative approach that can be taken when sufficient prior information exists that indicates what covariance should be present in the model. The matrix $R^T R$ is a roughening operator which, when applied to the model vector within the functional (equation C.17) yields a smoother, or more correlated model. There exist non-singular correlation operators that, when inverted and applied to the model vector within the functional C.16, also yield a more correlated model. We denote such an operator by $C_{mm}$. If we return to C.17 and replace $R^T R$ with $C_{mm}^{-1}$ we redefine the model norm by:

$$\| m \|^2 = m^T C_{mm}^{-1} m \qquad (3.24)$$

The trade-off functional, U, becomes:

$$U = m^T C_{mm}^{-1} m + \mu^{-1} \{ (Gm - d)^T C_{nn}^{-1} (Gm - d) - X^2 \} \qquad (3.25)$$

Following the steps taken above to define equations C.22 to C.23 we find that the estimate of the model can be cast in the following form:

$$\hat{m} = \left( C_{mm}^{-1} + \mu^{-1} G^T C_{nn}^{-1} G \right)^{-1} \mu^{-1} G^T C_{nn}^{-1} d \qquad (3.26)$$

63

If the model vector is due to a stationary process and if $C_{mm}$ is the covariance matrix that describes this process, this operator, when applied in this manner (Equation C.24), will introduce the proper degree of correlation into m. Arguments can be made that the scattered wavefields should be stationary (ex. Frankel and Wennerberg, 1987). These arguments are based on the assumption that the underlying scatterers are distributed randomly. The current study is deterministic in nature, the number of the scatterers is not known beforehand but is assumed to be small. The scattered wavefields we are inverting for are not expected to be stationary. Since we believe the model we seek is a transient, it is probably safest to consider $C_{mm}$ simply as a smoothing operator that, hopefully, can be defined, given *a priori* information, to introduce the proper degree of correlation into the transient model vector. If we follow the hypothesis that the locally scattered phases are generated by the interaction of incident wavefields and topographic features, then knowing the scale length of the topography, and the velocity of propagation of the incident energy, we should be able to make an educated guess as to what correlation should be present in the model. In the next section we will use synthetics in an attempt to determine if this is true, and, if so, the extent to which the result can be improved.

This result (C.25) is somewhat awkward since the inverses of the correlation matrices must be computed to estimate the model. It has been shown (eg. Tarantola, 1981) that

$$G^{T} + G^{T}C_{nn}^{-1}GC_{mm}G^{T} = G^{T}C_{nn}^{-1}\left(C_{nn} + GC_{mm}G^{T}\right) = \left(G^{T}C_{nn}^{-1}G + C_{mm}^{-1}\right)C_{mm}G^{T} \quad (3.27)$$

given that $C_{nn} + GC_{mm}G^{T}$ and $G^{T}C_{nn}^{-1}G + C_{mm}^{-1}$ are positive definite. Since $C_{mm}$ and $C_{nn}$ have Toeplitz form they are positive definite and, thus, so are their inverses. As a result,

$$\left(G^{T}C_{nn}^{-1}G + C_{mm}^{-1}\right)G^{T}C_{nn}^{-1} = C_{mm}G^{T}\left(C_{nn} + GC_{mm}G^{T}\right)^{-1} \quad (3.28)$$

and equation C.29 becomes:

$$\dot{m} = C_{mm}G^{T}\left(\mu C_{nn} + GC_{mm}G^{T}\right)^{-1}d \quad (3.29)$$

If the model and noise are stationary, stochastic, processes and are uncorrelated with each other, this result has the form of the stochastic inverse of Franklin (1970). It is only necessary to compute a single matrix inverse to obtain an estimate of the model. However, given the definition of G in Equation C.5, this matrix is larger than the one appearing in equation C.23 ($N_d$ by $N_d$ vs $N_m$ by $N_m$) and it is still necessary to invert $C_{nn}$ to calculate misfit. To invert for model estimates, equations C.23 and C.29 are solved in steps by varying $\mu$ and using equation C.19 to determine when an acceptable misfit has

been achieved. This result encompasses the Wiener shaping filter. If there is no noise, or $\mu=0$ (infinite emphasis is placed on misfit) and the model is assumed to be uncorrelated then equation C.29 simplifies to equations C.8 and C.14. Hereafter, we refer to the method described by equation C.29 as method C.

### C.3.d Wavelet estimation

In Chapter 2, we found that the best practical means of estimating the character of the excitation function (referred to as the wavelet in this chapter) is via beamforming. This estimation procedure is imperfect, due to seismic noise, locally scattered phases and the fact that the incoming wavefield contains a spectrum of wavenumbers. This beam, which will be denoted by $\hat{b}(t)$, is an imperfect representation of the wavelet b(t), but is, nonetheless, assumed by the preceding theory to be an exact representation. To remedy this problem, we could apply the approach developed by Tarantola (1982) which allows for uncertainty in b(t). Another alternative is to consider the current problem and judge whether this additional labor is likely to yield much improvement. Assuming that the signal does not vary between channels but the noise is spatially uncorrelated, the noise in $\hat{b}(t)$ is expected to be a factor of $\sqrt{N}$ down from the noise levels in the individual channels (Lacoss, 1975; Husebye et al., 1985). The NORESS array, for example, has 25 sensors so the noise level in $\hat{b}(t)$ should be roughly $\frac{1}{5}$ the level in each channel. In the next section we attempt to assess the impact of such an error on a synthetic example.

The wavelet deviates further from the true "excitation function" since the former must be truncated at a reasonable point. The impact of finite wavelet length is also considered in the next section.

## C.4 Deconvolution of several synthetic time series

Prior to applying the technique to the pre-processing of array records, the method and software have been tested on a variety of synthetic datasets. The advantage of the synthetic data, and the reason that it is valuable for testing purposes, is that it is completely controlled. As a result, all aspects of the inversion can be tested since it is known, under all circumstances, what the outcome should be.

### C.4.a Uncorrelated noise and model

The initial tests have been made on a simple dataset, one in which the wavelet is known to be

**basic wavelet**
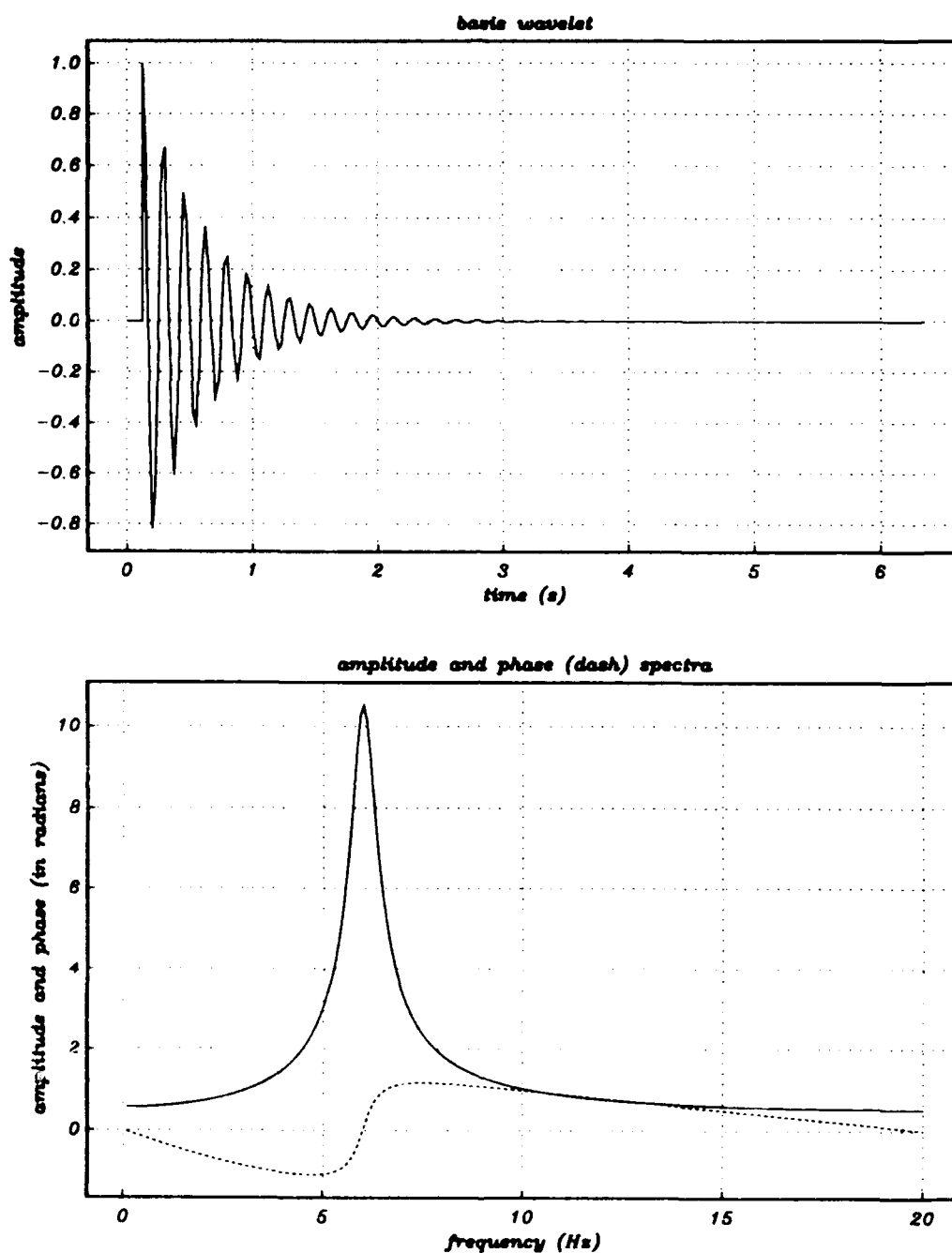


**amplitude and phase (dash) spectra**

Figure 3.6 A synthetic minimum phase wavelet (described in the text). The amplitude and phase spectra are displayed in the lower figure.

a simple. narrow-band, time decaying sinusoid described by.
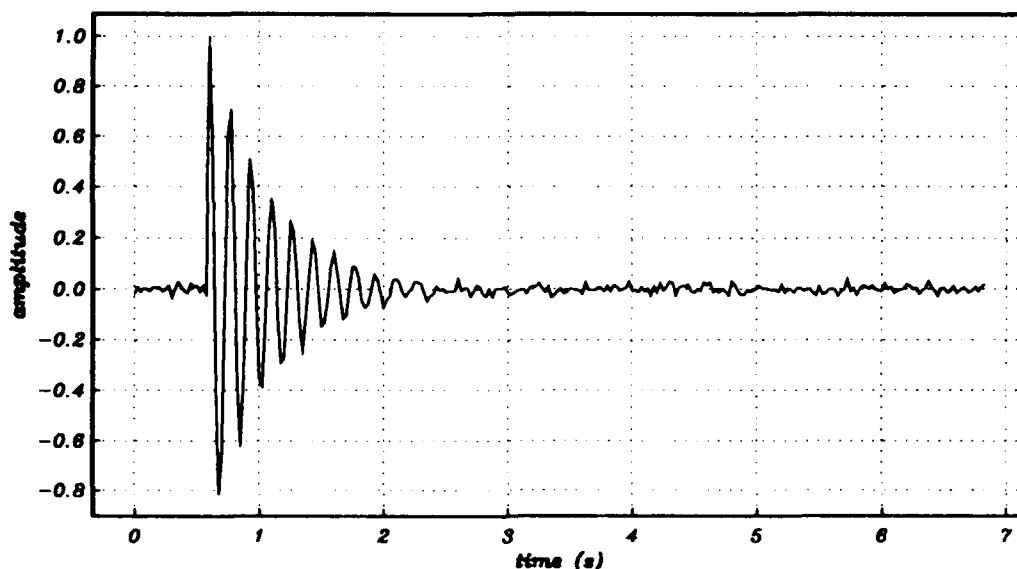
$$b(t) = H(t - t_0)cos(2\pi f_0 t)exp(-\alpha(t - t_0))$$  (3.30)

Figure 3.7 A synthetic time series produced by convolving a delta function (at t=0.6 s) with the wavelet displayed in the preceding figure. Uncorrelated, Gaussian, noise ($\sigma$=0.0002) has been added. This synthetic has a signal to noise ratio comparable to the best events in the NORESS dataset.

The sinusoid is multiplied by the heaviside step function, $H(t-t_0)$ to provide an abrupt onset at $t=t_0$, $\alpha$ controls the rate of decay of the exponential. This wavelet is the result of an, admittedly simple-minded attempt to mimic a typical teleseism encountered in the NORESS dataset. Although the input sinusoid is monochromatic (at frequency $f_0$), as illustrated in Figure C.6 some bandwidth is present, due to the exponential decay and finite length. In this subsection, all input time series are constructed usirg uncorrelated models and uncorrelated noise - consequently both methods, B and C, give exactly the same results ($C_{nn}$ and $C_{mm}$, or $R^T R$) are diagonal matrices. The time series in Figure C.7 has resulted from the convolution of the wavelet with a delta function (at $t_0$=0.6 s) and the addition of uncorrelated Gaussian noise ($\sigma^2$=.0002). This model provides an interesting challenge to methods B and C since these approaches both employ the $L_2$ norm to assess model "size" and data misfit and thus assume these elements obey Gaussian statistics. In this synthetic, the added noise belongs to a stationary Gaussian process, the model parameters clearly do not. While all points, except one, are zero, the one exception (the $\delta$ function) is a significant outlier (at 0.6 s the model has a value of 1.0). The output models of 4 successive inversions are displayed in Figure C.8; the data misfits are displayed in Figure C.9. From inversions 1 to 3, the Lagrange multiplier, $\mu$, decreases and the models are clearly becoming rougher since more emphasis is being placed on misfit. The Lagrange multiplier acts as the only model
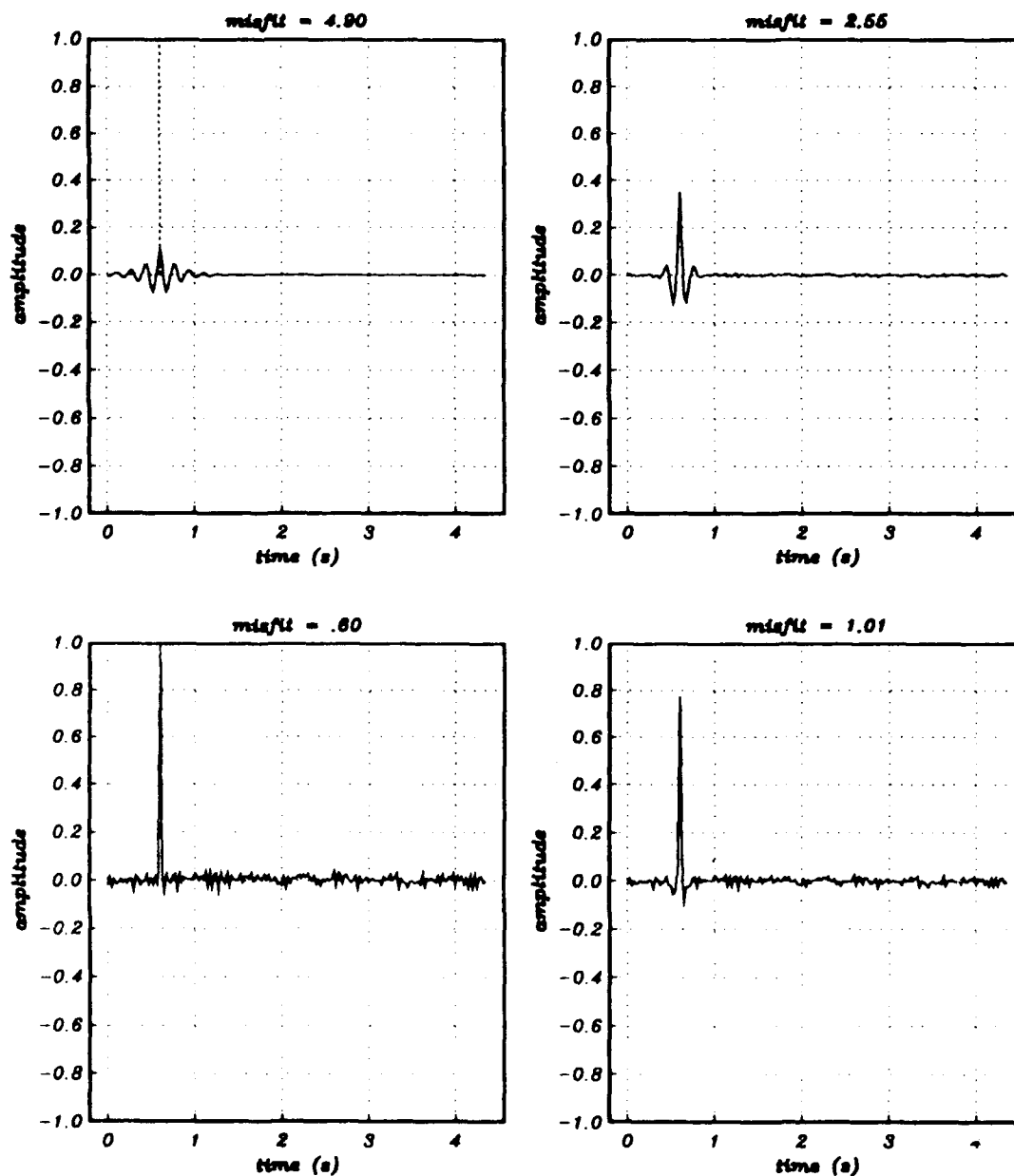
**Figure 3.8** Displayed in this figure are models resulting from deconvolving the wavelet displayed in Figure C.6 from the time series displayed in Figure C.7. Four inversions resulting from progressively smaller Lagrange multipliers are included. The dashed line in the upper left-hand figure indicates the known, correct result. The lower right-hand model has been selected since it yields an rms data misfit of 1.01.
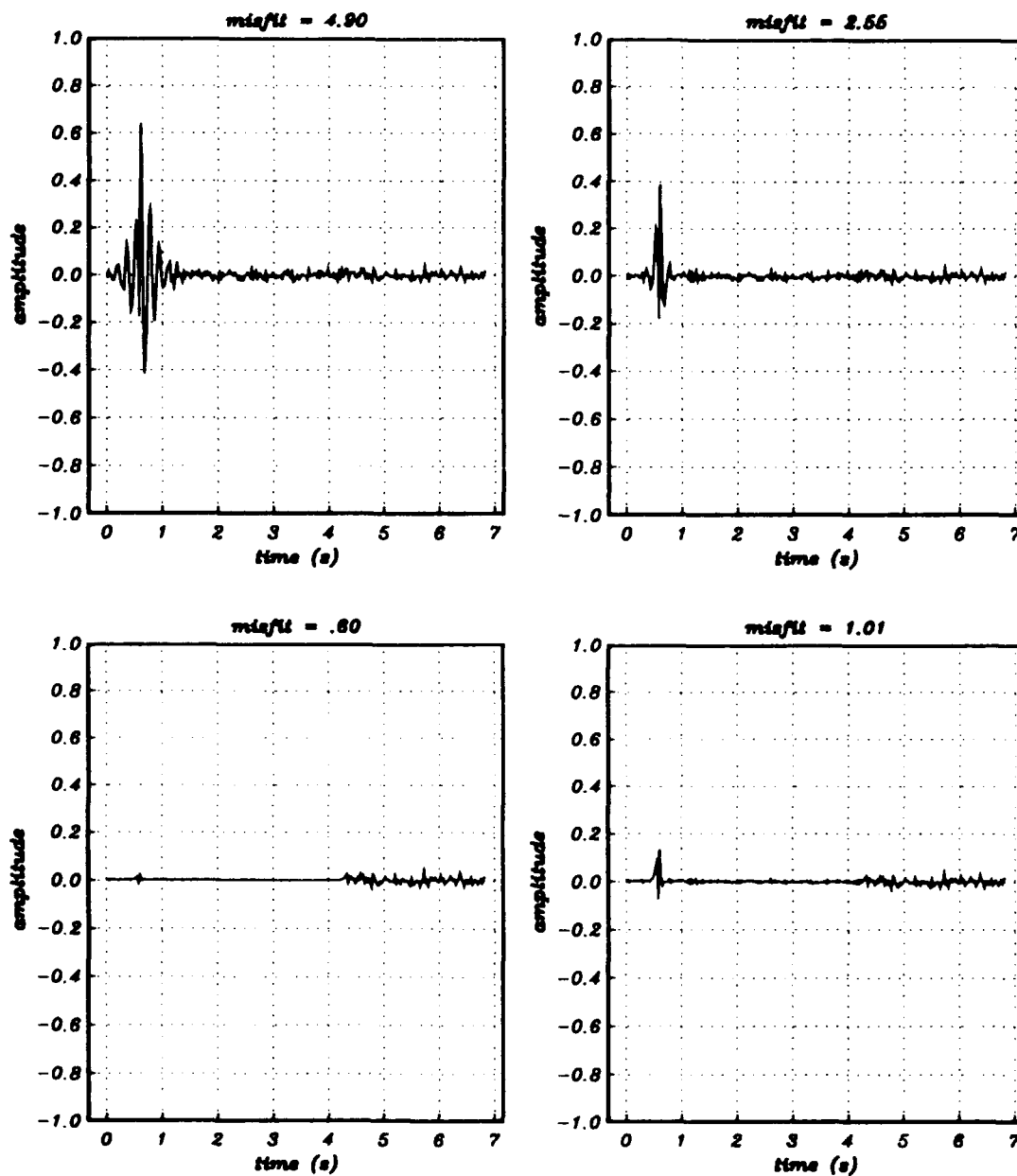
**Figure 3.9** Displayed in this figure are data residuals resulting from deconvolving the wavelet displayed in Figure C.6 from the time series displayed in Figure C.7. The residuals present in inversions, resulting from the four models displayed in Figure C.8, are included. The lower right-hand figure illustrates that the selected model provides overfitting of the data in the model space with the exception of the points in the vicinity of the delta function (at 0.6 s).
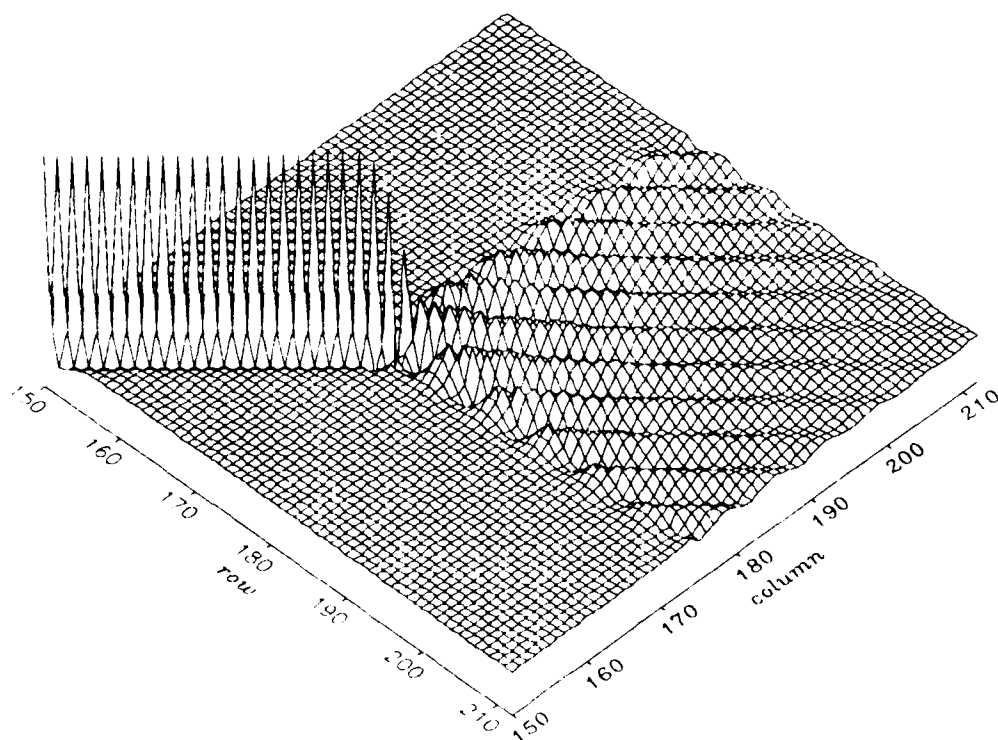
Figure 3.10 A portion (rows and columns from 150 to 212 of 274) of the data-resolution matrix ($R_d$) for the inversion displayed in figures C.7 and C.8. The model space ends at row/column 175.

smoothing parameter since no smoothing is caused by $C_{mm}$ and $(R^T R)$ since they are identity matrices. By inspection of equation C.17 it is clear that in the limit where $\mu$ vanishes, we get the model with the greatest resolution. From inspection of Figure C.8, three problems with the preferred model (lower right-hand corner) immediately become apparent. The delta function amplitude is underpredicted (by 22%), the delta function is accompanied by side lobes and a significant amount of noise has been introduced into the model. In Figure C.9 it can be seen that at a misfit of 1.01, the most significant discrepancy between input and predicted data occurs at the location of the delta function (0.6 seconds). The data are being over-fit where the model has support (from 0.0 to 4.35 s) and the expected amount of misfit is occurring outside the model space (from 4.37 s to 6.825 s).

It is possible to describe why the data misfits are unusually distributed by considering the manner in which the predicted data $d_p$ relate to the input data. Using equations C.4 and C.29 we find that:

$$d_p = GC_{mm}G^T \left( \mu C_{nn} + GC_{mm}G^T \right)^{-1} d \qquad (3.31)$$

70

**rms misfit vs Lagrange multiplier**

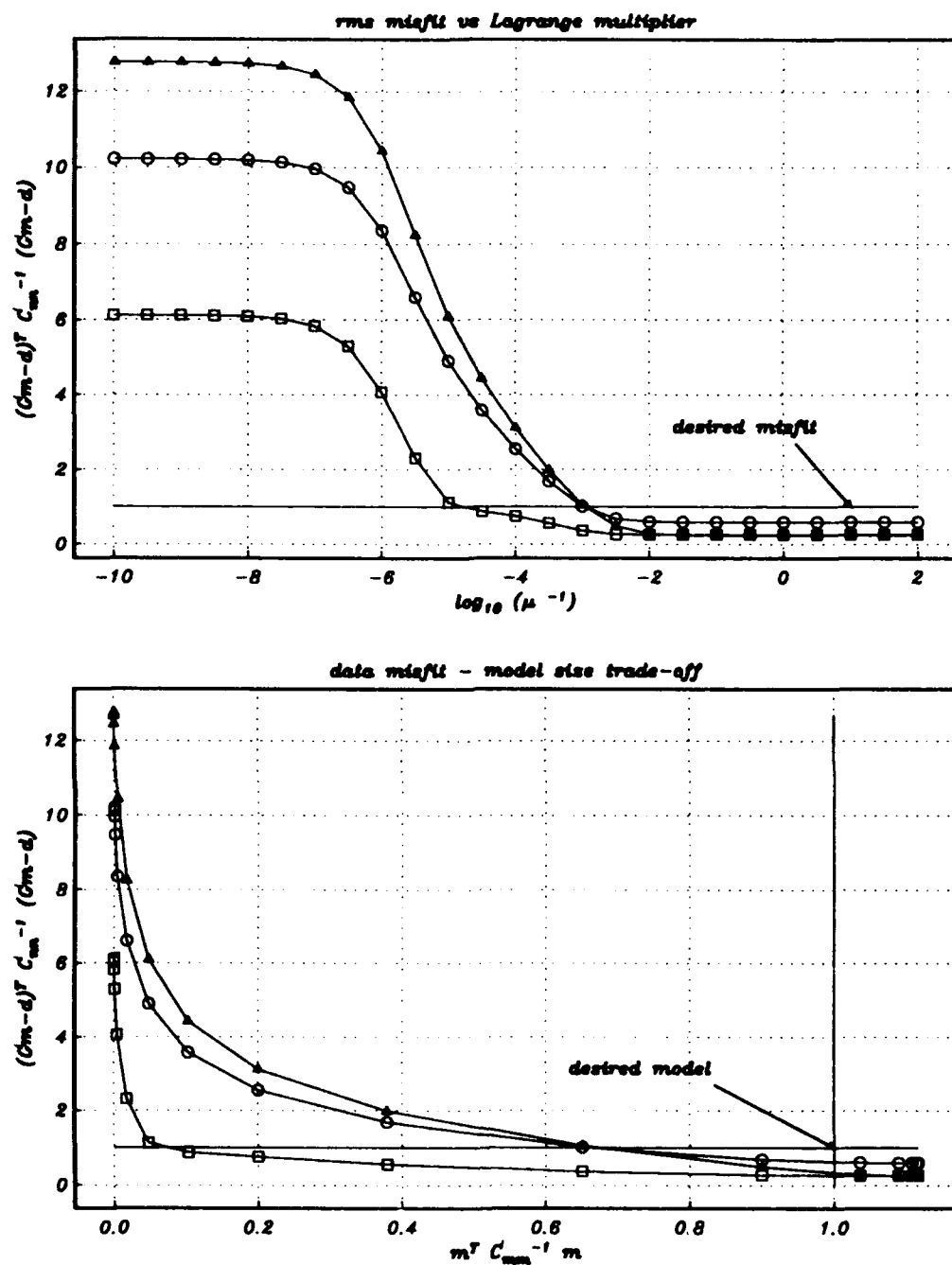**data misfit — model size trade-off**

Figure 3.11 The upper figure illustrates dependence of the data misfit on the Lagrange multiplier ($\mu$) for the inversion considered in Figures C.7 to C.10. The curves highlighted by the circles, triangles and squares represent the misfit measured over the data space, the model space and the portion of the model space from 1.0 to 4.0 s. The lower figure results from the same data however the trade-off illustrated is between data misfit and model size. As in the upper figure, $\mu$ decreases from left to right. In both figures, the horizontal line (at an rms misfit of 1.0) represents the desired misfit. The input model lies on the vertical line in the lower figure. In the lower figure, the horizontal axis scale has been magnified by a factor of 14.4 to allow visual inspection of detail.
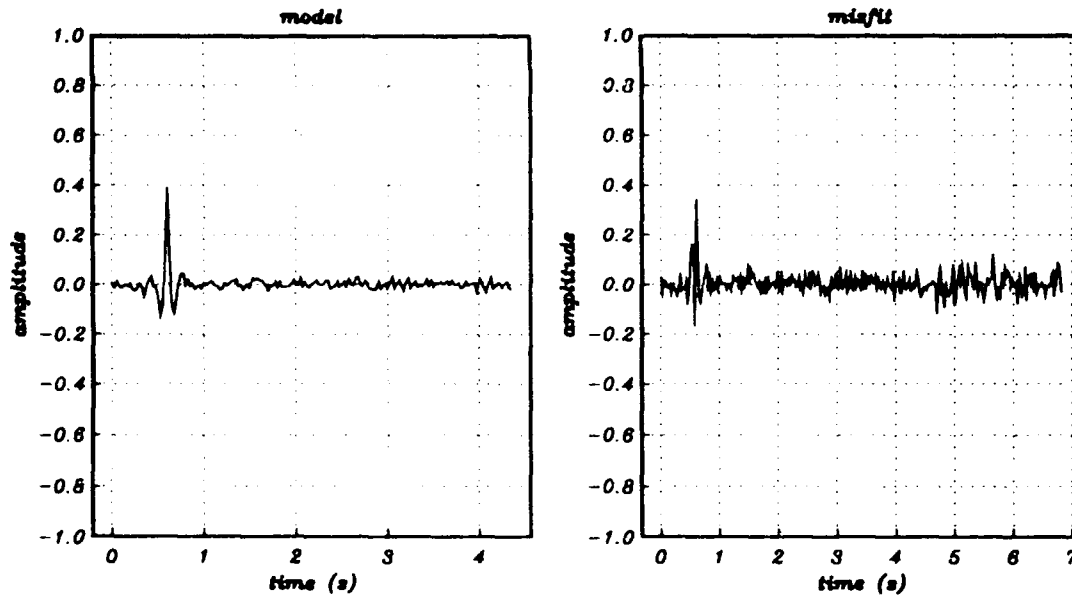
**Figure 3.12** The left figure illustrates the model that yields an rms data misfit of 1.0 when the wavelet (Figure C.6) is deconvolved from a time series identical to that displayed in Figure C.7 except that the noise level has 10 times the variance ($\sigma = 0.002$). The higher noise level has resulted in a smaller main lobe with larger side lobes. The figure on the right illustrates that a relatively large misfit is occurring in the vicinity of the delta function, and overfitting is occurring over the rest of the model space.

If the matrix that premultiplies the input data vector, the data resolution matrix, $R_d$, is equal to I, the identity matrix, the data are predicted exactly. This occurs when the noise has zero variance, or in the limit where the Lagrange multiplier $\mu$ vanishes (misfit is considered to be of the upmost importance). In this inversion, neither of these conditions exist. In general, $GC_{mm}G^T$ possesses small eigenvalues and the noise correlation matrix, $C_{nn}$, is needed to stabilize the inversion. As a result, this added component prevents the data resolution matrix from achieving the form of an identity matrix.

The impact of $\mu C_{nn}$ is greatest at the lower right hand corner of $GC_{mm}G^T$ where values are small due to the decay of the wavelet. The inverse of the sum $\mu C_{nn} + GC_{mm}G^T$ is thus significantly changed from the inverse of $GC_{mm}G^T$ and, as a result, $R_d$ deviates from I. In this case, the edge effect appears in Figure C.9 as bloated residuals (data-misfits) beyond the model space. A portion of the data resolution matrix for this inversion is shown in Figure C.10. Within the model space (at row/columns less that 176), clearly the data are well resolved. The decay in power, and thus the loss of the diagonal form, begins abruptly at row/column 176 - the first point outside of the model space. The periodicity in the energy that remains beyond this limit is due to the periodicity in b(t). Examination of the data resolution matrix reveals that, given the rapid decay of b(t), it is not possible to predict stationary data
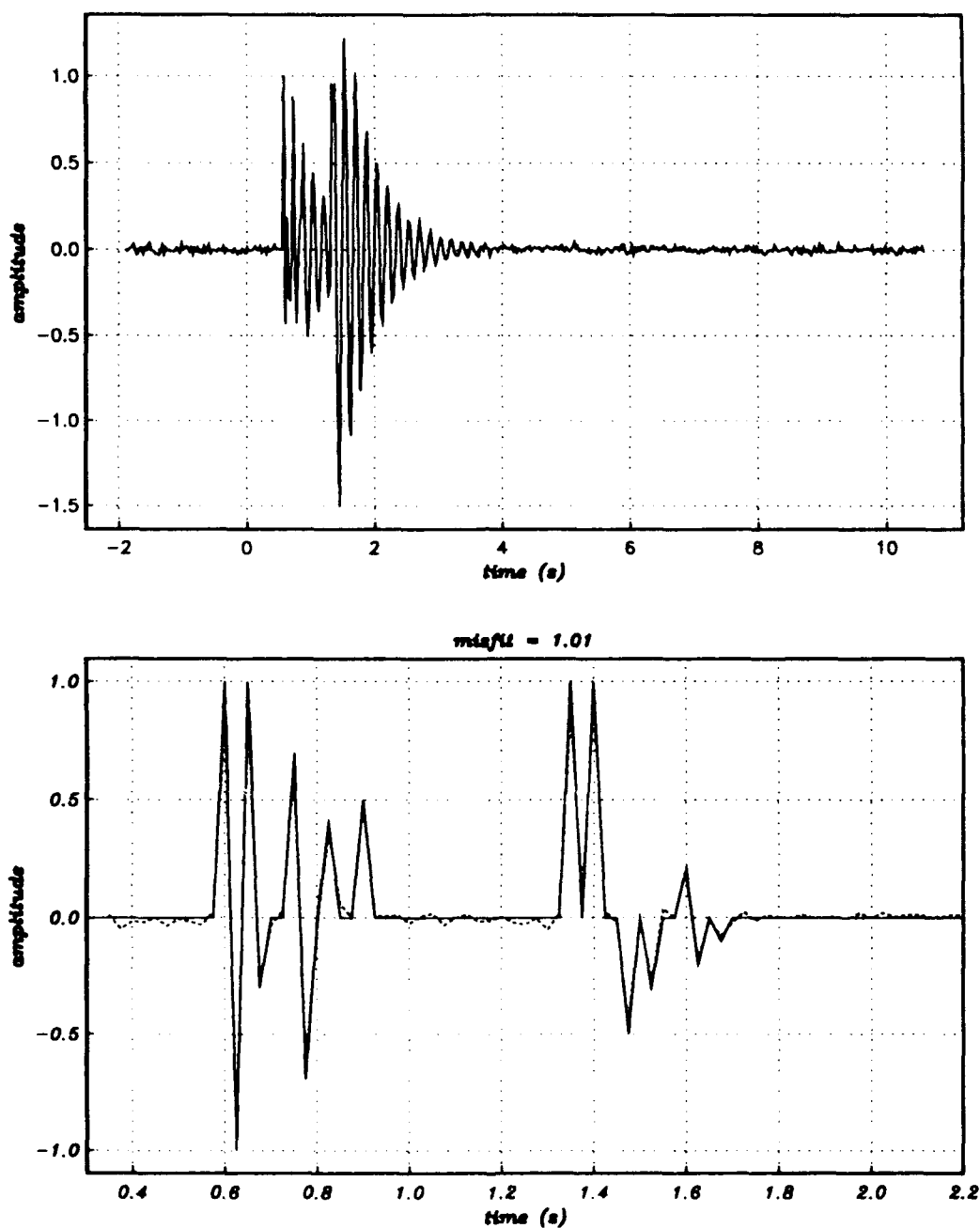
72

**Figure 3.13** The upper figure illustrates a synthetic time series that has resulted from the convolution of 15 delta functions with the wavelet introduced in Figure C.6). Uncorrelated, Gaussian, noise ($\sigma$=0.0002) has been added. The magnitudes and locations of the delta functions are revealed by the solid line in the lower figure. The dashed line represents the model that produces an rms data misfit of 1.0.
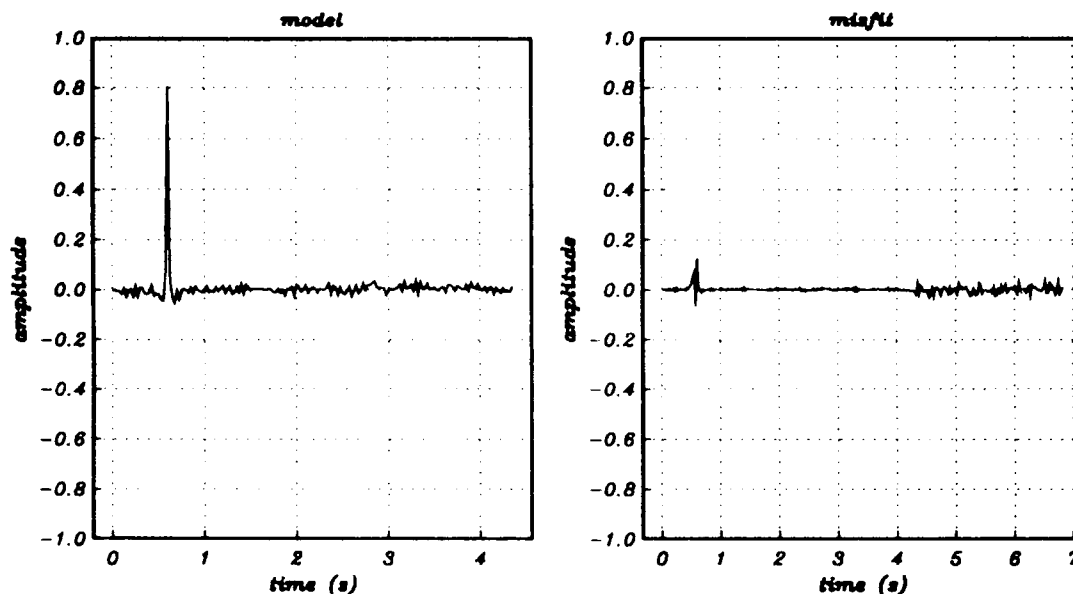
Figure 3.14 The left figure illustrates the model that yields an rms data misfit of 1.0 when the wavelet (Figure C.6) is deconvolved from the time series displayed in Figure C.7 after adding noise to the wavelet ($\frac{1}{5}$ the amplitude of the noise in the data). The misfit is illustrated in the right-hand figure. This figure is included to illustrate what impact error in the estimation of the wavelet has on the inversion.

outside the model space. In short, the noise is generated as a stationary process, not via a convolution, and so this deconvolution procedure is not able to duplicate it - there is an edge effect made noticeable because of the rapid decay of the minimum phase wavelet. A graphic description of the impact of the unevenly distributed data residuals on the chosen model is given by trade-off curves. In the upper half of Figure C.11 is displayed the trade-off relationship between the Lagrange multiplier, $\mu$, and the data misfit. The three curves in this figure were computed by considering misfit over the full data space (circles), the model space (triangles) and the portion of the model space from 1.0 to 4.0 s (squares). The solid horizontal line in both figures represents the desired misfit. Considering either misfit over the model space, or the data space, we select the model when $\mu$ reaches a value of 3, since at this point the misfit has reached the desired level. The vertical gap between the misfit associated with this model and the misfit occurring from 1.0 to 3.0 s (the bulk of the model) illustrates the extent to which overfitting is occurring in the bulk of the model space. Considering only the misfit occurring in the model space, with the exception of the large values near t=0.6 s, the normalized misfit is roughly 0.29 - a significant overfitting is occurring. To a large extent, the overfitting that occurs in most of the model space compensates for the underfitting that occurs near the delta function at 0.6 s. The algorithm has trouble fitting the delta
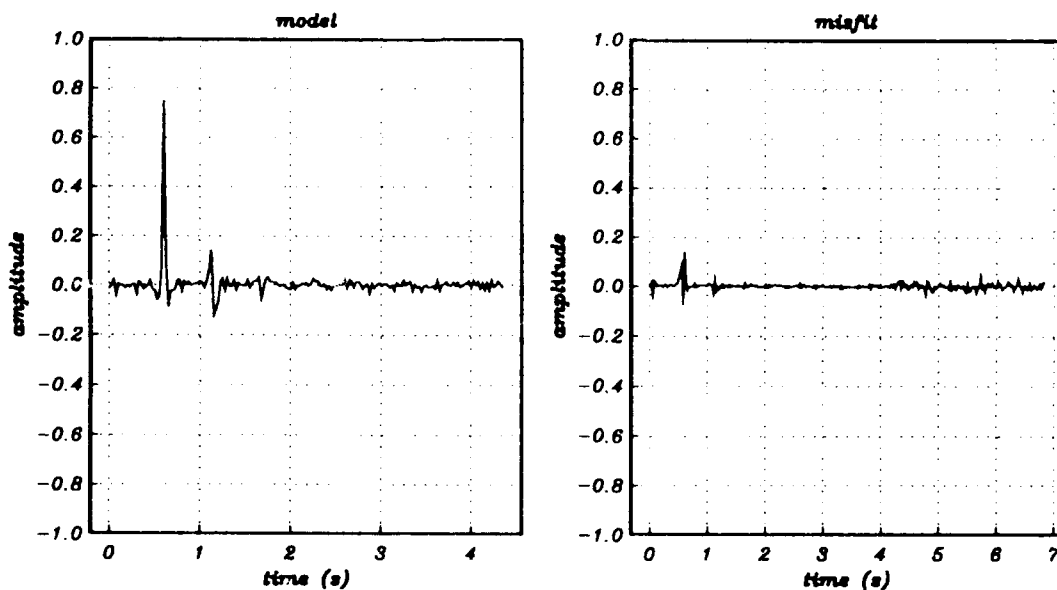
**Figure 3.15** The left figure illustrates the model that yields an rms data misfit of 1.0 when the wavelet (Figure C.6) is deconvolved from the time series displayed in Figure C.7 after truncating the wavelet after 20 points (0.5 s). The misfit is illustrated in the right-hand figure. This figure is included to illustrate what impact truncation of the true wavelet has on the inversion. Not surprisingly, the most significant corruption occurs at 1.1 s (0.5 s after the delta function).
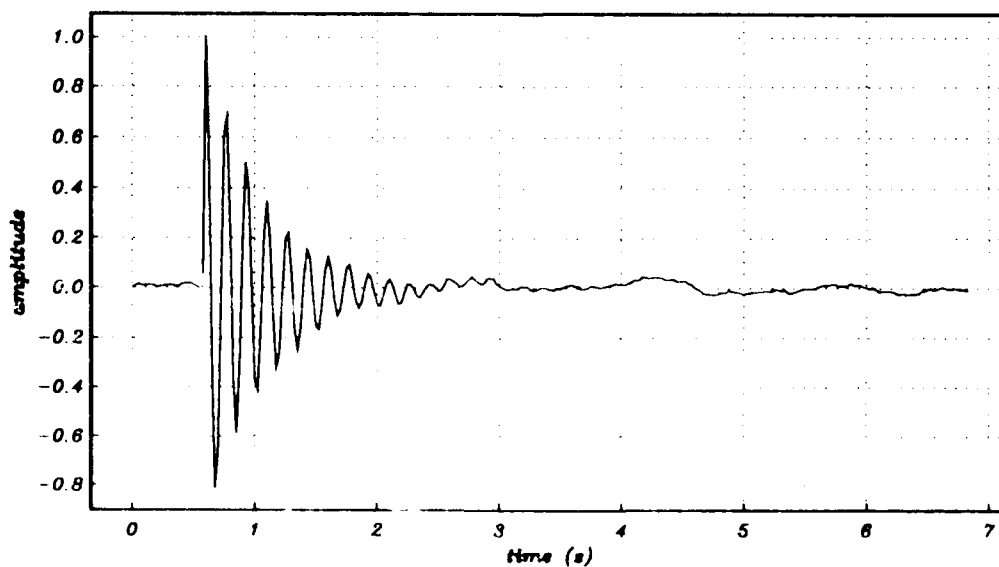


**Figure 3.16** A synthetic time series produced by convolving a delta function (at t=0.6 s) with the wavelet displayed in Figure C.6. Correlated, Gaussian, noise has been produced by convolving uncorrelated noise with a boxcar function.

function and thus overfits other model points to compensate. In the lower figure, we display the trade-off between data misfit and model size. The horizontal axis scale has been magnified by a factor of 14.4 to allow examination of detail. As a result of this, the preferred model appears further from the bend in the trade-off curves than it actually is. The selected model has a norm of roughly 0.65 - the input model is known to have a norm of 1.0. This discrepancy is mainly due to the underprediction of the delta function amplitude.

A second test, using the same input model but adding noise with 10 times the variance ($\sigma^2 = .002$) yields the output model and data misfits pictured in Figure C.12. This noise level is roughly equivalent to the worst level encountered in the Scripps' archive of 105 NORESS teleseismic recordings. In this noise environment, at a misfit of 1.01, the delta function is still located in the correct place; however, its amplitude is judged to be only 0.4 the true amplitude. The sidelobes have increased in amplitude, noise is still being fit into the model, and overfitting is occurring only in the model space.

In Figure C.13 we illustrate the degree to which the inversion algorithm is able to find a set of 15 delta functions convolved with the minimum phase wavelet (Figure C.6) when the result is added to a low level of noise ($\sigma = 0.0002$). The input data are illustrated in the upper half of the figure, the result is displayed in the lower half. It appears that, given a low noise environment, the approach is able to uncover a large number of delta functions when they are convolved with a minimum phase wavelet. To test the resistance of the inversion schemes to imperfect estimation of the wavelet, b(t), we have added uncorrelated Gaussian noise (at one-fifth the amplitude present in the data) to the wavelet. This relative amplitude has been chosen to simulate the relative error expected in the NORESS data set. In all other respects, we have duplicated the first inversion (i.e., we assume the wavelet is free of error). Visual comparison of the result (Figure C.14) with the original inversion (Figures C.7 to C.11) reveals little degradation of model quality.

In Figure C.15 we truncate the wavelet after 20 points (0.5 s). As expected, large "truncation phases" and residuals have resulted at multiples of 0.5 s after the model power. This test represents a severe truncation - as will be seen later, recorded teleseismic amplitudes generally decrease rapidly enough so that power levels at the end of the window are low.

The problems noted above may be due, in part, to the adoption of the $L_2$ norm and the underlying assumption of Gaussian statistics. Methods B and C are clearly not very tolerant of (or resistant to) outliers. The challenge of recovering the input model is increased when the model and data error possess similar covariances (in these datasets they are both uncorrelated). Fortunately, it is extremely unlikely that the recorded data will be so "long tailed" or that the model and error statistics
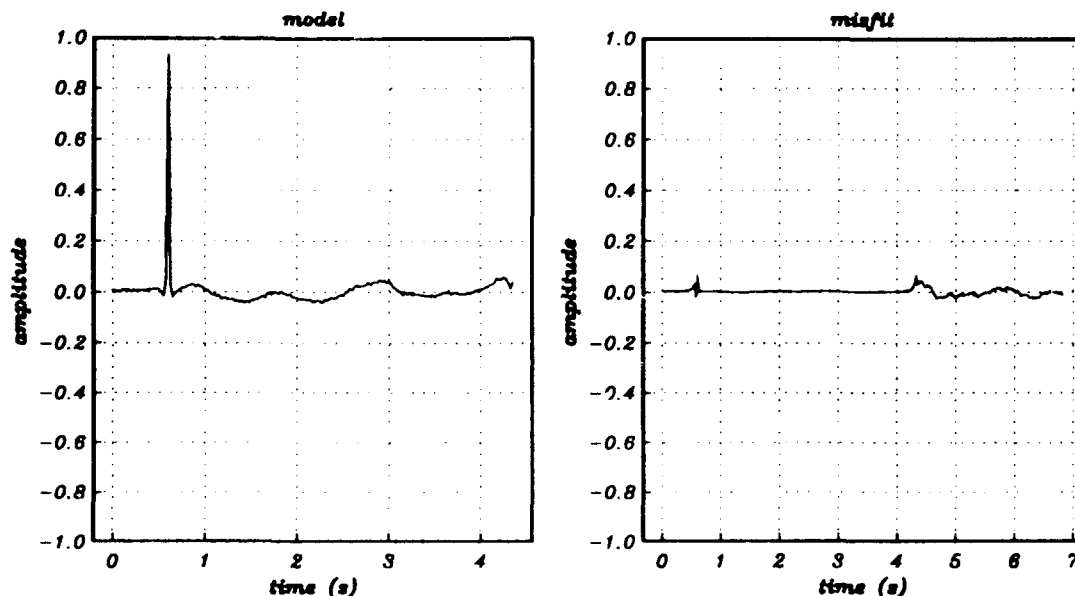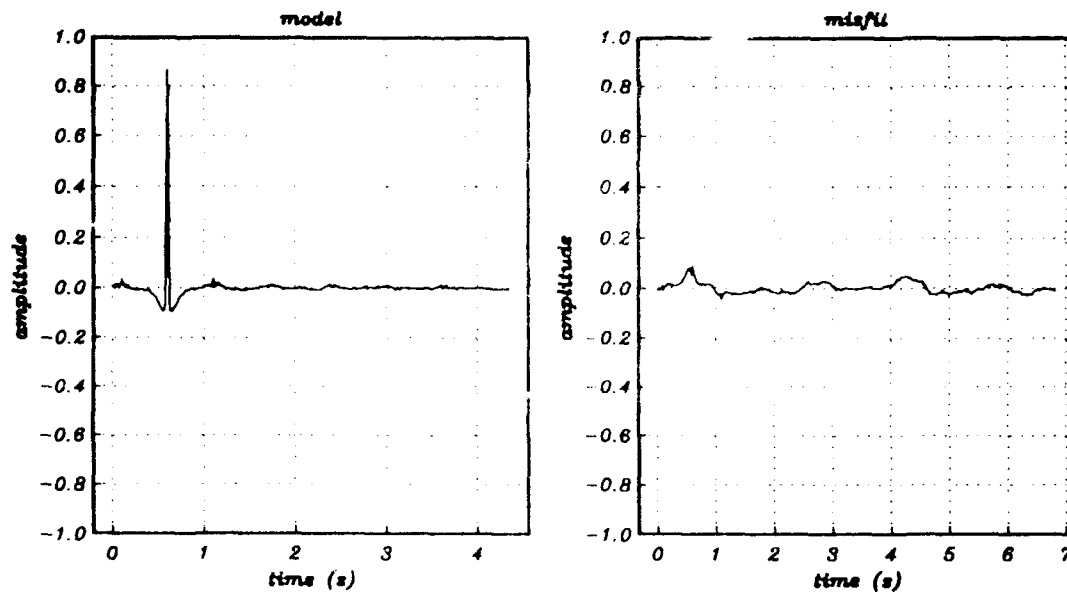
Figure 3.17 The left figure illustrates the model that yields an rms data misfit of 1.0 when the wavelet (Figure C.6) is deconvolved from the time series displayed in the preceding figure. The noise was assumed to be uncorrelated and, as a result, a significant amount of the correlated noise has been introduced into the model.

will be so well matched.

## C.4.b Correlated noise

In this subsection, we consider a time series produced by convolving the minimum phase wavelet with a single delta function (at 0.6 s) with correlated noise added to the result (Figure C.16). The correlated noise was generated by convolving uncorrelated Gaussian noise with a boxcar function. In Figure C.17 we present the preferred model that resulted from using methods B or C and assuming the noise is uncorrelated. This poor result suffers mainly because the correlated noise has been fit into the model - the algorithm expected the noise to be uncorrelated and thus put this correlated energy in the model. In the next figure (C.18) we have included the covariance matrix estimated for the noise using Equation C.19 and have re-inverted for the model. Although the delta function has acquired significant side lobes, the rest of the model is relatively free of noise - the residuals are well distributed.

## C.4.c Correlated model

In this subsection, we consider a more physically reasonable model - a correlated transient

77

**Figure 3.18** The left figure illustrates the model that yields an rms data misfit of 1.0 when the wavelet (Figure C.6) is deconvolved from the time series displayed in the preceding figure. The true noise covariance matrix ($C_{nn}$) was included in the inversion causing most of the noise to be excluded from the model.
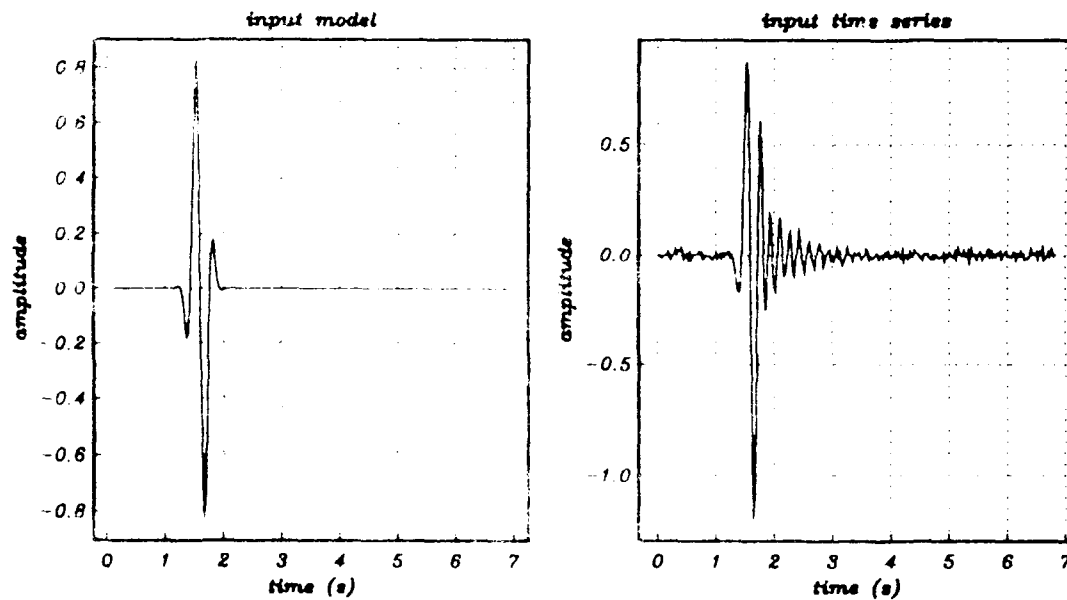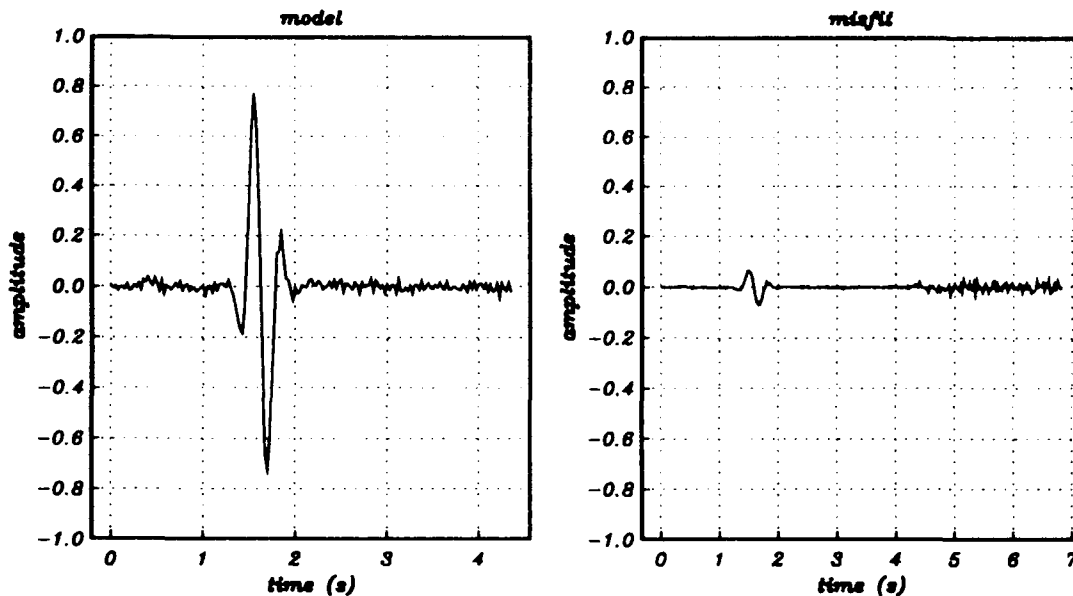


**Figure 3.19** To produce the synthetic time series (right figure) the transient, correlated model (left figure) is convolved with the minimum phase wavelet displayed in Figure C.6. Uncorrelated, Gaussian, noise ($\sigma = 0.0002$) has been added.

displayed on the left side of Figure C.19. To produce the input data (right side of Figure C.19) uncorrelated

**Figure 3.20** The left figure illustrates the model that yields an rms data misfit of 1.0 when the wavelet (Figure C.6) is deconvolved from the time series displayed in the preceding figure. The model was assumed to be uncorrelated. As a result, the data misfit (right figure) is concentrated at the location of the model-power.
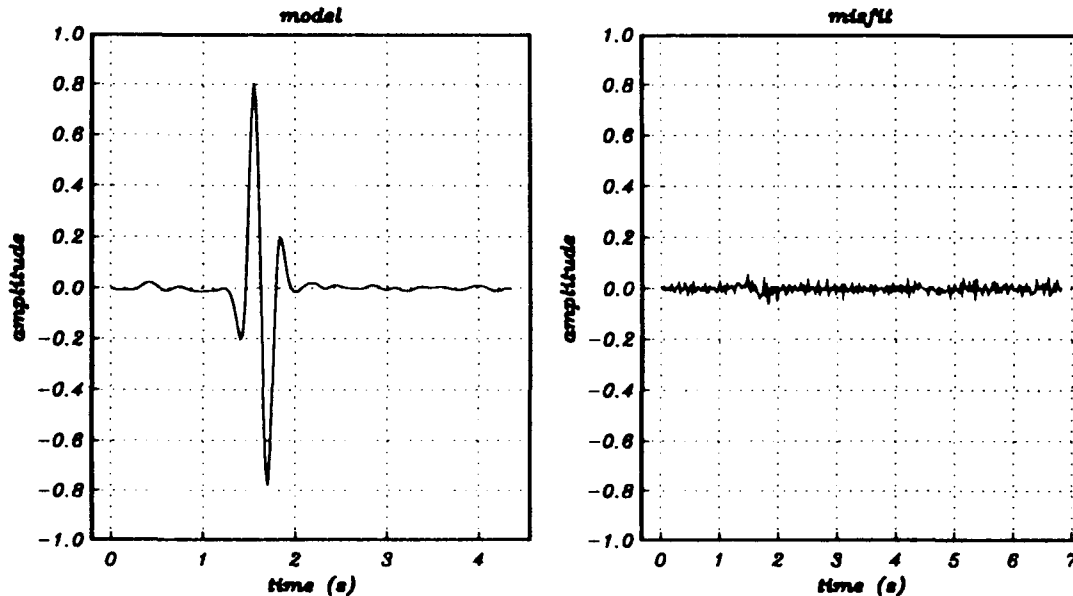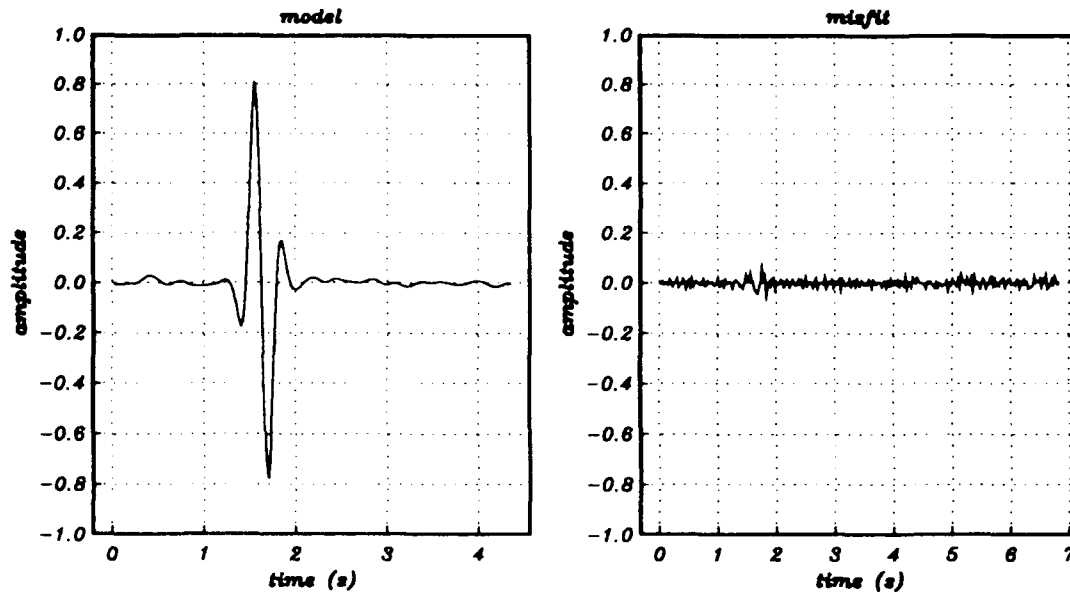


**Figure 3.21** The left figure illustrates the model that yields an rms data misfit of 1.0 when the wavelet (Figure C.6) is deconvolved from the time series displayed in Figure C.19. The Toeplitz correlation matrix ($C_{mm}$), estimated by applying an autocorrelation operator to the known model, has been used in the inversion. The data residuals (right figure) are well (evenly) distributed.

**Figure 3.22** The left figure illustrates the model that yields an rms data misfit of 1.0 when the wavelet (Figure C.6) is deconvolved from the time series displayed in Figure C.19. The Toeplitz correlation matrix ($C_{mm}$), estimated by applying an autocorrelation operator to the known model (and approximating the result with a Gaussian), has been used in the inversion. The data residuals (right figure) are well (evenly) distributed with the exception of a slight concentration of power at the vicinity of the model power.

noise ($\sigma = 0.0002$) has been added to the convolution of this transient with the minimum phase wavelet. In Figures C.20 to C.24 we present a series of inversions involving this data that were computed to test the relative worth of methods B and C. In Figure C.20 we use method C, the statistical approach, to invert for the underlying model; however, we assume that the model is uncorrelated. The model has not been resolved with great fidelity - it possesses some uncorrelated noise due to overfitting in the model space that compensates for the underfitting that has occurred at the location of the model power.

In Figure C.21 we attempt the same inversion; however, prior to the inversion we have applied the autocorrelation operator to the known model and included this information, within the correlation operator $C_{mm}$, as part of the inversion. Despite the slight concentration of power at roughly 0.6 s, the data residuals are extremely well distributed - the model power is not being underfitted. It appears that the statistical approach works well in spite of the transient nature of the model. To achieve the result displayed in Figure C.22 we approximate the true covariance matrix with a Gaussian, that provides roughly the same smoothing, and invert to find slightly worse residuals - the transient amplitudes are underpredicted. In Figures C.23 and C.24 we use method B and define the roughening matrix to be discrete first and second order differencing operators respectively. Both of these results are clearly inferior to those achieved using
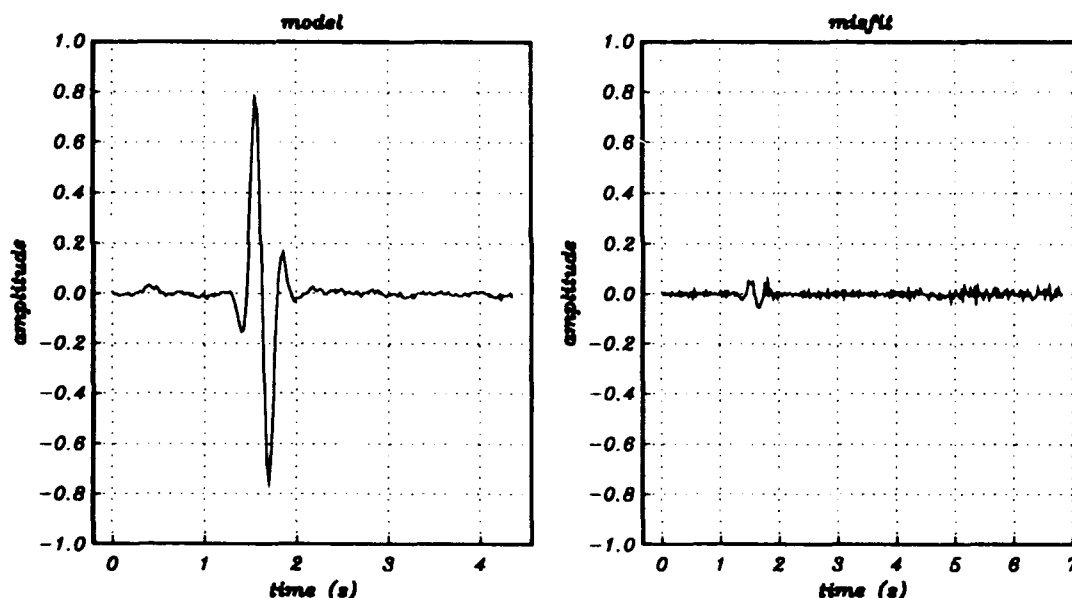
**model** **misfit**

**Figure 3.23** The left figure illustrates the model that yields an rms data misfit of 1.0 when the wavelet (Figure C.6) is deconvolved from the time series displayed in Figure C.19. The model has been solved for using equation C.21, a first-derivative roughening matrix was used. The data residuals possess a more marked concentration of power in the vicinity of the transient model power than is possessed in the previous two inversions. As a result, more noise has been fit into the model (note the "chatter" in the model (left figure) and the overfitting in the model space (right figure).

method C with the known correlation operator $C_{mm}$, but only slightly worse than the results achieved when $C_{mm}$ has been approximated with a Gaussian. In both of the inversions achieved using method B, the transient is not well predicted, compensatory overfitting is occurring in the model space, causing "chatter" in the model.

*C.4.d Deconvolution of full array recordings of synthetic and recorded events*

At this point, we return to the images presented in section C.2 to determine the extent to which we can use methods A and C to deconvolve the seismograms and recover the radial resolution in the images. Recall, from section C.2, that the image in Figure C.3 originated by convolving a Semipalatinsk teleseism ($b_s(t)$, pictured in Figure C.2) with the synthetics used to generate Figure C.1. In the same manner, Figure C.5 was generated from C.1 using the teleseismic earthquake beam ($b_e(t)$ pictured in Figure C.4).

In Figure C.25 we present the result of using method C to deconvolve the 25 channels underlying Figure C.3. We have added a small level of uncorrelated noise to each channel to stabilize the inversion.
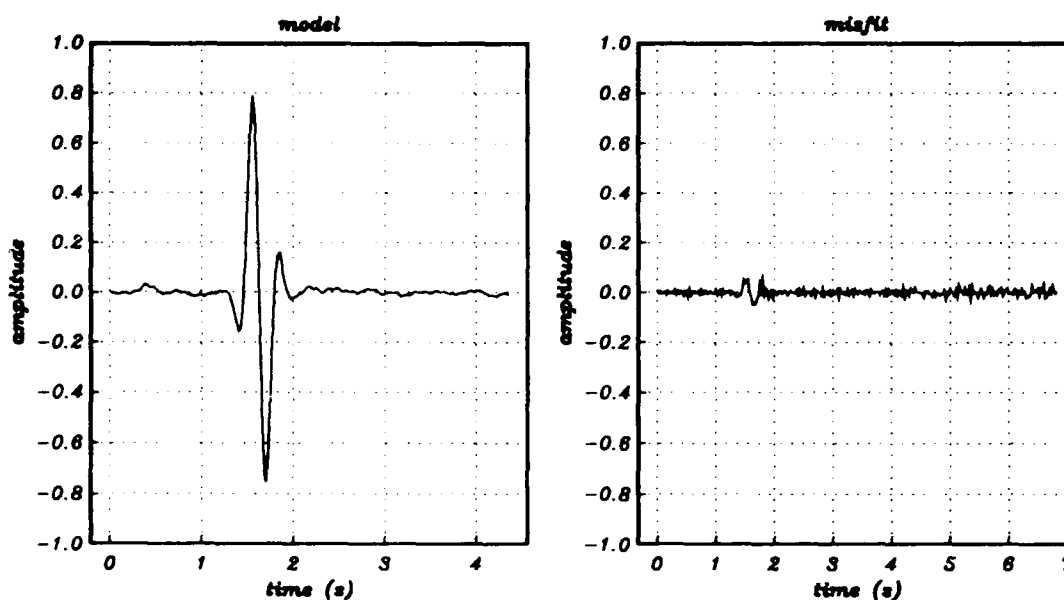
**Figure 3.24** The left figure illustrates the model that yields an rms data misfit of 1.0 when the wavelet (Figure C.6) is deconvolved from the time series displayed in Figure C.19. The model has been solved for using equation C.21, a second-derivative roughening matrix was used. As in the previous inversion, a significant underfitting of the data is occurring at the location of the model power. As a result, more noise has been fit into the model (note the "chatter" in the model (left figure) and the overfitting in the model space (right figure).

We use $b_s(t)$ with the exception that it has been truncated after 400 points (roughly 40 s) and tapered by a cosine taper from points 361 to 400. The data vector (799 points) has been tapered by a cosine er from points 401 to 799 to reduce edge effects. The model contains 400 points and spans 40 s. This combination of vector lengths was chosen to reduce edge effects - as seen earlier, any truncation error should occur $N_b$ points beyond the model power. Using the parlance introduced in section C.2, this approach has reduced the power of the tail by roughly 15 dB. The azimuthal resolution (width of the main lobe) has been recovered almost exactly and the image side lobes have been recovered to a similar extent. The deconvolved trace, station a0, is displayed below the image and bears a striking resemblance to the original channel displayed in Figure C.1. Fortunately, considering that this inversion required roughly 11 minutes of CPU time on the SDSC Cray Y-MP, it appears to have been a great success. In Figure C.26 we present the result of applying method A to deconvolve the same 25 time series. This result was achieved after several (roughly 10) iterations, where parameters (such as the water level) were chosen to yield a model estimate. The visual appearance of each intermediate model led to the selection of a new (we hope better) set of parameters, and so on. This result (Figure C.26) is inferior to the preceding one (Figure C.25) for several reasons. First, the ringing has led to a slight widening of the main lobe (in a
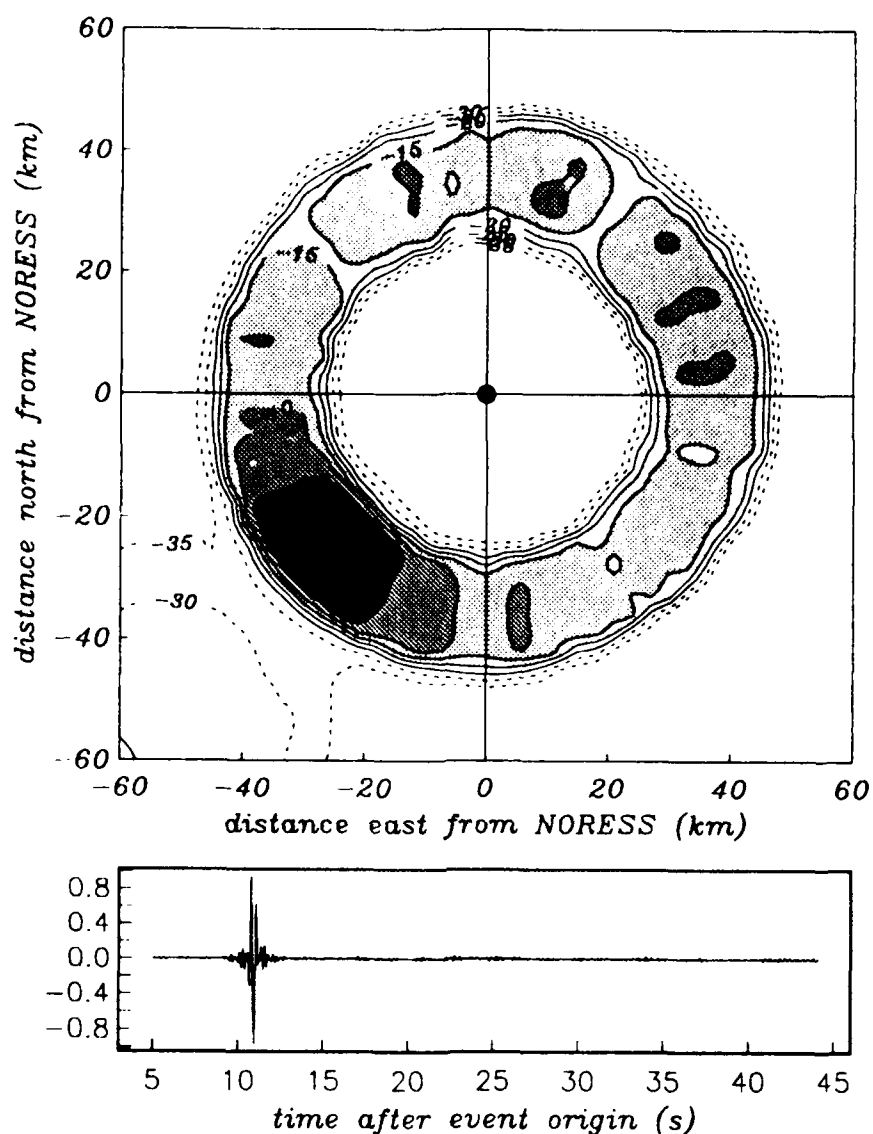
**Figure 3.25** The result of the deconvolution of the teleseism displayed in Figure C.2 from the seismograms represented by the trace in Figure C.3. Perfect deconvolution would result in this image being identical to that displayed in Figure C.1. Displayed in the lower figure is the deconvolved channel a0.

radial sense) and some loss of azimuthal resolution. The surface wave packet has been smoothed leading to a further reduction of azimuthal resolution. The character of the image "side lobes" has not been well recovered (see Figure C.1). The "tail" has been significantly reduced (by roughly 15dB). It is likely that a better result could be achieved after several more visual, and subjective, iterations; however, based on this disappointing result, we have chosen to abandon this approach.

The second test image (Figures C.4 and C.5) presents a greater challenge for method C since
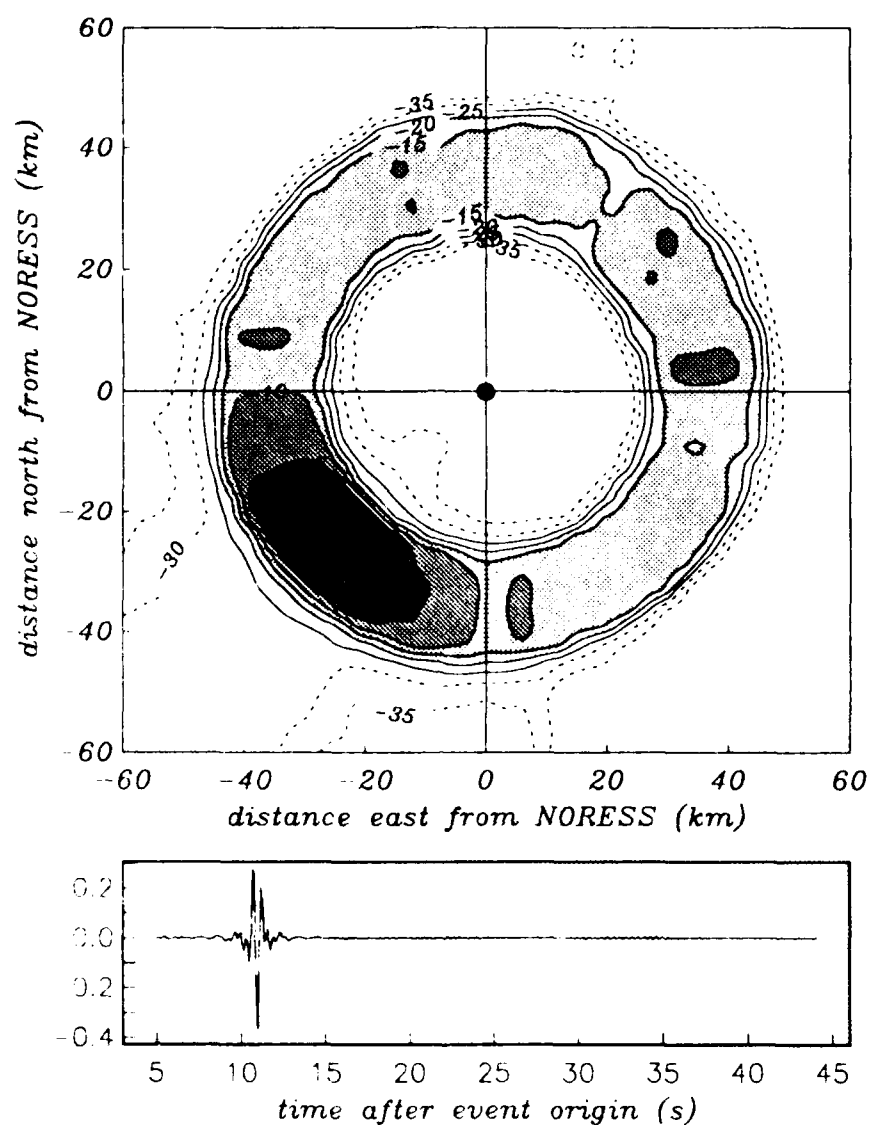
**Figure 3.26** The result of the deconvolution of the teleseism displayed in Figure C.2 from the seismograms represented by the trace in Figure C.3 using the spectral division technique. As in the previous figure, perfect deconvolution would result in this image being identical to that displayed in Figure C.1. Displayed in the lower figure is the deconvolved channel a0.

the wavelet is more protracted. Using method C we can reduce the tail by roughly 10 dB (Figure C.27).

There is a slight edge effect at the beginning of the deconvolved trace. The side lobe character has been recovered the azimuthal resolution has not been degraded.
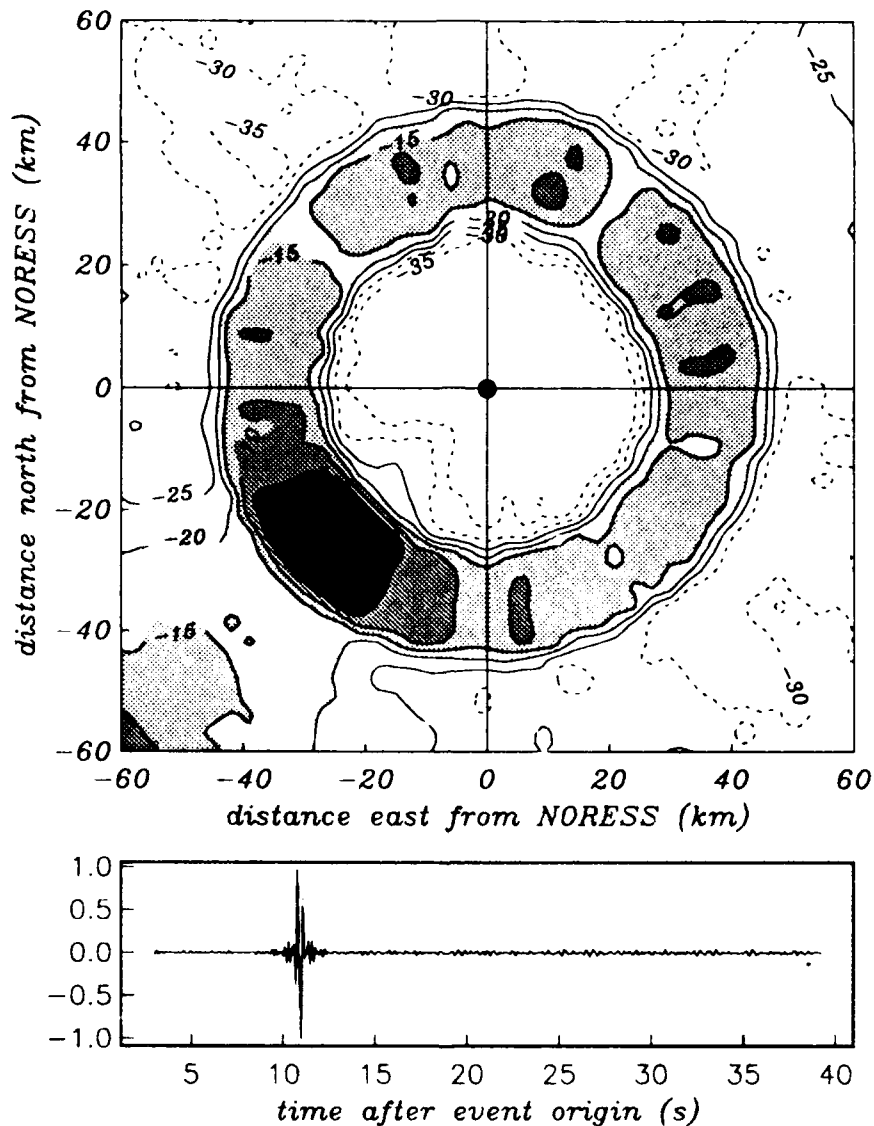
# C.5 Conclusions

**Figure 3.27** The result of the deconvolution of the teleseism displayed in Figure C.4 from the seismograms represented by the trace in Figure C.5. As in the previous two figures, perfect deconvoluuon would result in this image being identical to that displayed in Figure C.1. Displayed in the lower figure is the deconvolved channel a0.

In this chapter, three approaches to the seismic deconvolution problem have been considered. The first, method A, is a straightforward spectral division technique that uses pre-whitening. The second, method B, is akin to the Occam's Razor approach of Constable, *et al.*(1987). The third technique, developed in this chapter, is essentially the stochastic inversion scheme of Franklin (1970) and allows the introduction of *a priori* information regarding noise and model covariances, into the inversion process. These approaches have been applied, with varying degrees of success, to several synthetic data~ts. The

spectral division technique has been found to be inferior, primarily because of its *ad hoc*, highly subjective nature.

It has become clear from the analysis of synthetic data that the measure by which techniques can best be judged is the manner in which the data misfits are distributed. The most succesful techniques yield evenly distributed residuals. Using this yardstick to judge success, methods B and C are equally capable of inverting data when the model is uncorrelated. Application of these techniques to models which possess significant outliers generally yields unsatisfactory results. This is most likely true because these techniques use the $L_2$ norm to assess model size and thus assume the model is a realization of a Gaussian process. The problem seems particularly acute when the model and noise possess similar covariances - it is not clear where the energy in the data should be placed - much noise is assumed to be part of the model. Given accurate *a priori* information, it appears that method C, the statistical approach, is capable of the best results, or the most evenly distributed residuals, when the input model is a correlated transient pulse - the most physically reasonable model considering that we are most interested in deconvolving seismic records for surface wave packets produced by scatterers. This is true even when a Gaussian Toeplitz operator is substituted for the model covariance matrix.

Analysis of synthetic images created by applying the migration technique (Chapter 2) to data constructed by convolving full array "recordings" of synthetic scattered wavefields with real teleseisms reveals that method C is capable of significantly enhancing the temporal resolution of the time series and thus the radial resolution of the images.

## C.6 Acknowledgments

# References

Backus, G.E. and Gilbert, J.F., Numerical applications of a formalism for geophysical inverse problems. *Geophys. J. R. astr. Soc.*, **13**, 247-276, 1967.

Backus, G.E. and Gilbert, J.F., The resolving power of gross earth data. *Geophys. J. R. astr. Soc.*, **16**, 169-205, 1968.

Backus, G.E. and Gilbert, J.F., Uniqueness in the inversion of inaccurate gross earth data. *Phil. Trans. Roy. Soc. London Ser. A*, **266**, 123-192, 1973.

Constable, S.C., Parker, R.L. and Constable, C.G., Occam's inversion: A practical algorithm for generating smooth models from electromagnetic sounding data. *Geophysics*, **52**, 289-300, 1987.

Frankel, A. and Wennerberg, L., Energy-flux model of seismic coda: separation of scattering and intrinsic attenuation. *Bull. Seismol. Soc. Am.*, **77**, 1223-1251, 1987.

Franklin, J.N., Well-posed stochastic extensions of ill-posed linear problems. *Journal of mathematical analysis and applications*, **31**, 682-716, 1970.

Fyen, J., NORSAR semiannual technical summary - 2-85/86. *48-59*, 1986.

Hedlin, M.A.H. and Orcutt, J.A., A comparative study of island, seafloor and sub-seafloor ambient noise levels. *Bull. Seismol. Soc. Am.*, **79**, 172-179, 1989.

Husebye, E.S., Ingate, S.F. and Thoresen, E., *The Vela Program, a twenty five year review of basic research - Ann U. Kerr, editor.* Defense Advanced Research Projects Agency, Seismic arrays for everyone.

Journel, A.G., Fundamentals of Geostatistics in Five Lessons. *Short Course in Geology presented at the 28th International Geological Congress in Washington, D.C.*, **8**, 1-40, 1989.

Lacoss, R.T., Review of some techniques for array processing. *Exploitation of seismograph networks, K.G. Beauchamp - editor*, 1975.

Mendel, J.M., *Optimal seismic deconvolution, an estimation based approach.* Academic Press, Inc., 1983.

Menke, W., *Geophysical data analysis: discrete inverse theory.* Academic Press, Inc., 1984.

Oldenburg, D.W., A comprehensive solution to the linear deconvolution problem. *Geophys. J. R. astr. Soc.*, **65**, 331-357, 1981.

Parker, R.L., Understanding inverse theory. *Ann. Rev. Earth Planet. Sci.*, **5**, 35-64, 1977.

Priestley, M.B., *Spectral analysis and time series.* Academic Press, Inc., 1981.

Shaw, P.R. and Orcutt, J.A., Waveform inversion of seismic reflection data and applications to young Pacific crust. *Geophys. J. R. astr. Soc.*, **82**, 375-414, 1985.

Tarantola, A., *Essai d'une approche generale du probleme inverse.* Ph.D. thesis submitted to l'Universite Pierre et Marie Curie, 1981.

Tarantola, A. and Valette, B., Generalized nonlinear inverse problems solved using the least squares criterion. *Rev. Geophys. Space Phys.*, **20**, 219-232, 1982.

Treitel, S. and Robinson, E.A., The design of high-resolution digital filters. *IEEE transactions on geoscience electronics*, **GE-4**, 25-39, 1966.

Yilmaz, O., *Seismic data processing*. Society of Exploration Geophysicists, investigations in geophysics, volume 2, 1987.

Prof. Thomas Ahrens
Seismological Lab, 252-21
Division of Geological & Planetary Sciences
California Institute of Technology
Pasadena, CA 91125

Prof. Keiiti Aki
• Center for Earth Sciences
University of Southern California
University Park
, Los Angeles, CA 90089-0741

Prof. Shelton Alexander
Geosciences Department
403 Deike Building
The Pennsylvania State University
University Park, PA 16802

Dr. Ralph Alewine, III
DARPA/NMRO
3701 North Fairfax Drive
Arlington, VA 22203-1714

Prof. Charles B. Archambeau
CIRES
University of Colorado
Boulder, CO 80309

Dr. Thomas C. Bache, Jr.
Science Applications Int'l Corp.
10260 Campus Point Drive
San Diego, CA 92121 (2 copies)

Prof. Muawia Barazangi
Institute for the Study of the Continent
Cornell University
Ithaca, NY 14853

Dr. Jeff Barker
Department of Geological Sciences
State University of New York
 at Binghamton
Vestal, NY 13901

Dr. Douglas R. Baumgardt
ENSCO, Inc
5400 Port Royal Road
Springfield, VA 22151-2388

Dr. Susan Beck
Department of Geosciences
Building #77
University of Arizona
Tuscon, AZ 85721

Dr. T.J. Bennett
S-CUBED
A Division of Maxwell Laboratories
11800 Sunrise Valley Drive, Suite 1450
Reston, VA 22091

Dr. Robert Blandford
AFTAC/TT, Center for Seismic Studies
1330 North 17th Street
Suite 1450
Arlington, VA 22209-2308

Dr. G.A. Bollinger
Department of Geological Sciences
Virginia Polytechnical Institute
21044 Derring Hall
Blacksburg, VA 24061

Dr. Stephen Bratt
Center for Seismic Studies
1300 North 17th Street
Suite 1450
Arlington, VA 22209-2308

Dr. Lawrence Burdick
Woodward-Clyde Consultants
566 El Dorado Street
Pasadena, CA 91109-3245

Dr. Robert Burridge
Schlumberger-Doll Research Center
Old Quarry Road
Ridgefield, CT 06877

Dr. Jerry Carter
Center for Seismic Studies
1300 North 17th Street
Suite 1450
Arlington, VA 22209-2308

Eric Chael
Division 9241
Sandia Laboratory
Albuquerque, NM 87185

Prof. Vernon F. Cormier
Department of Geology & Geophysics
U-45, Room 207
University of Connecticut
Storrs, CT 06268

Prof. Anton Dainty
Earth Resources Laboratory
Massachusetts Institute of Technology
42 Carleton Street
Cambridge, MA 02142

Prof. Steven Day
Department of Geological Sciences
San Diego State University
San Diego, CA 92182

Art Frankel
U.S. Geological Survey
922 National Center
Reston, VA 22092

Marvin Denny
U.S. Department of Energy
Office of Arms Control
Washington, DC 20585

Dr. Cliff Frolich
Institute of Geophysics
8701 North Mopac
Austin, TX 78759

Dr. Zoltan Der
ENSCO, Inc.
5400 Port Royal Road
Springfield, VA 22151-2388

Dr. Holly Given
IGPP, A-025
Scripps Institute of Oceanography
University of California, San Diego
La Jolla, CA 92093

Prof. Adam Dziewonski
Hoffman Laboratory, Harvard University
Dept. of Earth Atmos. & Planetary Sciences
20 Oxford Street
Cambridge, MA 02138

Dr. Jeffrey W. Given
SAIC
10260 Campus Point Drive
San Diego, CA 92121

Prof. John Ebel
Department of Geology & Geophysics
Boston College
Chestnut Hill, MA 02167

Dr. Dale Glover
Defense Intelligence Agency
ATTN: ODT-1B
Washington, DC 20301

Eric Fielding
SNEE Hall
INSTOC
Cornell University
Ithaca, NY 14853

Dr. Indra Gupta
Teledyne Geotech
314 Montgomery Street
Alexanderia, VA 22314

Dr. Mark D. Fisk
Mission Research Corporation
735 State Street
P.O. Drawer 719
Santa Barbara, CA 93102

Dan N. Hagedon
Pacific Northwest Laboratories
Battelle Boulevard
Richland, WA 99352

Prof Stanley Flatte
Applied Sciences Building
University of California, Santa Cruz
Santa Cruz, CA95064

Dr. James Hannon
Lawrence Livermore National Laboratory
P.O. Box 808
L-205
Livermore, CA 94550

Dr. John Foley
NER-Geo Sciences
1100 Crown Colony Drive
Quincy, MA 02169

Dr. Roger Hansen
AFTAC/TTR
Patrick AFB, FL 32925

Prof. Donald Forsyth
Department of Geological Sciences
Brown University
Providence, RI 02912

Prof. David G. Harkrider
Seismological Laboratory
Division of Geological & Planetary Sciences
California Institute of Technology
Pasadena, CA 91125

Prof. Danny Harvey
CIRES
University of Colorado
Boulder, CO 80309

Prof. Donald V. Helmberger
• Seismological Laboratory
Division of Geological & Planetary Sciences
California Institute of Technology
, Pasadena, CA 91125

Prof. Eugene Herrin
Institute for the Study of Earth and Man
Geophysical Laboratory
Southern Methodist University
Dallas, TX 75275

Prof. Robert B. Herrmann
Department of Earth & Atmospheric Sciences
St. Louis University
St. Louis, MO 63156

Prof. Lane R. Johnson
Seismographic Station
University of California
Berkeley, CA 94720

Prof. Thomas H. Jordan
Department of Earth, Atmospheric &
   Planetary Sciences
Massachusetts Institute of Technology
Cambridge, MA 02139

Prof. Alan Kafka
Department of Geology & Geophysics
Boston College
Chestnut Hill, MA 02167

Robert C. Kemerait
ENSCO, Inc.
445 Pineda Court
Melbourne, FL 32940

Dr. Max Koontz
U.S. Dept. of Energy/DP 5
Forrestal Building
1000 Independence Avenue
Washington, DC 20585

Dr. Richard LaCoss
MIT Lincoln Laboratory, M-200B
P.O. Box 73
Lexington, MA 02173-0073

Dr. Fred K. Lamb
University of Illinois at Urbana-Champaign
Department of Physics
1110 West Green Street
Urbana, IL 61801

Prof. Charles A. Langston
Geosciences Department
403 Deike Building
The Pennsylvania State University
University Park, PA 16802

Prof. Thorne Lay
Institute of Tectonics
Earth Science Board
University of California, Santa Cruz
Santa Cruz, CA 95064

Dr. William Leith
U.S. Geological Survey
Mail Stop 928
Reston, VA 22092

James F. Lewkowicz
Phillips Laboratory/GPEH
Hanscom AFB, MA 01731-5000

Mr. Alfred Lieberman
ACDA/VI-OA State Department Building
Room 5726
320-21st Street, NW
Washington, DC 20451

Prof. L. Timothy Long
School of Geophysical Sciences
Georgia Institute of Technology
Atlanta, GA 30332

Dr. Robert Masse
Denver Federal Building
Bos 25046, Mail Stop 967
Denver, CO 80225

Dr. Randolph Martin, III
New England Research, Inc.
76 Olcott Drive
White River Junction, VT 05001

Dr. Gary McCartor
Department of Physics
Southern Methodist University
Dallas, TX 75275

3

Dr. Richard Sailor
TASC, Inc.
55 Walkers Brook Drive
Reading, MA 01867

Prof. Charles G. Sammis
Center for Earth Sciences
University of Southern California
University Park
Los Angeles, CA 90089-0741

Prof. Christopher H. Scholz
Lamont-Doherty Geological Observatory
of Columbia University
Palisades, CA 10964

Dr. Susan Schwartz
Institute of Tectonics
1156 High Street
Santa Cruz, CA 95064

Secretary of the Air Force
(SAFRD)
Washington, DC 20330

Office of the Secretary of Defense
DDR&E
Washington, DC 20330

Thomas J. Sereno, Jr.
Science Application Int'l Corp.
10260 Campus Point Drive
San Diego, CA 92121

Dr. Michael Shore
Defense Nuclear Agency/SPSS
6801 Telegraph Road
Alexandria, VA 22310

Dr. Matthew Sibol
Virginia Tech
Seismological Observatory
4044 Derring Hall
Blacksburg, VA 24061-0420

Prof. David G. Simpson
IRIS, Inc.
1616 North Fort Myer Drive
Suite 1400
Arlington, VA 22209

Donald L. Springer
Lawrence Livermore National Laboratory
L-025
P.O. Box 808
Livermore, CA 94550

Dr. Jeffrey Stevens
S-CUBED
A Division of Maxwell Laboratory
P.O. Box 1620
La Jolla, CA 92038-1620

Lt. Col. Jim Stobie
ATTN: AFOSR/NL
Bolling AFB
Washington, DC 20332-6448

Prof. Brian Stump
Institute for the Study of Earth & Man
Geophysical Laboratory
Southern Methodist University
Dallas, TX 75275

Prof. Jeremiah Sullivan
University of Illinois at Urbana-Champaign
Department of Physics
1110 West Green Street
Urbana, IL 61801

Prof. L. Sykes
Lamont-Doherty Geological Observatory
of Columbia University
Palisades, NY 10964

Dr. David Taylor
ENSCO, Inc.
445 Pineda Court
Melbourne, FL 32940

Dr. Steven R. Taylor
Los Alamos National Laboratory
P.O. Box 1663
Mail Stop C335
Los Alamos, NM 87545

Prof. Clifford Thurber
University of Wisconsin-Madison
Department of Geology & Geophysics
1215 West Dayton Street
Madison, WS 53706

Prof. M. Nafi Toksoz
Earth Resources Lab
Massachusetts Institute of Technology
42 Carleton Street
Cambridge, MA 02142

5

Dr. Larry Turnbull
CIA-OSWR/NED
Washington, DC  20505

DARPA/RMO/SECURITY OFFICE
3701 North Fairfax Drive
Arlington, VA  2203-1714

Dr. Gregory van der Vink
IRIS, Inc.
16116 North Fort Myer Drive
Suite 1440
Arlington, VA  22209

HQ DNA
ATTN:  Technical Library
Washington, DC  20305

Dr. Karl Veith
EG&G
5211 Auth Road
Suite 240
Suitland, MD  20746

Defense Intelligence Agency
Directorate for Scientific &  Technical Intelligence
ATTN:  DTIB
Washington, DC  20340-6158

Prof. Terry C. Wallace
Department of Geosciences
Building #77
University of Arizona
Tuscon, AZ  85721

Defense Technical Information Center
Cameron Station
Alexandria, VA  22314 (5 Copies)

Dr. Thomas Weaver
Los Alamos National Laboratory
P.O. Box 1663
Mail Stop C335
Los Alamos, NM  87545

TACTEC
Battelle Memorial Institute
505 King Avenue
Columbus, OH  43201 (Final Report)

Dr. William Wortman
Mission Research Corporation
8560 Cinderbed Road
Suite 700
Newington, VA  22122

Phillips Laboratory
ATTN:  XPG
Hanscom AFB, MA  01731-5000

Prof. Francis T. Wu
Department of Geological Sciences
State University of New York
 at Binghamton
Vestal, NY  13901

Phillips Laboratory
ATTN:  GPE
Hanscom AFB, MA  01731-5000

AFTAC/CA
(STINFO)
Patrick AFB, FL  32925-6001

Dr. Michel Bouchon
I.R.I.G.M.-B.P. 68
38402 St. Martin D'Heres
Cedex, FRANCE

DARPA/PM
3701 North Fairfax Drive
Arlington, VA  22203-1714

Dr. Michel Campillo
Observatoire de Grenoble
I.R.I.G.M.-B.P. 53
38041 Grenoble, FRANCE

DARPA/RMO/RETRIEVAL
3701 North Fairfax Drive
Arlington, VA  22203-1714

Dr. Kin Yip Chun
Geophysics Division
Physics Department
University of Toronto
Ontario, CANADA

Prof. Hans-Peter Harjes
Institute for Geophysics
Ruhr University/Bochum
P.O. Box 102148
4630 Bochum 1, GERMANY

Prof. Eystein Husebye
• NTNF/NORSAR
P.O. Box 51
N-2007 Kjeller, NORWAY

David Jepsen
Acting Head, Nuclear Monitoring Section
Bureau of Mineral Resources
Geology and Geophysics
G.P.O. Box 378, Canberra, AUSTRALIA

Ms. Eva Johannisson
Senior Research Officer
National Defense Research Inst.
P.O. Box 27322
S-102 54 Stockholm, SWEDEN

Dr. Peter Marshall
Procurement Executive
Ministry of Defense
Blacknest, Brimpton
Reading FG7-FRS, UNITED KINGDOM

Dr. Bernard Massinon, Dr. Pierre Mechler
Societe Radiomana
27 rue Claude Bernard
75005 Paris, FRANCE (2 Copies)

Dr. Svein Mykkeltveit
NTNT/NORSAR
P.O. Box 51
N-2007 Kjeller, NORWAY (3 Copies)

Prof. Keith Priestley
University of Cambridge
Bullard Labs, Dept. of Earth Sciences
Madingley Rise, Madingley Road
Cambridge CB3 OEZ, ENGLAND

Dr. Jorg Schlittenhaardt
Federal Institute for Geosciences & Nat'l Res.
Postfach 510153
D-3000 Hannover 51, GERMANY

Dr. Johannes Schweitzer
Institute of Geophysics
Ruhr University/Bochum
P.O. Box 1102148
4360 Bochum 1, GERMANY